
Electronic Thesis and Dissertation Repository

9-12-2013 12:00 AM

Automated Segmentation of Left and Right Ventricles in MRI and Classification of the Myocardium Abnormalities

Cyrus (Mohammad Saleh) Nambakhsh
The University of Western Ontario

Supervisor

Dr. Terry Peters

The University of Western Ontario

Graduate Program in Biomedical Engineering

A thesis submitted in partial fulfillment of the requirements for the degree in Doctor of Philosophy

© Cyrus (Mohammad Saleh) Nambakhsh 2013

Follow this and additional works at: <https://ir.lib.uwo.ca/etd>

 Part of the [Bioimaging and Biomedical Optics Commons](#), and the [Other Biomedical Engineering and Bioengineering Commons](#)

Recommended Citation

Nambakhsh, Cyrus (Mohammad Saleh), "Automated Segmentation of Left and Right Ventricles in MRI and Classification of the Myocardium Abnormalities" (2013). *Electronic Thesis and Dissertation Repository*. 1655.

<https://ir.lib.uwo.ca/etd/1655>

This Dissertation/Thesis is brought to you for free and open access by Scholarship@Western. It has been accepted for inclusion in Electronic Thesis and Dissertation Repository by an authorized administrator of Scholarship@Western. For more information, please contact wlsadmin@uwo.ca.

AUTOMATED SEGMENTATION OF LEFT AND RIGHT VENTRICLES
IN MRI AND CLASSIFICATION OF THE MYOCARDIUM
ABNORMALITIES

(Thesis format: Integrated Article)

by

Cyrus (M. S.) Nambakhsh

Graduate Program in Biomedical Engineering

A thesis submitted in partial fulfillment

of the requirements for the degree of

Doctorate of Philosophy

The School of Graduate and Postdoctoral Studies

Western University

London, Ontario, Canada

© Cyrus (M. S.) Nambakhsh 2013

Abstract

A fundamental step in diagnosis of cardiovascular diseases, automated left and right ventricle (LV and RV) segmentation in cardiac magnetic resonance images (MRI) is still acknowledged to be a difficult problem. Although algorithms for LV segmentation do exist, they require either extensive training or intensive user inputs. RV segmentation in MRI has yet to be solved and is still acknowledged a completely unsolved problem because its shape is not symmetric and circular, its deformations are complex and varies extensively over the cardiac phases, and it includes papillary muscles. In this thesis, I investigate fast detection of the LV endo- and epi-cardium surfaces (3D) and contours (2D) in cardiac MRI via convex relaxation and distribution matching. A rapid 3D segmentation of the RV in cardiac MRI via distribution matching constraints on segment shape and appearance is also investigated. These algorithms only require a single subject for training and a very simple user input, which amounts to one click. The solution is sought following the optimization of functionals containing probability product kernel (or Bhattacharya) constraints on the distributions of intensity and geometric features. The formulations lead to challenging optimization problems, which are not directly amenable to convex-optimization techniques. For each functional, the problem is split into a sequence of sub-problems, each of which can be solved exactly and globally via a convex relaxation and the augmented Lagrangian method. Finally, an information-theoretic based artificial neural network (ANN) is proposed for normal/abnormal LV myocardium motion classification. Using the LV segmentation results, the LV cavity points is estimated via a Kalman filter and a recursive dynamic Bayesian filter. However, due to the similarities between the statistical information of normal and abnormal points, differentiating between distributions of abnormal

and normal points is a challenging problem. The problem was investigated with a global measure based on the Shannon's differential entropy (SDE) and further examined with two other information-theoretic criteria, one based on Renyi entropy and the other on Fisher information. Unlike the existing information-theoretic studies, the approach addresses explicitly the overlap between the distributions of normal and abnormal cases, thereby yielding a competitive performance. I further propose an algorithm based on a supervised 3-layer ANN to differentiate between the distributions farther. The ANN is trained and tested by five different information measures of radial distance and velocity for points on endocardial boundary.

Keywords: Left ventricle, right ventricle, wall motion analysis, machine learning, classification, artificial neural network (ANN), segmentation, support vector machines, kernel density estimation, probability product kernel, MRI, bhattacharyya coefficient, convex relaxation.

Acknowledgements

“No man is an island entire of itself; every man is a piece of the continent, a part of the main”, John Donne. No thesis is solely the work of one person.

Foremost, I would like to express my sincere gratitude to Dr. Terry M. Peters and Dr. Ismail Ben Ayed for their peerless support, patience, persuasions, and immense knowledge. It was only for their deep vision and guidance that I was empowered to survive all the ups and downs of this four years of research. Their guidance, insight and all the helps which came from their labs enriched this dissertation as it is today.

I would also like to acknowledge Dr. Maria Drangova for her feedback which always reminded me to question the assumptions and to oversee the study through a difficult lens.

I would also like to acknowledge the members of my examination board, Dr. Aaron Ward, Dr. Roy Eagleson, Dr. Olga Veksler and Dr. Anne Martel of the University of Toronto for taking time out of their schedules to read this thesis and share their invaluable insights with me.

There were many people who were not at the forefront of this thesis but they were its backbone. Truly, without their help this work would not have come to fruition. My warmest appreciation goes to Dr. Jing Yuan, Dr. Kumaradevan Punithakumar, Dr. Aashish Goela, Dr. Ali Islam and Brandon Miles.

Last but not least, my family. First, my Mom and Dad for always believing in me and teaching me to be strong, curious and independent. I must thank my siblings for their everlasting emotional support as well as occasional inspirational thoughts.

Contents

Abstract	ii
Acknowledgements	iv
List of Figures	xi
List of Tables	xvi
1 Introduction	1
1.1 The cardiovascular system	2
1.1.1 Heart, blood vessels, and pulmonary circulation	2
1.2 Heart Failure	3
1.3 Cardiovascular Magnetic Resonance Imaging	5
1.3.1 Optimization of cardiac MRI sequences: general principles	5
1.4 Clinical significance of using CMRI	6
1.4.1 Morphological CMRI	7
1.4.2 Functional CMRI	8
Cine sequences	8
Real-time cardiac imaging	8

Delayed enhancement MRI (DE-MRI)	9
1.5 Diagnosis of cardiovascular disease	10
1.5.1 Global assessment of the LV and RV	10
1.5.2 Classification of regional/global LV myocardial dysfunction	11
1.6 Automated 2D/3D segmentation of LV	12
1.6.1 Overview of LV segmentation algorithms	12
LV segmentation based on strong priors	12
LV segmentation with intensive user inputs	14
1.6.2 Optimization of distribution measures	14
1.7 Automated segmentation of the RV in 3D	16
1.7.1 Overview of RV segmentation	17
1.8 Wall motion abnormality classification	20
Prior methods	21
1.9 Thesis Objectives	23
1.10 Thesis Outline	24
1.10.1 Chapter 2: LV Segmentation in MRI via Convex Relaxed Distribution	
Matching	24
1.11 Chapter 3: RV Segmentation using Invariant Object-Interaction Priors	25
1.12 Chapter 4: An ANN Learned Information Measures for LV Myocardium Ab-	
normality Detection	27
1.12.1 Chapter 5: Conclusion, Contribution and Future Directions	28
1.12.2 Publications ensuing from the thesis	28
Published or accepted	29

Submitted	30
In preparation	30
Bibliography	30
2 Left Ventricle Segmentation in MRI via Convex Relaxed Distribution Matching	44
2.1 Contributions of this study	44
2.2 Formulation	46
2.2.1 The functional	47
Introducing a scale variable	51
2.2.2 Two-step optimization procedure	53
Convex-relaxation optimization with respect to the regions	54
Global Minimization of Energy Upper Bound	56
2.2.3 Energy Upper Bounds	58
Convex-relaxation optimization of energy upper bound	60
2.2.4 Exactness of the Convex Relaxed Min-Cut Model in (2.39)	63
Optimization with respect to the scale variable	63
2.3 Experiments	65
2.3.1 Visual samples of the 2D/3D results	66
2.3.2 Computational evaluations	66
Quantitative and comparative performance evaluations	68
Robustness of the algorithm with respect to initial surfaces/contours	72
Robustness of the 3D convex-relaxation algorithm with respect to the choice of the training subject	73

Invariance of the shape-prior models:	75
Robustness of the algorithm with respect to the choice of the weighting parameters	75
2.4 Conclusion	77
Bibliography	79
3 Right Ventricle Segmentation using Invariant Object-Interaction Priors	82
3.1 Formulation	83
3.1.1 The functional	83
Automation with a scale variable:	87
3.1.2 Two-step optimization	89
Step 1–Optimization with respect to the segment via convex-relaxed . . .	89
Step 2–Fixed-point optimization with respect to the scale variable . . .	95
3.2 Experiments	97
3.2.1 User Initialization and Segmentation Parameters	98
3.2.2 Visual Inspection	99
3.2.3 Quantitative Performance Evaluations	100
3.2.4 Invariance of the geometric distributions	105
3.2.5 Robustness with respect to the choice of training subject:	107
3.3 Discussion	107
Bibliography	108
4 ANN Learned Information Measures for LV Myocardium Abnormality Detection	112
4.1 Preprocessing of data	114

4.1.1	Information theory and cardiac motion abnormality detection	114
4.1.2	Tracking the endocardium boundary motion	116
	The recursive Bayesian Filtering and Kalman filter	117
	State Prediction	119
	Time Update	120
	Filter Initialization	120
4.1.3	The SDE, Fisher information and Rényi entropy of normalized radial distance	122
4.1.4	Artificial feed-forward back-propagation neural network	123
	Training:	124
	Testing:	125
4.2	Experiments	126
4.3	Conclusions	128
	Bibliography	129
5	Conclusion	132
5.1	General Discussion	132
5.2	Cardiovascular Magnetic Resonance Imaging	133
5.3	Techniques to automate the quantification of cardiac MRI and wall motion ab- normality detection	134
	5.3.1 Segmentations	134
	5.3.2 Wall motion	137
5.4	Future Directions	138

Bibliography 140

List of Figures

1.1	Anatomy of the heart. Red and blue organs are oxygenated and de-oxygenated blood pathways.	3
1.2	Most common causes of HF including a) myocardial infarction, b) cardiomyopathy, and c) hypertension.	4
1.3	Three main planes used in CMRI Duerden et al. [2006]	6
2.1	Red curves: the intensity distributions learned from the user click (i.e., using the image data within a small cylinder centered at the user click). Blue curves: the actual cavity distributions estimated from the ground truth. The distributions for three subjects and all the phases of a cardiac cycle are plotted.	49
2.2	A typical example, which illustrates the evolution of the segmentation and the corresponding distributions during an iterative distribution matching process.	52
2.3	The distance distribution of the training subject (blue) and the testing subject (red).	53
2.4	Iterative bound optimization: u^i denotes the labeling at iteration i	58

2.5	Results for two subjects from diastolic to systolic phases (left to right) for basal, mid-cavity and apical slices (top to bottom). The yellow contour delineates the cavity region, and the region between red and yellow contours delineates the myocardium.	67
2.6	Manual segmentation (red; 1st column): (1st line) endocardium and (2nd line) Epicardium surfaces; Result of the proposed algorithm (green; 2nd column): (1st line) Endo- and (2nd line) Epicardium surfaces; (3rd column): Corresponding 2D automatic (yellow) and manual (red) contours superimposed on 2D frames.	68
2.7	Linear regression plots depicting the automatic-segmentation volumes against manually obtained volumes in 2D (first row) and 3D (2nd row) for the entire dataset.	73
2.8	Effect of the choice of the initial surfaces/contours on the results. First line (a, b and c): The yellow curves depict three different initializations. Second line (d, e and f): The yellow curves depict the final segmentations. The red curves depict the ground-truth segmentation. The obtained results were approximately the same, although the initial contours were significantly different.	74
2.9	Distance distributions of 50 volumes obtained from 10 subjects (5 each) for (a) cavity and (b) myocardium regions; The average Bhattacharyya measures for all pairs of analyzed volumes (50 volumes) is 0.93 for cavity and 0.88 for myocardium. The distributions were estimated using 192 bins and a kernel width of 2.	76

2.10	The average <i>DM</i> and <i>RMSE</i> over all the data-set as functions of the weights of the shape priors: (a-b) α_c ; (c-d) α_m	77
2.11	The average <i>DM</i> and <i>RMSE</i> over all the data-set as functions of the smoothness/edge weights: (a-b) λ ; and (c-d) β	78
3.1	(a) An example of regions connected to the RV in which their intensity profiles are very similar to that of the RV region (the region enclosed within the red curve); (b) The geometric relationships between the LV centroid and the RV region for building the object-interaction priors.	87
3.2	Plots of the angle, distance from LV centroid and intensity distributions of the pixels within the RV cavities for 20 frames of one single sequence of a single subject (the manual segmentations are used to compute these distributions). 1st row: angles; 2nd row: distances from LV centroid; 3rd row: intensities. 1st column: apical slices; 2nd column: mid-cavity slices; 3rd column: basal slices.	88
3.3	Invariance and shift of the distance-based shape model.	88
3.4	A typical example using a $125 \times 125 \times 6$ volume. (a-b): Manual and automatic surfaces; (c-d): The corresponding 2D contours/slices.	99
3.5	An example using a $256 \times 126 \times 9$ volume from MICCAI'12 dataset. The surfaces rendered with a simple nearest neighbour interpolation between each 2 consecutive slices.	100

3.6	Comparison of Median DM for ED and ES phases (Test1 and Test2 datasets together) for all algorithms participated in MICCAI'12 challenge. The median is the middle red bar. The box indicates the lower quartile (splits 25% of lowest data) and the upper quartile (splits 75% of highest data). The whiskers are the maximum and minimum values.	104
3.7	(a) Plots the manual volumes versus the automatic volumes for cardiac subjects; (b) Dice metric's reliability: $R(d) = Pr(DM > d)$ for MRIUWO dataset.	105
3.8	Invariance of the angle and distance distributions. 16 subjects, 6 frames from apical to basal per each subject. The distributions have been superimposed for (a) distance and (b) angle priors. The distributions were estimated using 192 bins and a kernel width $\sigma = 2$	106
3.9	The angle and distance distributions for the RV cavity for 20 frames from different sequences (Apical, Basal, Mid-cavity) belonging to a single subject. To measure the distributions, the manually segmented contours were used. 1st row: cosine of angles; 2nd row: distances from LV centroid. 1st column: apical slices; 2nd column: mid-cavity slices; 3rd column: basal slices.	106
3.10	(a) and (b): Robustness of the proposed algorithm with respect to the choice of the training subject, (c): Invariance of the distance-based shape model.	107
4.1	Distributions of radial velocity of all normal (blue) and abnormal (red) points in my dataset.	113

4.2	The power of the SDE compared to the Mean in classifying ab/normal motions. (a) typical normal, (b) typical abnormal heart motion trajectory, (c) and (d) corresponding distributions of radial distance and velocity. SDE unlike the Mean is able to create a more discriminative margin between normal and abnormal motion distributions despite a significant overlap between them; the figures are from Punithakumar et al. [2010].	115
4.3	An illustration of segmented cavity region and sampled contour. Each point such as P_1 on the boundary of far left contour should be tracked over cardiac temporal phases from systolic (middle contour) to diastolic (far right and left). The pink point is the centroid of the cavity and r is the distance of an assumed point (P_i) to the centroid (radial radial).	116
4.4	The block diagram of Kalman Filter. P_t is state prediction covariance and S_t the state.	119
4.5	a) A node in ANN model, and b) General structure of the ANN.	124
4.6	Receiver operating characteristics of the ANN, Information-theoretic and SVM classifiers are illustrated.	127
4.7	Distribution of normal and abnormal hearts using different classifiers.	128

List of Tables

2.1	Statistical measures of the conformity between manually and automatically obtained contours for my method in 2D and 3D, Graph-cut (GC) method in Ayed et al. [2012] , and level-set (LS) method in Ayed et al. [2009a] . The dataset which was used for for GC and LS algorithms is the same as the dataset which was used for our algorithm.	70
2.2	Correlation coefficients between automatically and manually obtained segmentations.	72
2.3	The mean and standard deviation of obtained average <i>DM</i> , <i>RMS E</i> and <i>CC</i> for 20 different iterations using CR 3D method, where training subject is variable at each iteration; I used 20 different training subjects and validated the algorithm on the rest of the dataset.	74
3.1	The details of MR sequence and images in MICCAI'12 dataset	98
3.2	List of MR datasets.	102

3.3	The evaluation results for automatic (A) and semi-automatic (SA) segmentation of the endocardium surfaces; mean and standard deviation of DM and HD. The methods are including CMIC Zuluaga et al. [2012], NTUST Wang et al. [2012], SBIA ou et al. [2012], ICL Bai et al. [2012], LITIS Grosgeorge et al. [2012],BIT-UPM Maier et al. [2012].	102
3.4	The evaluation results for automatic (A) and semi-automatic (SA) segmentation of endocardium surfaces on the ED and ES phases; mean and standard deviation of DM and HD. The methods are including CMIC Zuluaga et al. [2012], NTUST Wang et al. [2012], SBIA ou et al. [2012], ICL Bai et al. [2012], LITIS Grosgeorge et al. [2012],BIT-UPM Maier et al. [2012].	103
3.5	The run-time computation and off-line load for the algorithms.	103
3.6	Clinical performance for endocardium segmentation: correlation coefficient CC, linear regression coefficients on ED areas (slope a and intercept b).	103
3.7	Quantitative performance evaluations over the MRIUWO dataset. Evaluations are averaged over the entire dataset. The optimization parameters were fixed for all the subjects.	104
4.1	The AUC, \mathcal{B} and accuracy of the classifiers corresponding to Fig. 4.6 and Fig. 4.7.	128

List of abbreviations

2D 2-Dimensional

3D 3-Dimensional

AAM Active Appearance Models

AHA American Heart Association

ANN Artificial Neural Network

ASM Active Shape Models

ARVC Arrhythmogenic Right Ventricular Cardiomyopathy

AUC Area Under Curve

CVD Cardiovascular Disease

CHD Congenital Heart Disease

CMRI Cardiac MRI

CR Convex Relaxation

CT Computed Tomography

CC Correlation Coefficient

DE-MRI Delayed Enhancement MRI

DM Dice Metric

ED End-Diastolic

ES End-Systolic

EF Ejection Fraction

ECG Electrocardiogram

FPE Fixed-Point Equation

GC Graph Cut

GPU Graphics Processing Unit

HF Heart Failure

HVD Heart Valve Disease

HD Hausdorff Distance

HCM Hypertrophic Cardiomyopathy

IHD Ischemic Heart Disease

KDE Kernel Density Estimation

LS Level Set

LV Left Ventricle

MRF Markov Random Field

MRI Magnetic Resonance Images

MEDIA Medical Image Analysis

PCA Principal Component Analysis

RF Radio Frequency

ROC Receiver Operating Characteristic

RMSE Root Mean Squared Error

RV Right Ventricle

RVEF RV Ejection Fraction

SDE Shannon's Differential Entropy

SSFP Steady-State Free-Precession

SNR Signal-to-Noise Ratio

SVM Support Vector Machine

tMRI Tagged MRI

TMI Transaction of Medical Imaging

Chapter 1

Introduction

Cardiovascular disease (CVD) is the leading cause of morbidity and mortality across the world [Roger and et.al \[2012\]](#). As a particular case of CVD, heart failure (HF) or congestive heart failure occurs when the heart is not able to pump out a sufficient volume of blood to meet the needs of the body [Kuznetsova et al. \[2010\]](#). Radiologically diagnosing HF in its early stages plays an essential role in treatment and improvement of clinical outcomes.

With a 40 percent fatality rate, CVD imposes a huge burden on society and the healthcare system. In order to reduce the rate of hospitalization and cost, including that of radiologists time per case, and shortening the diagnostic procedure, tools that allow radiologists to reach an early, efficient, simple and accurate quantification of clinical criteria are highly desired.

1.1 The cardiovascular system

The cardiovascular system¹ includes the heart, blood, pulmonary circulation and vessels to carry blood throughout the body. The essential components of the human cardiovascular system are briefly explained in the following.

1.1.1 Heart, blood vessels, and pulmonary circulation

The heart² is a cone-shaped organ with four hollow chambers and is about the size of a closed fist (10-12cm in length and 8-10cm in breadth). It is geometrically located between the left and right lungs, behind the sternum, in the thoracic cavity with its apex tilted towards the left side of the chest cavity. The heart muscle is called the myocardium, with the inner boundary being named the endocardium and the outer surface the epicardium. The heart is split into four chambers, atria (upper chambers) and ventricles (lower chambers). It performs as two anatomically connected pumps, which are shown in Fig. 1.1³:

1. The right heart: This part receives the de-oxygenated blood from the body and pumps it into the lungs;
2. The left heart: This part receives oxygenated blood from the lungs and pumps it out to the entire body;

¹http://www.heartfailure.org/eng_site/introheart.asp

²http://www.heartfailure.org/eng_site/introheart_heart.asp

³http://en.wikipedia.org/wiki/File:Heart_diagram-en.svg

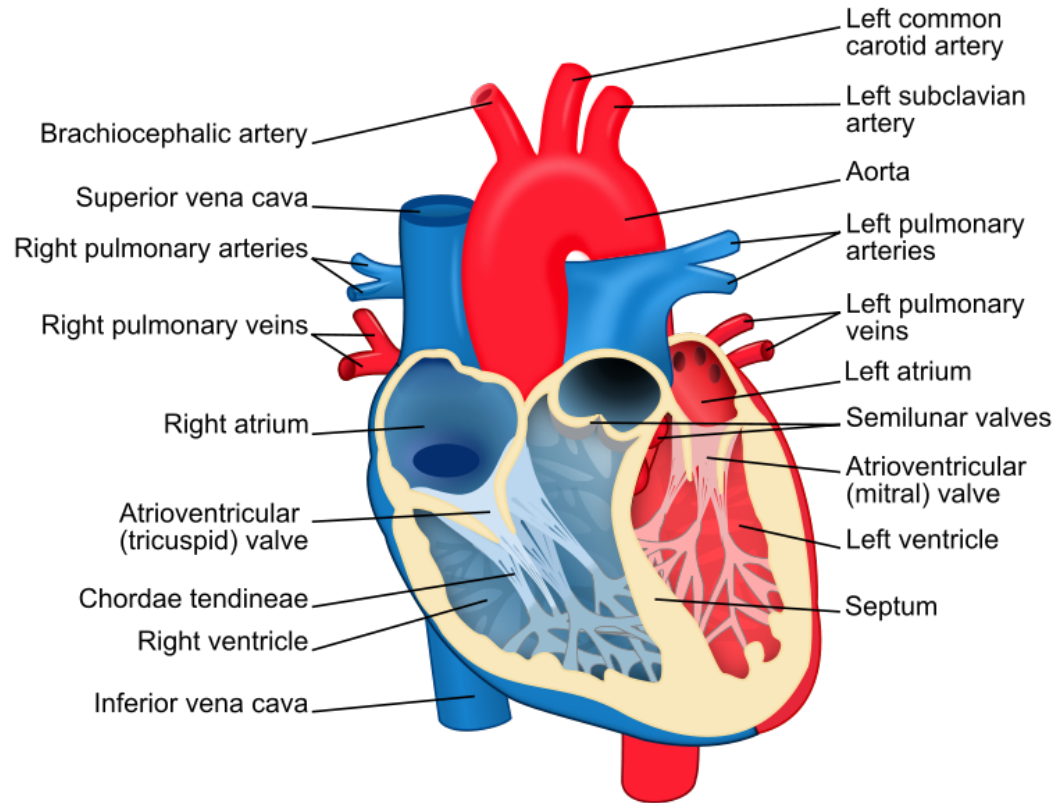


Figure 1.1: Anatomy of the heart. Red and blue organs are oxygenated and de-oxygenated blood pathways.

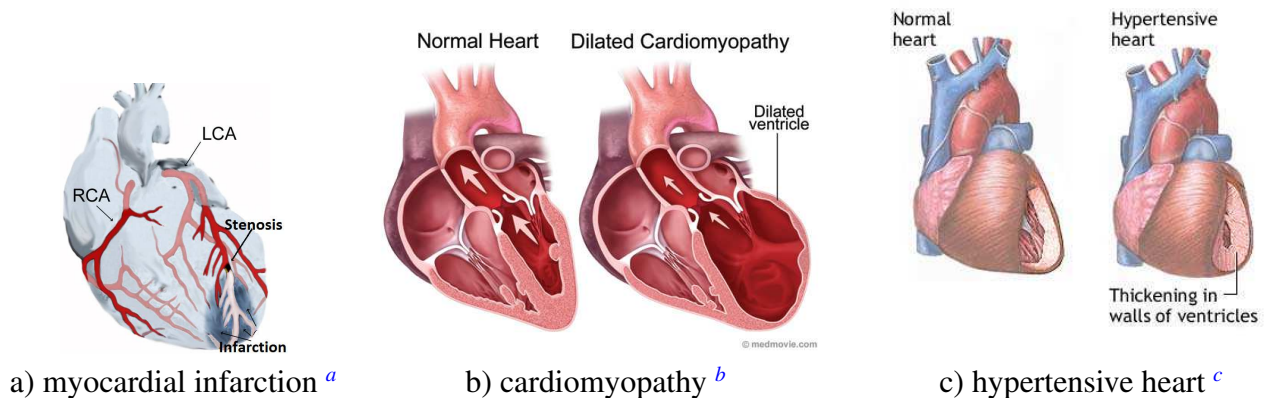
1.2 Heart Failure

HF is a chronic condition indicated by failure of the heart to fill the ventricles or failure of the heart muscles to eject adequate blood to the rest of the body⁴. Its progression can stem from a number of different pathologies such as myocardial infarction, cardiomyopathy and hypertension [Figueroa and Peters \[2006\]](#), which are illustrated in Fig.1.2. Congestive HF affects roughly half a million Canadians annually and its incidence is rising [Ross et al. \[2006\]](#). HF occurs under one of the following conditions [Afshin \[2012\]](#):

⁴http://en.wikipedia.org/wiki/Heart_failure

- **Diastolic heart failure or preserved ejection fraction (EF):** The LV is not sufficiently filled with blood in each cycle;
- **Systolic heart failure or reduced EF:** The left myocardium does not pump sufficient blood during each heart beat;
- **Coronary artery disease:** An insufficient quantity of blood is pumped into the heart because of a blockage or narrowing of coronary arteries;
- **Cardiomyopathy:** An infection weakens the heart muscle;

Additionally, other common causes of HF Afshin [2012] can be congenital heart disease(CHD), heart valve disease (HVD), high blood pressure, diabetes, lung diseases, sleep apnea and some abnormal rhythms ⁵.



^awww.en.wikipedia.org

^bwww.genedx.com

^cwww.optimumhealthvitamins.com

Figure 1.2: Most common causes of HF including a) myocardial infarction, b) cardiomyopathy, and c) hypertension.

⁵<http://www.nlm.nih.gov/medlineplus/ency/article/000158.htm>

1.3 Cardiovascular Magnetic Resonance Imaging

The structural and functional examination of the heart using imaging modalities is challenging since the heart moves with the cardiac cycle, respiratory motion and blood flow [ima, Afshin \[2012\]](#). Motion is usually the main sources of artifacts in MR images and, to date, a range of strategies have been developed to deal with these effects. Current advances in MRI techniques have made cardiac diagnosis possible using MRI in routine clinical practices. In fact, MRI is the main choice for cardiac motion tracking and analysis, and it provides a medium for 3D assessments of regional and global cardiac function [Wang and Amini \[2012\]](#).

To overcome the motion artifacts, various strategies exist:

- Fast acquisition sequences;
- Synchronization with the motion (gating);
- Containing or averaging the motion;

The last two methods can be used to account for respiratory motion. However, breath-holds are employed only if the length of breath-hold is compatible with the patient's clinical state. Otherwise, echo-navigator gating is used to synchronize with respiratory motion and mitigate its effects, albeit with an increase in acquisition time.

1.3.1 Optimization of cardiac MRI sequences: general principles

Ultra-fast spin echo and fast gradient echo sequences are two main choices for cardiac MRI (CMRI) examination [Nitz \[2002\]](#), [ima](#). Several advanced strategies have been developed to

accelerate CMRI acquisitions [Bernstein et al. \[Sep 21, 2004\]](#), [ima](#). These include:

- Optimizing radio frequency (RF) pulse;
- gradient sequences;
- Single-shot sequences;
- Parallel imaging with phased array coils;
- Optimized k-space filling: k-space data sharing, partial k-space, segmented k-space;

1.4 Clinical significance of using CMRI

CMRI exams are non-invasive, unlike computed tomography (CT) and X-ray, and do not expose patients to ionizing radiation [Wang and Amini \[2012\]](#). CMRI acquisitions are mainly based on four chambers (long-axis), LV long-axis, or LV short-axis protocols as shown in [Fig.1.3](#). The short-axis plane demonstrates only the ventricles. It is used in the volumetric

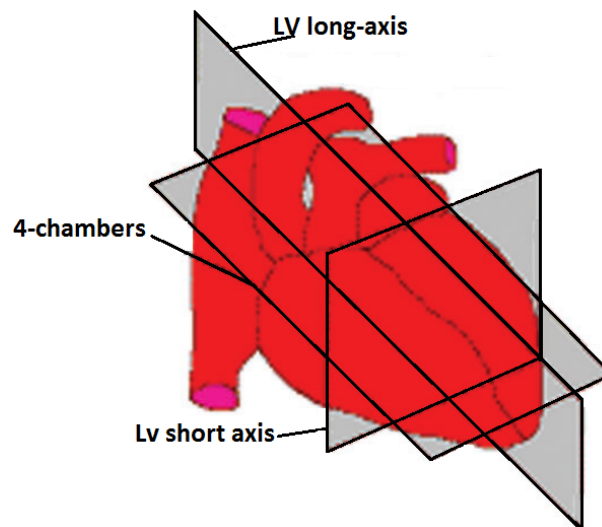


Figure 1.3: Three main planes used in CMRI [Duerden et al. \[2006\]](#).

analysis of both chambers, assessment of ventricular mass, wall motion analysis and perfusion abnormalities [Duerden et al. \[2006\]](#), [Liney \[2006\]](#). The LV long-axis, which displays two chambers, is used in assessment of the LV walls, left atrium, and mitral valve [Duerden et al. \[2006\]](#). The 4-chamber view demonstrates the atria and ventricles, tricuspid and mitral valves, and the wall between chambers [Duerden et al. \[2006\]](#). CMRI planes, with the advantage of unrestricted fields of view, provide an adequate medium to assess abnormalities of various sizes and shapes within the ventricles [ima, Selvanayagam et al. \[2003\]](#), [Walsh and Hundley \[2007\]](#). The inherent 3D and 4D nature of CMRI makes it suitable for studying the LV/RV function and structure, which are typically challenging to assess due to their complex and deformable morphology and motion [Wang and Amini \[2012\]](#). Steady-state free-precession (SSFP) sequences of CMRI provide sufficient gray-scale contrast between blood and myocardium regions. Hence, they are most commonly used for regional and global assessments of the LV structural and functional abnormalities [Liney \[2006\]](#), [Sarwar et al. \[2008\]](#). However, CMRI has the following disadvantages:

1. Not being real-time for most of sequences,
2. High cost, and
3. Lower resolution compared to X-ray and CT.

1.4.1 Morphological CMRI

The purpose of this technique is to visualize scar or fat on the myocardium without using a contrast agent [Liney \[2006\]](#). This imaging approach typically uses fast and ultra-fast spin echo sequences with prospective electrocardiogram (ECG) gating and diastolic acquisition [Robert](#)

W. Biederman [2009], ima. The morphological cardiac MRI clearly delineates the heart chambers while illustrating blood in dark contrast Lee [December 14, 2005], Robert W. Biederman [2009]. Fast spin echo sequences, along with multiplane techniques, can be performed in a breath-hold setting ima, Liney [2006]. However, breath-hold is not compulsory because ultra-fast spin echo sequences are able to acquire a slice during a single cardiac cycle (within an R-R interval) ima, Robert W. Biederman [2009].

1.4.2 Functional CMRI

Cine sequences

Ultra-fast gradient echo sequences are the MR imaging techniques of choice for the dynamic study of cardiac motion and function, with a balanced SSFP that is most commonly used for cardiac cine studies Robert W. Biederman [2009], ima, Lee [December 14, 2005]. Blood typically appears bright in these sequences and the technique can differentiate blood and myocardium very well Robert W. Biederman [2009]. Briefly, these techniques have the advantage of being very fast, have a high signal-to-noise ratio (SNR) and a high contrast. In order to improve temporal resolution, these acquisitions are preferably acquired with retrospective ECG gating over several heart beats ima, Lee [December 14, 2005].

Real-time cardiac imaging

Real-time MRI is vital to continuous monitoring of moving objects such as heart. Since MRI is a very slow process of scanning of k-space, acquiring real-time MRI was almost impossible without losing image quality or temporal resolution Uecker et al. [2010]. However, new time-

correlated parallel acquisition techniques (k-t BLAST, k-t SENSE) show promise for real-time imaging with sufficient resolution [Uecker et al. \[2010\]](#), [Lee \[December 14, 2005\]](#), [ima](#). The main importance of real-time imaging is its capacity in cardiac kinetic studies for patients with arrhythmia, or those not capable of performing an adequate breath-hold [Lee \[December 14, 2005\]](#), [ima](#). Some new real-time MRI methods achieve a temporal resolution of 20 to 30 milliseconds for images with an in-plane resolution of 1.5 to 2.0 mm [Uecker et al. \[2010\]](#).

Delayed enhancement MRI (DE-MRI)

Myocardial delayed enhancement studies are performed about 10 minutes after injection of the contrast agent. The DE-MRI acquisition employs an inversion-recovery pulse to negate normal myocardium. It is followed by a segmented k-space gradient-echo acquisition [Vogel-Claussen et al. \[2006\]](#), [Lee \[December 14, 2005\]](#). Scar tissues that are formed on myocardium or by catheter based radiofrequency ablation (RFA) therapy retain the contrast agent so that the intensity signal on T1-weighted images are increased [Vogel-Claussen et al. \[2006\]](#), [Robert W. Biederman \[2009\]](#). Primarily, the purpose of this technique is characterizing myocardial scarring caused by myocardial infarction [Vogel-Claussen et al. \[2006\]](#). On these images, scars are indicated as bright pixels [Robert W. Biederman \[2009\]](#), [Vogel-Claussen et al. \[2006\]](#). Other applications of DE-MRI include cardiomyopathy, inflammatory or infectious diseases of the myocardium, and congenital cardiac conditions such as arrhythmogenic right ventricular cardiomyopathy (ARVC). 3D imaging enables a large volume of data to be acquired within a single breath-hold, whereas 2D acquisitions offer better spatial resolution (less blurring due to motion), and provide better visualization of trans-mural enhancement extension [ima](#).

1.5 Diagnosis of cardiovascular disease

In clinical practices, the assessment of the LV and RV regions rely mainly on manual segmentations of the corresponding cavity or myocardial regions, for the quantification of clinical criteria. However, drawing the contours manually is tedious and prone to intra- and inter-observer variability. Myocardium wall motion is also currently assessed visually. This method extensively relies on the radiologist's ability to extract and comprehend spatial and temporal information about the wall thickening and endocardial motion, which requires extensive training [Caiani et al. \[2004b\]](#). Several clinical studies have demonstrated that visual assessments are not very accurate and are dependent on observers and their experience [Lu et al. \[2009\]](#), [Caiani et al. \[2004a,b\]](#). As a result, novel methods for automated evaluation of these regions have become a major area of research in the past few years [Petitjean and Dacher \[2011\]](#). The study in [Caiani et al. \[2004b\]](#) demonstrates the feasibility of quantitative analysis of endocardial motion from CMRI. It shows that automated algorithms can be used to detect wall motion abnormalities accurately whereas the detection of the wall motion abnormalities by radiologists could be less accurate and suffer from high inter-observer variability.

1.5.1 Global assessment of the LV and RV

The cardiac Ejection Fraction (EF) is a benchmark for global assessments of the LV and RV functions, and is often required for the diagnosis of ventricular or bi-ventricular disease. The EF, which represents the volumetric fraction of the blood being pumped out of heart in each heart cycle, is usually measured using ventricular volume during different cardiac phases [Sar-](#)

war et al. [2008]. In current clinical practice, the EF is often estimated using manual segmentations from several short-axis CMR images⁶ in a cardiac sequence which is a very tedious process Sarwar et al. [2008].

1.5.2 Classification of regional/global LV myocardial dysfunction

According to the American Heart Association (AHA)⁷ standard, heart failure is a prevalent disease caused by various cardiac conditions, in particular, Ischemic Heart Disease (IHD) Karamitsos et al. [2009]. The contractile properties of different myocardial regions become impaired by plaque build up along the inner walls of the arteries, which results in narrowing blood vessels and restricting blood flow to the heart. This impairment skews the regional LV wall motion and contractility patterns of the myocardium. Since IHD is the most common cause of sudden heart attack or death, early and accurate detection of LV wall motion abnormalities are required for the diagnosis and monitoring of IHD Buckberg [2004]. In current clinical routines, the myocardial regions are assessed for normal, hypokinesia, akinesia or dyskinesia symptoms using visual assessment of the LV motion and thus are highly subjective Harris et al. [2008], Sarwar et al. [2008]. Alternatively, computer-aided detection systems have shown promise in the analysis of LV myocardial function Caiani et al. [2004b], Shellock and Crues [2004], and the ability to classify cardiac function into normal or abnormal groups Punithakumar et al. [2009, 2010].

⁶Short-axis slices are the most reliable imaging plane for quantification of ventricular volumes and myocardial mass

⁷<http://www.heart.org>

1.6 Automated 2D/3D segmentation of LV

Rapid, reproducible and reliable assessments of the LV function, including the EF, regional wall motion, and myocardium scars are critical for the diagnosis of various cardiovascular abnormalities. As mentioned earlier, 2D/3D segmentations of the LV endo- and epicardium boundaries/surfaces in MRI is an essential step towards such assessments, yielding LV dynamics that can be translated into clinical diagnosis and measurements [Cerqueira et al. \[2002\]](#).

1.6.1 Overview of LV segmentation algorithms

The recent and comprehensive review in [Petitjean and Dacher \[2011\]](#) categorized LV segmentation algorithms into two main categories: (1) LV segmentation based on strong priors and (2) LV segmentation with intensive user inputs.

LV segmentation based on strong priors

Most of the existing LV segmentation algorithms are based on strong spatial priors such as statistical shape models or atlases [Petitjean and Dacher \[2011\]](#). Such strong priors remove the need for user intervention, at the price of time-consuming pre-processing steps, which consist of building large, manually-segmented sets of scans that train the algorithms. These methods are often built on Active Shape Models (ASM) [Zhang et al. \[2010\]](#), [Zambal et al. \[2006\]](#), [Andreopoulos and Tsotsos \[2008\]](#), [Mitchell et al. \[2002, 2001\]](#), [Assen et al. \[2008\]](#), shape-driven curve evolution [Mahapatra \[2013\]](#), [Paragios \[2003\]](#), [Xiang et al. \[2005\]](#), [Lynch et al. \[2006\]](#), or atlas-based techniques [Zhuang et al. \[2008\]](#), [Lorenzo-Valdés et al. \[2004\]](#). ASM and curve-evolution techniques generally follow two fundamental steps: (1) building a statistical

shape model of a set of aligned training shapes, and (2) finding a target region in the current image by fitting the solution to the learned model. This is achieved by using some rotational, translational and scaling parameters that need to be computed along with the segmentation process. In atlas based methods, the solution is sought by first mapping the image to a learned atlas using a registration process [Lorenzo-Valdés et al. \[2004\]](#), [Zhuang et al. \[2008\]](#), and then applying the ensuing transformation to the atlas, thereby obtaining a segmentation of the testing image. The result is then propagated over time throughout the cardiac cycle (phases) following the same principles. Although these methods can lead to exceptional performance, especially in cases that benefit the training set, they may not be sufficient for routine clinical use because of the following reasons [Ayed et al. \[2012\]](#), [Jolly \[2008\]](#), [Hautvast et al. \[2006\]](#), [Ayed et al. \[2009b\]](#):

- Strict consistency must be enforced between the solution and the training set. Therefore, some priors may have difficulty in capturing the substantial variations encountered in a clinical context, with the results often being dependent on the choice of a specific training set. For instance, a pathological case outside the training shapes may not be correctly detected, and intensity models have to be continually updated for new acquisition protocols and sequences.
- The manual segmentations of a large set of subjects (during the training phase) is time-consuming and does not account for variants in data acquisition protocols.
- On top of the computational burden of finding the segmentation regions/boundaries, existing shape-based algorithms require additional costly pose optimization procedures such as rotation, translation, and scaling. These procedures are often based on slow

gradient-descent techniques, and add significantly to the total computation time.

LV segmentation with intensive user inputs

To relax the need for intensive training sets, the recent works in [Ayed et al. \[2012\]](#), [Zhu et al. \[2010\]](#), [Ayed et al. \[2009b,c\]](#), [Hautvast et al. \[2006\]](#) used a manually segmented frame in each cardiac sequence to create training models for segmenting the rest of the sequence. In [Hautvast et al. \[2006\]](#), the authors proposed to propagate a curve throughout a cardiac cycle so as to enforce a constant intensity profile within the neighborhood of the endocardium. In [Ayed et al. \[2009c\]](#), a curve evolution equation is computed so as to match the intensity distributions of cardiac regions within consecutive frames. The benefit of these algorithms is that they rely only on the current-subject data for training. However, they also require intensive user inputs (manual delineation of an initial frame) and a heavy computational load [Ayed et al. \[2012, 2010\]](#). The recent study in [Ayed et al. \[2012\]](#) proposed a much faster (nearly real-time) distribution-matching solution using graph cuts, and demonstrated a substantial improvements in computational time and load over active contour techniques. Unfortunately, as acknowledged by [Ayed et al. \[2012\]](#), this graph cut solution is difficult to extend to 3D.

1.6.2 Optimization of distribution measures

The LV segmentation methods in [Ayed et al. \[2012, 2009c\]](#) are extensions of several recent studies in computer vision including [Mukherjee and Singh \[2011\]](#), [Pham et al. \[2011\]](#), [Ayed et al. \[2010\]](#), [Adam et al. \[2009\]](#), [Ayed et al. \[2009a\]](#), [Mukherjee et al. \[2009\]](#), [Ni et al. \[2009\]](#), [Hochbaum and Singh \[2009\]](#), [Mitiche and Ayed \[2010\]](#), [Vicente et al. \[2010\]](#). In the context of 2D colour segmentation, these studies have shown that distribution-matching formulations can

yield outstanding performance that are unattainable with standard segmentation algorithms. The problem consists of finding a segmentation region consistent with a prior model distribution of some image and shape features. To address this, they optimize a global measure of similarity (or discrepancy) between distributions or histograms, e.g., the Earth Mover's Distance [Adam et al. \[2009\]](#), the Kullback–Leibler divergence [Mitiche and Ayed \[2010\]](#), the Bhattacharyya coefficient [Ayed et al. \[2009a\]](#), the Wasserstein distance [Ni et al. \[2009\]](#), the norm of the difference between histograms [Mukherjee et al. \[2009\]](#), and the dot product between histograms [Hochbaum and Singh \[2009\]](#). The use of global measures in image segmentation often leads to challenging optimization problems that are solved either with active contours [Mitiche and Ayed \[2010\]](#), [Adam et al. \[2009\]](#) or iterative graph cuts [Pham et al. \[2011\]](#), [Ayed et al. \[2010\]](#), [Vicente et al. \[2010\]](#). The active contour solutions were obtained following standard gradient-descent procedures using Euler-Lagrange partial differential equations [Adam et al. \[2009\]](#), [Ayed et al. \[2009a\]](#), [Mitiche and Ayed \[2010\]](#). A gradient flow is computed so as to optimize the similarity between the region within the active contour and a given model. In the case of global distribution measures, active contours lead to computationally intensive algorithms, when the image dimension is high (3D or higher) [Ayed et al. \[2010\]](#), [Mitiche and Ayed \[2010\]](#), [Ayed et al. \[2012\]](#), which may significantly limit their application in medical imaging. Along with an incremental contour evolution, these algorithms require a large number of updates of computationally expensive integrals, which include the distributions of the regions defined by the curve at each iteration and the corresponding measures. Moreover, the robustness of the ensuing algorithms rely on a user initialization of the contour close to the target region and the choice of an approximating numerical scheme of contour evolution. The recent graph cut solutions demonstrated significant improvements over active contours in regard to

computational load and speed as well as the optimality of the solution [Pham et al. \[2011\]](#), [Ayed et al. \[2010\]](#). Unfortunately, these graph-cut solvers are not amenable to parallel computations [Yuan et al. \[2010\]](#), and are difficult to extend beyond the 2D case [Klodt et al. \[2008\]](#), [Ayed et al. \[2012\]](#). In practice, it is well known that graph cut algorithms can yield excellent performances in the case of 2D grids with 4-neighborhood systems [Boykov and Kolmogorov \[2004\]](#), using heuristics that efficiently handle sparse grids. However, the efficiency of the algorithms may decrease considerably when moving from 2D to 3D (or higher-dimensional) grids and when using larger-neighborhood grids [Klodt et al. \[2008\]](#). Furthermore, the well-known grid bias (or metrication error) is another limitation of graph-based approaches [Pock et al. \[2009\]](#). These Metric artifacts can be reduced by increasing the number of neighboring graph nodes, but this may result in a very heavy computation and memory load.

1.7 Automated segmentation of the RV in 3D

The quantification of RV function for estimating clinical criteria such as the RV ejection fraction (RVEF) is critical in diagnosis of several bi-ventricular abnormalities. In some cases, it also can help to better understand LV defects. RVEF is known as an independent predictor of survival in patients with stable and moderate congestive HF as well [de Groote et al. \[1998\]](#). RV segmentation in MRI is an essential step towards such quantification, yielding RV dynamics which can be translated to improve clinical outcomes [Grothues et al. \[2004\]](#). However as previously mentioned, manual segmentation of 4D (3D+time) cardiac volumes is tedious and time-consuming.

1.7.1 Overview of RV segmentation

As pointed out in the recent cardiac-segmentation review in [Petitjean and Dacher \[2011\]](#), RV segmentation in MRI is still acknowledged as a difficult and a completely unsolved problem, unlike LV segmentation which has been intensively researched during the last decade [Petitjean and Dacher \[2011\]](#). The main challenges arise from the highly variable and complex deformations of the 3D RV chamber, its crescent-shaped structure, and the presence of papillary muscles. In the following, I review some of the existing RV segmentation algorithms, including those presented recently in the MICCAI'12 RV segmentation challenge. Oskar et al. [Maier et al. \[2012\]](#) proposed an approach to segment the RV endo-cardium surfaces semi-automatically. The method is based on 4D region-merging graph cuts (rmGC) and only requires few markers to be placed by a user. Also, an automated method is used to enhance the manual markers required by the graph-cut algorithm. They took into account both the 3D spatial and the temporal dimensions. Since the algorithm applies graph-cut optimization over the original spatial images, the drawback of this method is the lack of consideration of complex variations in RV shape and variation over cardiac phases.

In [Grosgeorge et al. \[2012\]](#), Grosgeorge et al. proposed a segmentation method based on a statistical shape model. A set of training shapes is filtered through a principal component analysis (PCA) to yield prior maps, each of which is represented by a signed distance map [Tsai et al. \[2003\]](#). The approach registers the prior maps to the new subject. Then, to obtain segmentations, it uses graph-cut optimizers to minimize a cost functional consisting of the prior. This approach is intended to overcome the low contrast between RV and the surrounding

tissues.

The study in [Bai et al. \[2012\]](#) presents a 3D multi-atlas based registration-segmentation method, which labels the RV myocardium and the blood pool by registering a target image to the label maps from each atlas. Then, it fuses the results to yield a final labeling map. This method requires an extensive initial input by the user in the form of landmarks and is very slow as it requires an exhaustive registration between the target and all atlases. [Zuluaga et al. \[2012\]](#) proposed an automated atlas-based propagation segmentation approach that combines an intensity image with a labeling image. The algorithm consists of a three-step coarse-to-fine segmentation strategy as following:

1. Foreground and background marker generation from a manual contour denoting the inside of the RV wall outlined by a user within 4 to 5 slices of the end-diastole (ED) phase;
2. Applying a watershed transform to obtain an over-segmented region of the image;
3. Merging these regions using 4D graph-cuts with intensity- and boundary-based terms.

One of the drawbacks of the method is its dependence solely on the intensity profiles of the RV region, while there are regions surrounding the RV with a similar intensity profile.

[Wang et al. \[2012\]](#) proposed a simple and fully automated unsupervised segmentation method, which combines the spatial morphological patterns in X-Y directions with the temporal cyclic cardiac motion patterns in order to find the RV endocardium contour from 4D CMRI data.

[Maria et al. \[2004\]](#) proposed an atlas-based algorithm for 4D RV and LV CMR segmentation. The algorithm used a 4D probabilistic atlas map of four distinct

anatomical structures of heart (e.g., LV, myocardium, RV and background) from manual contours delineated on MR images of fourteen healthy volunteers. The algorithm incorporates spatially and temporally varying priors from the atlas map into an expectation maximization (EM) segmentation algorithm to estimate initial model parameters and integrate a priori into the classification algorithm. The classifier was composed of the EM, a 4D Markov Random Field (MRF), and a global connectivity filter.

In [Zhang et al. \[2010\]](#), a two-stage 4D LV and RV segmentation method based on combined ASM/AAM algorithm in short- and long-axis MRI proposed. To fuse short- and long-axis images, they used a simple translation-based registration algorithm. Initially, a 4D model was constructed for preliminary segmentations. To this end, landmarks were created on all sample shapes in training set using the template-based framework in [Frangi et al. \[2002.\]](#). This 4D model was used to achieve robust preliminary segmentation on all cardiac phases simultaneously, and then, a 3D model applied to each phase to improve local accuracy while maintaining the overall robustness of the 4D segmentation. The second segmentation step was designed to achieve better cardiac motion tracking as well as improved shape details. The algorithm is semi-automated segmentation and requires user to provide manual initialization on one cardiac phase.

Most of the existing RV/LV segmentation algorithms require intensive learning from a large, manually-segmented training set. They also require expensive shape registration and pose estimation procedures. Enforcing a *strict consistency* between the solution and the training set, these algorithms may have difficulty in capturing the substantial variations encountered in a clinical context, with the results often being dependent on the choice of a specific training

set.

1.8 Wall motion abnormality classification

Diagnosis of LV dysfunctions such as wall motion abnormalities are an essential step to effectively detect cardiac diseases such as early stage coronary artery disease. Heart conditions such as IHD are commonly caused by a decrease in blood supply produced by coronary artery stenosis [Garcia-Barnes et al. \[2010\]](#). IHD appears as an abnormality in the wall motion and contractility patterns in different regions of the myocardium, especially the LV myocardium [Garcia-Barnes et al. \[2010\]](#). As per the AHA standards [Cerqueira et al. \[2002\]](#), current clinical practices for the diagnosis of the abnormal wall motion are labor-intensive, subject to high inter-observer variability [Hoffmann et al. \[2006\]](#), and are not reproducible. The clinical study in [Paetsch et al. \[2006\]](#) tested and compared the diagnostic accuracy of four physicians who were requested to identify wall motion abnormalities in the diagnosis of 150 consecutive MR examinations. The diagnostic sensitivity, specificity, and accuracy of all physicians were 78.2, 87.0 and 82.5% respectively, while the mean kappa coefficient (k) of their agreement was 59%. Hoffmann et al. in [3] also compared three different modalities including echocardiography with and without contrast agent, MRI, and cineventriculography. The k for these modalities were 41%, 77%, 43%, and 56% [Hoffmann et al. \[2006\]](#). None of these modalities resulted in a near perfect agreement among readers. The variability in their diagnostic results stems from the visual differences between the motion of abnormal and normal segments. Alternatively, computer-aided diagnostic systems have been utilized to analyze these large data-sets of 2D images [Qian et al. \[2008\]](#), [Qazi et al. \[2007\]](#), [Suinesiaputra et al. \[2009\]](#), [Punithakumar et al.](#)

[2009], [Leung and Bosch \[2007\]](#).

Prior methods

A few studies in the literature have tried to automate the wall motion analysis. Zhen et al. [Qian et al. \[2008\]](#) proposed a tensor-based classification method which uses the spatio-temporal structure of the myocardial deformation in tagged MRI (tMRI). The algorithm extracts the motion information from the tMRI using a non-tracking-based strain estimation approach [Qian et al. \[2007\]](#). The assumption is that the myocardium is incompressible, and it undergoes three types of deformation over cardiac phases including local rotation, stretching, and compression. The algorithm analyzes the gradient of the tag deformation by applying a 2D Gabor filter and optimizing its parameters such as orientation and spacing of a 2D Gabor's sinusoidal modulation in the spatial domain [Qian et al. \[2008\]](#). Maleeha et al. [Qazi et al. \[2007\]](#) combined a set of local and global features including ejection fraction (EF) ratio, circumferential strain, thickness, thickening, velocity, radial displacement, timing, eigen-motion, curvature, and bending energy of the LV in echocardiograms, where all the features were based on the systolic phase [Qazi et al. \[2007\]](#). Then they use a 1-norm linear Fisher's discriminant classifier to provide the classification for each myocardium segment and the entire heart. Other methods include an approach that locates shape variations for echocardiograms [Leung and Bosch \[2007\]](#), a shape-based classification using principal component analysis and active appearance model in echocardiograms [Bosch et al. \[2005\]](#), a hidden Markov model for wall motion detection using stress echocardiography [Mansor and Noble \[2008\]](#). MRI-based wall motion abnormality detection has attracted a great deal of research attention recently [Qian et al. \[2008\]](#), [Lu et al. \[2009\]](#), [Suinesiaputra et al. \[2009\]](#), [Garcia-Barnes et al. \[2010\]](#), [Lekadir et al. \[2011\]](#), [Suinesiaputra](#)

et al. [2011]. Suinesiaputra et al. [Suinesiaputra et al. \[2009\]](#) built normokinetic myocardial shape models using short-axis cine MR images acquired from healthy subjects. They then applied an independent component analysis (ICA) classifier to detect and localize abnormally contracting segments of images acquired from 12 patients suffering from previous myocardial infarction [Suinesiaputra et al. \[2009, 2011\]](#).

Yingli Lu et al. proposed a pattern recognition technique [Lu et al. \[2009\]](#) built on intra-segment correlation, using a normalization scheme that maps each LV slice to polar coordinates. Assuming epicardial contours are available, the LV myocardium in each slice is normalized to polar coordinates. Knowing that the LV wall motion is approximately radial and it has a circular epicardial boundary, the analysis is simplified by mapping the pixel intensities from Cartesian (x, y) to polar coordinates with a fixed size, intensity level and position. By normalizing the length of radial distance for each point on the epicardium from the LV centroid, the method normalizes the size and shape of the myocardium.

In general, a myocardial abnormality detection algorithm must consist of two fundamental components including 1) pre-processing component and 2) classification component.

In summary, myocardial segmentation is the primary step for wall motion detection and tracking. I have explored the literature and prior art for the LV segmentation in the previous sections. In this study, prior to the classification, segmentation contours are sampled to points and a recursive Bayesian filtering [Punithakumar et al. \[2010\]](#) is applied to smooth the trajectories over temporal cardiac phases. Statistical information such as the radial distance and velocity of each point is used to quantify the trajectories [Punithakumar et al. \[2010\]](#). Finally, the LV wall motions are classified by building information theoretic measures of the statistics

(e.g., SDE) and train a classifier by combining these features.

1.9 Thesis Objectives

The objective of this thesis is to provide radiologists and other physicians with highly automated algorithms to aid them for more efficient diagnosis of cardiac MRI subjects, thereby reducing the burden of thorough visual and manual examinations. Usually examinations consist of a large set of 2D cardiac MRI slices, which is very tedious. In this PhD work, I developed mathematical algorithms, which are inspired from the visual features that radiologists look at while examining the images. Moreover, the procedures that they perform in clinical routines were followed to quantify clinical criteria for global assessment of ventricular or bi-ventricular diseases.

I believe with further developments, the algorithms can be integrated into either existing diagnostic packages or as stand-alone applications into portable machines for an efficient and repeatable diagnosis of ventricular or bi-ventricular diseases. The objectives of this research are summarized as follows:

- Developing an algorithm to provide highly rapid, repeatable, automated and accurate segmentation of LV boundaries for quantifying the LVEF and wall motion analysis;
- Developing an algorithm to provide highly rapid, repeatable, automated and accurate segmentation of the RV for quantifying the RVEF;
- Developing a robust classifier for detecting LV wall motion abnormalities.

1.10 Thesis Outline

1.10.1 Chapter 2: LV Segmentation in MRI via Convex Relaxed Distribution Matching

In this chapter, fast detection of the LV endo- and epicardium contours (2D) and surfaces (3D) in cardiac MRI via a novel convex relaxation and distribution matching algorithm is investigated. The algorithm is implemented in semi-automated manner on a Graphics Processing Unit (GPU). The 3D implementation of the algorithm only requires a single subject for training and a very simple user input, which amounts to a single point (mouse click) per target region (cavity or myocardium). It seeks cavity and myocardium regions within each 3D phase by optimizing two functionals. The mathematical expressions of the priors, along with the optimizers and the used similarity measures are explained in this chapter.

The segmentation results are used for global functional assessment of the heart by quantification of the LVEF. In clinical routines, EF is often estimated manually by drawing contours around the LV cavity and myocardium in a large number of short axis CMRI.

A quantitative and qualitative performance evaluation is reported over 400 volumes acquired from 20 subjects, which shows that the obtained results correlate with independent manual delineations. I further demonstrate experimentally that (1) the performance of the automated algorithm is not significantly affected by the choice of the training subject; and (2) the proposed shape description is used does not change significantly from one subject to another. These results support the fact that a single subject is sufficient for training the proposed

algorithm. Furthermore, it is demonstrated that there is a trade-off between the accuracy of the algorithm and the degree of automation (less user interactions). A preliminary conference version of this work appeared in IPMI 2011 [Nambakhsh et al. \[2011\]](#) and the journal version of it was accepted for publication in the Medical Image Analysis (MEDIA) journal, which expands significantly on [Nambakhsh et al. \[2011\]](#) with:

1. A 3D formulation that includes additional fixed-point optimization steps/variables, and reduces significantly the user inputs.
2. A wider experimental investigation that includes comprehensive evaluations of the robustness of the 3D algorithm with respect to the parameters and the choice of the training subject; and
3. A broader, more informative/rigorous description of the formulations including the proofs of all propositions.

1.11 Chapter 3: RV Segmentation using Invariant Object-Interaction Priors

In this chapter, a fast 3D segmentation of the RV in short-axis cardiac MRI is investigated. The RV cavity is segmented via a convex relaxation optimizer. The functionals used by the optimizer utilize distribution matching constraints that extract geometric information from the interaction between the LV and RV regions. The segmentation results are used to quantify RVEF for clinical routines. The proposed algorithm is highly automated and rapid. It relaxes the need for large, manually-segmented training sets as is the case in most of the existing atlas-

and registration-based algorithms. A performance evaluation is reported over 64 volumes acquired from 32-subject dataset provided by the RV Challenge at MICCAI'12 and 400 volumes from another dataset (20 subjects) of cine MRI. It is further experimented the robustness of the algorithm with respect to the choice of the training subject and the shape prior.

Preliminary conference versions of this work accepted in MICCAI 2013 [Nambakhsh et al. \[2013\]](#) and MICCAI 2012 [Nambakhsh et al. \[2012\]](#) RV challenge. An extended journal version is in preparation to be submitted to IEEE Transaction of Medical Imaging (TMI). It is worth noting that the use of distribution matching constraints, as is the case of my formulation of LV/RV segmentations, has recently attracted significant interest in computer vision [Gorelick et al. \[2012\]](#), [Pham et al. \[2011\]](#), [Ayed et al. \[2010\]](#), [Foulonneau et al. \[2009\]](#), and has led to outstanding segmentation performances unattainable with standard algorithms. Such constraints include several affinity measures on the distributions of segment appearance [Gorelick et al. \[2012\]](#), [Pham et al. \[2011\]](#), [Ayed et al. \[2010\]](#), as well as geometric inter-segment relationships [Ayed et al. \[2011\]](#). As a result, distribution matching constraints can relax the need for intensive training and pose estimation [Foulonneau et al. \[2009\]](#). Unfortunately, such constraints are non-linear (high-order) functionals, which result in difficult optimization problems that are not amenable to standard solvers. Most of the existing methods are based on gradient-descent procedures (e.g., active curves [Foulonneau et al. \[2009\]](#), [Mitiche and Ayed \[2010\]](#)), which may lead to weak local minima and computationally demanding algorithms [Ayed et al. \[2010\]](#), [Mitiche and Ayed \[2010\]](#). The recent graph cut solutions in [Gorelick et al. \[2012\]](#), [Pham et al. \[2011\]](#), [Ayed et al. \[2010\]](#) brought significant improvements over active curves with respect to optimality and computational load. Unfortunately, graph cuts are not

amenable to parallel computations [Yuan et al. \[2010\]](#). In practice, it is well known that graph cuts can yield excellent performance for 2D domains with 4-neighborhood systems [Boykov and Kolmogorov \[2004\]](#). However, the efficiency may decrease considerably when moving from 2D to 3D (or higher-dimensional) domains and when using larger-neighborhood systems [Klodt et al. \[2008\]](#). Furthermore, the well-known grid bias is another limitation of graph-based optimizers [Pock et al. \[2009\]](#). Therefore, I believe the proposed convex-relaxation technique can be efficiently used in cardiac image segmentation.

1.12 Chapter 4: An ANN Learned Information Measures for LV Myocardium Abnormality Detection

This chapter investigates an information theoretic based artificial neural network (ANN) for normal/abnormal LV myocardium motion classification. Using the LV segmentation contours from chapter 2, the algorithm estimates discrete points over the LV cavity contours via Kalman filter and a recursive dynamic Bayesian filter. The Recursive Bayesian filter is a general probabilistic method for estimating an unknown probability density function recursively over time. In my solution, it uses the current state of a point on the myocardium to measure its state in the next cardiac temporal phase. The algorithm consists of a prediction and estimation part, whereby having the sequences of points over temporal phases, the radial distance and velocity of each point over time is quantified. The kernel density distribution of normal and abnormal points based on the gold standard is built. Assuming the distributions are well-separated, any point on myocardium from a new subject will fall within either the distribution of normal or abnormal points from the training set. Due to the high degree of similarity between the

distributions of normal and abnormal points, the ensuing classification problem is challenging. Therefore, I investigated the problem with a set of global measures including SDE, Renyi entropy and Fisher information of radial distances and velocities. The distributions of such information theoretic measures of the myocardium motion are examined for separability. Unfortunately, since they are quite overlapped, the process results in unsatisfactory classifications.

This chapter describes the development of an ANN to be trained and tested with the above-mentioned information theoretic measures of the LV wall motion in order to improve the classification results. The algorithm combines the ability of each individual classifier with the non-linear structure of the ANN. Using 395×20 segmented LV cavities of short-axis MRI acquired from 48 subjects, the experimental results show that the proposed method outperforms Support Vector Machine (SVM) and information theoretic classifiers. It yields a specificity of 90%, a sensitivity of 91%, and an Area Under Curve (AUC) for Receiver Operating Characteristic (ROC) of 93.2%.

1.12.1 Chapter 5: Conclusion, Contribution and Future Directions

In this chapter the contributions of the study as well as its limitations at each chapter are discussed concisely. Future directions for the project to be further developed and taken to the clinical market are proposed.

1.12.2 Publications ensuing from the thesis

This PhD research has led to the following publications:

Published or accepted

1. Cyrus M.S. Nambakhsh, J. Yuan, K. Punithakumar, A. Goelaa, M. Rajchl, T.M. Peters, I. Ben Ayed, **Left Ventricle Segmentation in MRI via Convex Relaxed Distribution Matching**, Medical Image Analysis (MEDIA), 17(8), P. 1010-1024, 2013.
2. Cyrus M.S. Nambakhsh, Terry M. Peters, A. Islam, Ismail Ben Ayed, **Right Ventricle Segmentation with Probability Product Kernel Constraints**, In: Medical Image Computing and Computer-Assisted Intervention (MICCAI), 2013.
3. M.S. Nambakhsh, J. Yuan, I. Ben Ayed, K. Punithakumar, A. Goela, A. Islam, T.M. Peters, S. Li, **A Convex Max-Flow Segmentation of LV Using Subject-Specific Distributions on Cardiac MRI**, Information Processing in Medical Imaging (IPMI), Vol. 6801, P.171-183, 2011.
4. Cyrus M.S. Nambakhsh, K. Punithakumar, I. Ben Ayed, A. Goela, A. Islam, T.M. Peters, S. Li, **A neural network learned information measures for heart motion abnormality detection**, In Proceeding of Image Processing, SPIE, Vol. 7962, 2011.
5. Cyrus M.S. Nambakhsh, M. Rajchl, T.M. Peters, I. Ben Ayed, **Rapid Automated 3D RV Endocardium Segmentation in MRI via Convex Relaxation and Distribution Matching**, In: Medical Image Computing and Computer-Assisted Intervention (MICCAI) 2012 RV Challenge.
6. M. Rajchl, J. Yuan, E. Ukwatta, Cyrus Nambakhsh, J. Stirrat, J. White, and T.M. Peters (2012). **A Fast Convex Optimization Approach to Segmenting 3D Scar Tissue from Delayed-Enhancement Cardiac MR Images**, In: Medical Image Computing and

Computer-Assisted Intervention (MICCAI), 15(1): P.659-66, 2012.

Submitted

1. M. Rajchl, J. Yuan, J.A. White, E. Ukwatta, J. Stirrat, Cyrus M.S. Nambakhsh, F.P. Li, and T.M. Peters, **Fast Hierarchical Max-Flow Segmentation of Scar Tissue from Late-Enhancement Cardiac MR Images**, submitted to IEEE Transaction of Medical Imaging (TMI), April, 2013.

In preparation

1. C. Petitjean, Cyrus M.S. Nambakhsh, T.M. Peters, I. Ben Ayed, et al., **Right Ventricle Segmentation From Cardiac MRI: A Collation Study**, To be submitted to IEEE Transaction of Medical Imaging (TMI), 2013.
2. Cyrus M.S. Nambakhsh, I. Ben Ayed, A. Islam, G. Garvin, T.M. Peters, S. Li, **Graph cuts with invariant inter-segment priors**, to be Submitted to IEEE Transaction of Medical Imaging (TMI), 2013.
3. Cyrus M.S. Nambakhsh, T.M. Peters, A. Islam, I. Ben Ayed, **RV segmentation with probability product kernels**, To be submitted to IEEE Transaction of Medical Imaging (TMI), 2013.

Bibliography

<http://www.imaios.com>.

A. Adam, R. Kimmel, and E. Rivlin. On scene segmentation and histograms-based curve evolution. *IEEE Transactions on Pattern Analysis and Machine Intelligence*, 31(9):1708–1714, 2009.

M. Afshin. *Automatic Assessment of Cardiac Left Ventricle Function Via Magnetic Resonance Images*. PhD thesis, The School of Graduate and Postdoctoral Studies, Western University, London, Ontario, Canada, 2012.

A. Andreopoulos and J. K. Tsotsos. Efficient and generalizable statistical models of shape and appearance for analysis of cardiac MRI. *Medical Image Analysis*, 12(3):335–357, Jun 2008.

H. C. Van Assen, M. G. Danilouchkine, M. S. Dirksen, J. H. C. Reiber, and B. P. F. Lelieveldt. A 3-D active shape model driven by fuzzy inference: Application to cardiac CT and MR. *IEEE Transactions on Information Technology in Biomedicine*, 12(5):595–605, 2008.

I. Ben Ayed, S. Li, and I. Ross. A statistical overlap prior for variational image segmentation. *International Journal of Computer Vision*, 85(1):115–132, 2009a.

- I. Ben Ayed, S. Li, and I. Ross. Embedding overlap priors in variational left ventricle tracking. *IEEE Transactions on Medical Imaging*, 28(12):1902–1913, 2009b.
- I. Ben Ayed, S. Li, I. Ross, and A. Islam. Myocardium tracking via matching distributions. *International Journal of Computer Assisted Radiology and Surgery*, 4(1):37–44, 2009c.
- I. Ben Ayed, H.-M. Chen, K. Punithakumar, I. Ross, and S. Li. Graph cut segmentation with a global constraint: Recovering region distribution via a bound of the bhattacharyya measure. In *IEEE International Conference on Computer Vision and Pattern Recognition*, pages 1–7, San Francisco, CA, USA, 2010.
- I. Ben Ayed, K. Punithakumar, G.J. Garvin, W. Romano, and S. Li. Graph cuts with invariant object-interaction priors: Application to intervertebral disc segmentation. *Information Processing in Medical Imaging (IPMI)*, pages 221–232, 2011.
- I. Ben Ayed, H.-M. Chen, K. Punithakumar, I. Ross, and S. Li. Max-flow segmentation of the left ventricle by recovering subject-specific distributions via a bound of the bhattacharyya measure. *Medical Image Analysis*, 16:87–100, 2012.
- W. Bai, W. Shi, H. Wang, N. S. Peters, and D. Rueckert. Multi-atlas based segmentation with local label fusion for right ventricle MR images. *Medical Image Computing and Computer-Assisted Intervention (MICCAI), Workshop on RV Segmentation Challenge in Cardiac MRI*, 2012.
- M. A. Bernstein, K. F. King, and X. J. Zhou. *Handbook of MRI Pulse Sequences*. Elsevier, Sep 21, 2004.

- J. G. Bosch, F. Nijland, S. C. Mitchell, B. P. Lelieveldt, O. Kamp, J. H. Reiber, and M. Sonka. Computer-aided diagnosis via model-based shape analysis: automated classification of wall motion abnormalities in echocardiograms. *Academic Radiology*, 12(3):358–67, 2005.
- Y. Boykov and V. Kolmogorov. An experimental comparison of min-cut/max-flow algorithms for energy minimization in vision. *IEEE Transactions on Pattern Analysis and Machine Intelligence*, 26(9):1124–1137, Sep 2004.
- G. Buckberg. Left ventricular form and function: Scientific priorities and strategic planning for development of new views of disease. *Circulation*, 110:e333–e336, 2004.
- EG Caiani, E Toledo, P. MacEneaney, KA Collins, RM Lang, and V Mor-Avi. The role of still-frame parametric imaging in magnetic resonance assessment of left ventricular wall motion by non-cardiologists. *Journal of Cardiovasc Magnetic Resonance*, 6:619–25, 2004a.
- E.G. Caiani, E. Toledo, P. MacEneaney, K.A Collins, R.M. Lang, and V. Mor-Avi. Objective assessment of left ventricular wall motion from cardiac magnetic resonance images. *Computers in Cardiology*, pages 153 –156, 2004b.
- M. D. Cerqueira, N. J. Weissman, V. Dilsizian, A. K. Jacobs, S. Kaul, W. K. Laskey, D. J. Pennell, J. A. Rumberger, T. Ryan, and M. S. Verani. Standardized myocardial segmentation and nomenclature for tomographic imaging of the heart: A statement for healthcare professionals from cardiac imaging committee of the council on clinical cardiology of the american heart association. *Circulation*, 105:539–542, 2002.
- P. de Groote, A. Millaire, C. Foucher-Hossein, O. Nugue, X. Marchandise, G. Ducloux, and J.-M. Lablanche. Right ventricular ejection fraction is an independent predictor of survival

- in patients with moderate heart failure. *Journal of the American College of Cardiology*, 32: 948–954, 1998.
- R. M. Duerden, K. S. Pointon, and S. Habib. Review of clinical cardiac MRI. *Imaging*, 18: 178–186, 2006.
- M. S. Figueroa and J. I. Peters. Congestive heart failure: Diagnosis, pathophysiology, therapy, and implications for respiratory care. *Respiratory Care*, 51:403–413, 2006.
- A. Foulonneau, P. Charbonnier, and F. Heitz. Multi-reference shape priors for active contours. *International Journal of Computer Vision*, 81(1):68–81, 2009.
- A. Frangi, D. Rueckert, J. Schnabel, and W. Niessen. Automatic construction of multiple-object three-dimensional statistical shape models: Application to cardiac modeling. *IEEE Transactions on Medical Imaging*, 21(9):1151–1166, 2002.
- J. Garcia-Barnes, D. Gil, L. Badiella, A. Hernandez-Sabate, F. Carreras, S. Pujades, and E. Marti. A normalized framework for the design of feature spaces assessing the left ventricular function. *IEEE Transactions on Medical Imaging*, 29(3):733–745, 2010.
- L. Gorelick, F. R. Schmidt, Y. Boykov, A. Delong, and A. Ward. Segmentation with non-linear regional constraints via line-search cuts. *European Conference on Computer Vision (ECCV)*, pages 583–597, 2012.
- D. Grosgeorge, C. Petitjean, and S. Ruan. Right ventricle segmentation by graph cut with shape prior. *Medical Image Computing and Computer-Assisted Intervention (MICCAI), Workshop on RV Segmentation Challenge in Cardiac MRI*, 2012.

- F. Grothues, J. C. Moon, N. G. Bellenger, G. S. Smith, H. U. Klein, and D. J. Pennell. Inter-study reproducibility of right ventricular volumes, function, and mass with cardiovascular magnetic resonance. *American Heart Journal*, 147(2):218–223, 2004.
- Scott R Harris, James Glockner, Andrew J Misselt, Imran S Syed, and Philip A Araoz. Cardiac mr imaging of nonischemic cardiomyopathies. *Magnetic resonance imaging clinics of North America*, 16(2):165–183, 2008.
- G. Hautvast, S. Lobregt, M. Breeuwer, and F. Gerritsen. Automatic contour propagation in cine cardiac magnetic resonance images. *IEEE Transactions on Medical Imaging*, 25(11):1472–1482, Nov 2006.
- D. S. Hochbaum and V. Singh. An efficient algorithm for co-segmentation. In *IEEE International Conference on Computer Vision (ICCV)*, 2009.
- R. Hoffmann, S. von Bardeleben, J. D. Kasprzak, A. C. Borges, F. ten Cate, C. Firschke, S. Lafitte, N. Al-Saadi, S. Kuntz-Hehner, G. Horstick, C. Greis, M. Engelhardt, J. L. Vanoverschelde, and H. Becher. Analysis of regional left ventricular function by cineventriculography, cardiac magnetic resonance imaging, and unenhanced and contrast-enhanced echocardiography: A multicenter comparison of methods. *Journal of the American College of Cardiology*, 47(1):121128, 2006.
- M.-P. Jolly. Automatic recovery of the left ventricular blood pool in cardiac cine MR images. In *Medical Image Computing and Computer-Assisted Intervention (MICCAI)*, volume 1, pages 110–118, New York, NY, USA, 2008.
- T. D. Karamitsos, J. M. Francis, S. Myerson, J. B. Selvanayagam, and S. Neubauer. The role

- of cardiovascular magnetic resonance imaging in heart failure. *Journal of the American College of Cardiology*, 54(15):1407-1424, 2009.
- M. Klodt, T. Schoenemann, K. Kolev, M. Schikora, and D. Cremers. An experimental comparison of discrete and continuous shape optimization methods. In *European Conference on Computer Vision (ECCV) (1)*, pages 332–345, 2008.
- T. Kuznetsova, L. Herbots, Y. Jin, K. Stolarz-Skrzypek, and J. A. Staessen. Systolic and diastolic left ventricular dysfunction: from risk factors to overt heart failure. *Expert Review of Cardiovascular Therapy*, 8(2):251-258, 2010.
- V. S. Lee. *Cardiovascular MRI: Physical Principles to Practical Protocols*. Lippincott Williams & Wilkins, December 14, 2005.
- K. Lekadir, N. Keenan, D. Pennell, and G. Yang. An inter-landmark approach to 4-D shape extraction and interpretation: Application to myocardial motion assessment in MRI. *IEEE Transactions on Medical Imaging*, 30(1):52-68, 2011.
- K. Y. E. Leung and J. G. Bosch. Localized shape variations for classifying wall motion in echocardiograms. *Medical Image Computing and Computer-Assisted Intervention (MICCAI)*, 1:525-529, 2007.
- G. Liney. *MRI in Clinical Practice*. Springer, 2006.
- M. Lorenzo-Valdés, G. I. Sanchez-Ortiz, A. G. Elkington, R. H. Mohiaddin, and D. Rueckert. Segmentation of 4D cardiac MR images using a probabilistic atlas and the EM algorithm. *Medical Image Analysis*, 8(3):255–265, 2004.

- Y. Lu, P. Radau, K. Connelly, A. Dick, and G. Wright. Pattern recognition of abnormal left ventricle wall motion in cardiac MR. *in Medical Image Computing and Computer-Assisted Intervention; MICCAI, 5762:750–758, 2009.*
- M. Lynch, O. Ghita, and P. F. Whelan. Automatic segmentation of the left ventricle cavity and myocardium in MRI data. *Computers in Biology and Medicine, 36(4):389–407, 2006.* ISSN 0010-4825.
- D. Mahapatra. Cardiac image segmentation from cine cardiac mri using graph cuts and shape priors. *Journal of Digit Imaging, 26(4):721–730, 2013.*
- O. M. O. Maier, D. Jimenez-Carretero, A. Santos, and M.J. Ledesma-Carbayo. Right-ventricle segmentation with 4D region-merging graph cuts in MR. *Medical Image Computing and Computer-Assisted Intervention (MICCAI), Workshop on RV Segmentation Challenge in Cardiac MRI, 2012.*
- S. Mansor and J. Noble. Local wall motion classification of stress echocardiography using a hidden markov model approach. *IEEE Int. Symp. Biomed. Imag.: Nano Macro*, page 12951298, 2008.
- S. C. Mitchell, B. P. F. Lelieveldt, R. J. van der Geest, J. G. Bosch, J. H. C. Reiber, and M. Sonka. Multistage hybrid active appearance model matching: Segmentation of left and right ventricles in cardiac MR images. *IEEE Transactions on Medical Imaging, 20(5):415–423, 2001.*
- S. C. Mitchell, J. G. Bosch, B. P. F. Lelieveldt, R. J. van der Geest, J. H. C. Reiber, and

- M. Sonka. 3-D active appearance models: Segmentation of cardiac MR and ultrasound images. *IEEE Transactions on Medical Imaging*, 21(9):1167–1178, 2002.
- A. Mitiche and I. Ben Ayed. *Variational and Level Set Methods in Image Segmentation*. Springer, 1st edition, 2010.
- L. Mukherjee and V. Singh. Scale invariant cosegmentation for image groups. In *IEEE Conference on Computer Vision and Pattern Recognition (CVPR)*, 2011.
- L. Mukherjee, V. Singh, and C.R. Dyer. Half-integrality based algorithms for cosegmentation of images. In *IEEE International Conference on Computer Vision and Pattern Recognition (CVPR)*, 2009.
- C. M. S. Nambakhsh, M. Rajchl, T. M. Peters, and I. Ben Ayed. Rapid automated 3D RV endocardium segmentation in MRI via convex relaxation and distribution matching. *Medical Image Computing and Computer-Assisted Intervention (MICCAI), Workshop of RVChallenge*, 2012.
- C. M. S. Nambakhsh, T. M. Peters, and I. Ben Ayed. Right ventricle segmentation with probability product kernel constraints. *Medical Image Computing and Computer-Assisted Intervention (MICCAI)*, 2013.
- M. S. Nambakhsh, J. Yuan, I. Ben Ayed, K. Punithakumar, A. Goela, A. Islam, T. M. Peters, and S. Li. A convex max-flow segmentation of LV using subject-specific distributions on cardiac MRI. In *Information Processing in Medical Imaging (IPMI)*, pages 171–183, 2011.
- K. Ni, X. Bresson, T. F. Chan, and S. Esedoglu. Local histogram based segmentation using the wasserstein distance. *International Journal of Computer Vision*, 84(1):97–111, 2009.

- W. Nitz. Fast and ultrafast non-echo-planar MR imaging techniques. *Eur Radiol*, 12(12): 2866–82, 2002.
- I. Paetsch, C. Jahnke, V. A. Ferrari, F. E. Rademakers, P. A. Pellikka, W. G. Hundley, D. Poltermans, J. J. Bax, K. Wegscheider, E. F., and E. Nagel. Determination of interobserver variability for identifying inducible left ventricular wall motion abnormalities during dobutamine stress magnetic resonance imaging. *European heart journal*, 27 (12):1459–1464, 2006.
- N. Paragios. A level set approach for shape-driven segmentation and tracking of the left ventricle. *IEEE Transactions on Medical Imaging*, 22(6):773–776, Jun 2003.
- C. Petitjean and J.-N. Dacher. A review of segmentation methods in short axis cardiac MR images. *Medical Image Analysis*, 15:169–184, 2011.
- V.-Q. Pham, K. Takahashi, and T. Naemura. Foreground-background segmentation using iterated distribution matching. In *IEEE International Conference on Computer Vision and Pattern Recognition(CVPR)*, 2011.
- T. Pock, A. Chambolle, D. Cremers, and H. Bischof. A convex relaxation approach for computing minimal partitions. In *CVPR*, 2009.
- K. Punithakumar, S. Li, I. Ben Ayed, I. Ross, A. Islam, and J. Chong. Heart motion abnormality detection via an information measure and bayesian filtering. *Medical Image Computing and Computer-Assisted Intervention (MICCAI)*, 5762:373–380, 2009.
- K. Punithakumar, I. Ben Ayed, I. Ross, A. Islam, J. Chong, and S. Li. Detection of left ventric-

- ular motion abnormality via information measures and bayesian filtering. *IEEE Transactions on Information Technology in Biomedicine*, 14(4):1106–1113, 2010.
- M. Qazi, G. Fung, S. Krishnan, J. Bi, R. Bharat Rao, and A. Katz. Automated heart abnormality detection using sparse linear classifiers. *IEEE Engineering in Medicine and Biology Magazine*, 26:56–63, 2007.
- Z. Qian, D. Metaxas, and L. Axel. Non-tracking-based 2D strain estimation in tagged MRI. *IEEE International Symposium on Biomedical Imaging*, 2007.
- Z. Qian, Q. Liu, D. N. Metaxas, and L. Axel. Identifying regional cardiac abnormalities from myocardial strains using spatio-temporal tensor analysis. *Medical Image Computing and Computer-Assisted Intervention (MICCAI)*, 5241:789–797, 2008.
- June Yamrozik Robert W. Biederman, Mark Doyle. *Cardiac MRI: Guide Book on the Go*. Lippincott Williams & Wilkins, 2009.
- V. L. Roger and et.al. Heart disease and stroke statistics2012 update: A report from the american heart association. *Circulation*, 125:2–220, 2012.
- H. Ross, J. Howlett, J. M. Arnold, P. Liu, B. J. O’Neill, J. M. Brophy, C. S. Simpson, M. M. Sholdice, M. Knudtson, D. B. Ross, J. Rottger, K. Glasgow, and Canadian Cardiovascular Society Access to Care Working Group. Treating the right patient at the right time: Access to heart failure care. *Canadian Journal of Cardiology*, 22:749–745, 2006.
- A. Sarwar, M. D. Shapiro, S. Abbara, and R. C. Cury. Cardiac magnetic resonance imaging for the evaluation of ventricular function. *Seminars in Roentgenology*, 43:183–192, 2008.

- J. Selvanayagam, S. Westaby, K. Channon, J. Francis, J. Eichhfer, S. Saito, and S. Neubauer. Images in cardiovascular medicine. surgical left ventricular restoration: an extreme case. *Circulation*, 107:e71, 2003.
- F. G. Shellock and J. V. Crues. MR procedures: biologic effects, safety, and patient care. *Radiology*, 232:635–652, 2004.
- A. Suinesiaputra, A. Frangi, T. Kaandorp, H. Lamb, J. Bax, J. Reiber, and B. Lelieveldt. Automated detection of regional wall motion abnormalities based on a statistical model applied to multislice short-axis cardiac MR images. *IEEE Transactions on Medical Imaging*, 28(4):595–607, 2009.
- A. Suinesiaputra, A. F. Frangi, T. A. Kaandorp, H. J. Lamb, J. J. Bax, J. H. Reiber, and B. P. Lelieveldt. Automated regional wall motion abnormality detection by combining rest and stress cardiac MRI: Correlation with contrast-enhanced MRI. *Journal of Magnetic Resonance Imaging*, 34(2):270–278, 2011.
- A. Tsai, A. Yezzi, W. Wells, C. Tempany, D. Tucker, A. Fan, W. Grimson, and A. Willsky. A shape-based approach to the segmentation of medical imagery using level sets. *IEEE Transactions on Medical Imaging*, 22(2):137–154, 2003.
- M. Uecker, S. Zhang, D. Voit, A. Karaus, K.-D. Merboldt, and J. Frahm. Real-time MRI at a resolution of 20 ms. *NMR Biomed*, 23:986–994, 2010.
- S. Vicente, V. Kolmogorov, and C. Rother. Cosegmentation revisited: Models and optimization. In *European Conference on Computer Vision (ECCV)*, 2010.

- J. Vogel-Claussen, C. E. Rochitte, K. C. Wu, I. R. Kamel, T. K. Foo, J. A. C. Lima, and D. A. Bluemke. Delayed enhancement MR imaging: Utility in myocardial assessment. *RadioGraphics*, 2006.
- T. F. Walsh and W. G. Hundley. Assessment of ventricular function with cardiovascular magnetic resonance. *Magnetic Resonance Imaging Clinics of North America*, 15(4):487–504, 2007.
- C.-W. Wang, C.-W. Peng, and H.-C. Chen. A simple and fully automatic right ventricle segmentation method for 4-dimensional cardiac MR images. *Medical Image Computing and Computer-Assisted Intervention (MICCAI), Workshop on RV Segmentation Challenge in Cardiac MRI*, 2012.
- H. Wang and AA. Amini. Cardiac motion and deformation recovery from MRI: a review. *IEEE Trans Med Imaging*, 31(2):487–503., 2012.
- L. Xiang, C. Brett, and Y. Alistair. Model-based graph cut method for segmentation of the left ventricle. In *Conf Proc IEEE Eng. Med. Biol. Soc.*, pages 3059–3062, 2005.
- J. Yuan, E. Bae, and X.-C. Tai. A study on continuous max-flow and min-cut approaches. In *IEEE International Conference on Computer Vision and Pattern Recognition (CVPR)*, 2010.
- S. Zambal, J. Hladuvka, and K. Bühler. Improving segmentation of the left ventricle using a two-component statistical model. In *Medical Image Computing and Computer-Assisted Intervention (MICCAI)*, volume 1, pages 151–158, Copenhagen, Denmark, 2006.
- H. Zhang, A. Wahle, R. K. Johnson, T. D. Scholz, and M. Sonka. 4-D cardiac MR image

- analysis: left and right ventricular morphology and function. *IEEE Transactions on Medical Imaging*, 29(2):350–364, 2010.
- Y. Zhu, X. Papademetris, A. J. Sinusas, and J. S. Duncan. Segmentation of the left ventricle from cardiac MR images using a subject-specific dynamical model. *IEEE Transactions on Medical Imaging*, 29(4):669–687, 2010.
- X. Zhuang, K. S. Rhode, S. R. Arridge, R. Razavi, D. L. G. Hill, D. J. Hawkes, and S. Ourselin. An atlas-based segmentation propagation framework using locally affine registration - application to automatic whole heart segmentation. In *Medical Image Computing and Computer-Assisted Intervention (MICCAI)*, volume 2, pages 425–433, New York, NY, USA, 2008.
- M. A. Zuluaga, M. J. Cardoso, and S. Ourselin. Automatic right ventricle segmentation using multi-label fusion in cardiac MRI. *Medical Image Computing and Computer-Assisted Intervention (MICCAI), Workshop on RV Segmentation Challenge in Cardiac MRI*, 2012.

Chapter 2

Left Ventricle Segmentation in MRI via Convex Relaxed Distribution Matching

2.1 Contributions of this study

This chapter¹ investigates fast detection of the LV endo- and epicardium surfaces (3D) and contours (2D) in cardiac MRI via convex relaxation and distribution matching. In 2D mode, the algorithm requires the manual segmentation of the first frame in each sequence and in 3D, it requires a single subject for training and a very simple user input, which amounts to a single

1

This chapter is based on papers below:

1. Cyrus M.S. Nambakhsh, J. Yuan, K. Punithakumar, A. Goelaa, M. Rajchl, T.M. Peters, I. Ben Ayed, **Left Ventricle Segmentation in MRI via Convex Relaxed Distribution Matching**, Medical Image Analysis (MEDIA), 17(8), P. 1010-1024, 2013.
2. M.S. Nambakhsh, J. Yuan, I. Ben Ayed, K. Punithakumar, A. Goela, A. Islam, T.M. Peters, S. Li, **A Convex Max-Flow Segmentation of LV Using Subject-Specific Distributions on Cardiac MRI**, Information Processing in Medical Imaging (IPMI), Vol. 6801, P.171-183, 2011.

point (mouse click) per target region (cavity or myocardium). It seeks cavity and myocardium regions within each 3D phase by optimizing two functionals, each containing two distribution-matching constraints: (1) a distance-based shape prior and (2) an intensity prior. Based on a global measure of similarity between distributions, the shape prior is intrinsically invariant with respect to translation and rotation. The main contributions of the study that sets it apart from previous works in the literature and our own work published in IPMI'11 are including:

1. A 3D formulation that includes additional novel fixed-point optimization steps/variables,
2. reducing the user interactions to only a point for each region,
3. A wider experimental investigation that includes comprehensive evaluations of the robustness of the 3D algorithm with respect to the parameters and the choice of the training subject; and
4. A novel convex relaxation optimizer which is amendable to GPU and thereby results in a much faster algorithm.

In a nutshell, a scale variable is introduced from which a novel (fixed point equation) FPE is derived, thereby achieving scale-invariance with only few fast computations. The proposed algorithm relaxes the need for costly pose estimation (or registration) procedures and large training sets, and can tolerate shape deformations, unlike template (or atlas) based priors. The formulation leads to a challenging problem, which is not directly amenable to convex-optimization techniques. For each functional, the problem is split into a sequence of sub-problems, each of which can be solved exactly and globally via a convex relaxation and the augmented Lagrangian method. Unlike related graph-cut approaches, the proposed convex-

relaxation solution can be parallelized to reduce substantially the computational time for 3D domains (or higher), extends directly to high dimensions, and does not have the grid-bias problem. The parallelized implementation on a GPU demonstrates that the proposed algorithm requires about 3.87 seconds for a typical cardiac MRI volume, a speed-up of about 5 times compared to a standard implementation. A performance evaluation is reported over 400 volumes acquired from 20 subjects, which shows that the obtained 3D surfaces correlate with independent manual delineations. I further demonstrate experimentally that (1) the performance of the algorithm is not significantly affected by the choice of the training subject; and (2) the shape description is used does not change significantly from one subject to another. These results support the fact that a single subject is sufficient for training the proposed algorithm.

2.2 Formulation

Multi-region segmentation of the LV is formulated following the principle of Bhattacharya distribution matching, which has recently led to outstanding results in the context of color image segmentation [Ayed et al. \[2010\]](#), [Pham et al. \[2011\]](#). The objectives of the approach consists of finding two target regions, the blood cavity (Ω_c) and myocardium (Ω_m), each matching given (*a priori* learned) model distributions of shape and intensity. The solutions were obtained following the optimization of two energy functionals, each containing three priors: (1) a distance-distribution matching prior that embeds shape information; (2) an intensity-distribution matching prior; and (3) a surface-smoothness prior to avoid the occurrence of small, isolated regions in the solutions. In the 2D case, a single user-provided segmentation of one frame in each 2D sequence of a given subject data-set is used to build the model distributions. In the 3D case, new variables and optimization steps are added to reduce the user inputs to two points (mouse

clicks), one placed at about the centroid of the cavity and the other on the myocardium region, both at the middle slice of the testing subject. The intensity model is learnt from a small region (a cylinder) centered at the user-provided click. For shape, the model distribution is learnt from only one 3D segmented volume (among the 20 phases) of a single training subject that is different from the testing subject. In both 2D and 3D cases, the optimization is constrained with a geometric condition ensuring the cavity region is enclosed within the myocardium ring.

2.2.1 The functional

Let $I : \Omega \subset \mathbb{R}^n (n \in \{2, 3\}) \rightarrow \mathcal{Z}_I \subset \mathbb{R}$ be an image function which maps 3D (or 2D) domain Ω to a finite set of intensity values \mathcal{Z}_I . Let $D : \Omega \subset \mathbb{R}^n (n \in \{2, 3\}) \rightarrow \mathcal{Z}_D \subset \mathbb{R}$ be a distance function which measures the distance between each point $x \in \Omega$ and a given point O , which corresponds approximately to the centroid of the cavity region:

$$D(x) = \|x - O\| : \Omega \rightarrow \mathcal{Z}_D \subset \mathbb{R} \quad (2.1)$$

In the 3D case, O is obtained from a very simple user input that amounts to a click at about the centroid of the cavity within a middle slice. Such simple input yields an approximation of the centroid of the cavity in the 3D volume. In the 2D case, O is the centroid of the cavity in the first frame whose segmentation is assumed given.

The objective is to find optimal cavity (\hat{R}_c) and myocardium (\hat{R}_m) regions which match given (*a priori* learned) model distributions of intensities and distances. I solve the following

optimization problem:

$$\{\hat{\mathcal{R}}_c, \hat{\mathcal{R}}_m\} = \arg \min_{\mathcal{R}_c, \mathcal{R}_m} \underbrace{-\mathcal{D}_c(\mathcal{R}_c) - \mathcal{D}_m(\mathcal{R}_m)}_{\text{Distribution matching}} + \lambda \underbrace{\left(\int_{\partial \mathcal{R}_c} C(x) dx + \int_{\partial \mathcal{R}_m} C(x) dx \right)}_{\text{Smoothness/Edge}} \quad (2.2)$$

with \mathcal{D}_c and \mathcal{D}_m given by:

$$\mathcal{D}_c(\mathcal{R}_c) = \alpha_c \underbrace{\mathcal{B}(\mathcal{P}^I(\mathcal{R}_c, \cdot), \mathcal{M}_c^I)}_{\text{Cavity-intensity Prior}} + (1 - \alpha_c) \underbrace{\mathcal{B}(\mathcal{P}^D(\mathcal{R}_c, \cdot), \mathcal{M}_c^D)}_{\text{Cavity-shape prior}} \quad (2.3)$$

$$\mathcal{D}_m(\mathcal{R}_m) = \alpha_m \underbrace{\mathcal{B}(\mathcal{P}^I(\mathcal{R}_m, \cdot), \mathcal{M}_m^I)}_{\text{Myocardium-intensity Prior}} + (1 - \alpha_m) \underbrace{\mathcal{B}(\mathcal{P}^D(\mathcal{R}_m, \cdot), \mathcal{M}_m^D)}_{\text{Myocardium-shape Prior}} \quad (2.4)$$

subject to the following geometrical constraint which ensures the cavity is enclosed within the myocardium ring:

$$\mathcal{R}_c \subset \mathcal{R}_m$$

Below is a detailed description of the notations, variables and functionals that appear in the optimization problem which is defined in (2.2), (2.3) and (2.4):

- For an image $J \in \{I, D\} : \Omega \subset \mathbb{R}^n (n \in \{2, 3\}) \rightarrow \mathcal{Z}_J$, and for any region $\mathcal{R} \in \Omega$, $\mathcal{P}^J(\mathcal{R}, \cdot)$ is the kernel density estimate of the distribution of data J within region \mathcal{R} :

$$\mathcal{P}^J(\mathcal{R}, z) = \frac{\int_{\mathcal{R}} \mathcal{K}_z(J(x)) dx}{|\mathcal{R}|} \quad \forall z \in \mathcal{Z} \quad (2.5)$$

with $|\mathcal{R}|$ the area of region \mathcal{R} , i.e. $|\mathcal{R}| = \int_{\mathcal{R}} dx$; $\mathcal{K}_z(\cdot)$ is a kernel function, typically

Gaussian:

$$\mathcal{K}_z(y) = \frac{1}{(2\pi\sigma^2)^{(n/2)}} \exp\left(-\frac{\|z - y\|^2}{2\sigma^2}\right) \quad (2.6)$$

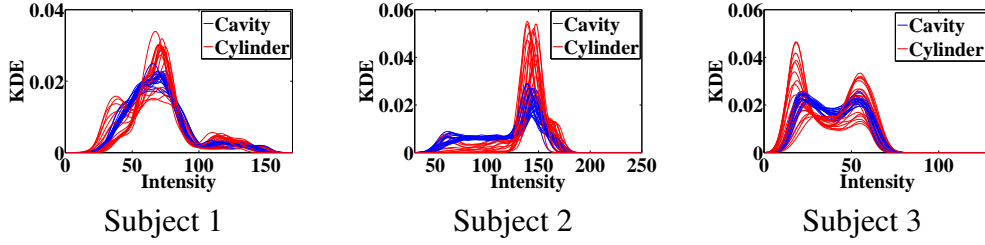


Figure 2.1: Red curves: the intensity distributions learned from the user click (i.e., using the image data within a small cylinder centered at the user click). Blue curves: the actual cavity distributions estimated from the ground truth. The distributions for three subjects and all the phases of a cardiac cycle are plotted.

- $\mathcal{B}(f, g)$ is the Bhattacharya measure of similarity between two distributions f and g :

$$\mathcal{B}(f, g) = \sum_{z \in \mathcal{Z}} \sqrt{f(z)g(z)}, \quad \mathcal{Z} \in \{\mathcal{Z}_I, \mathcal{Z}_D\} \quad (2.7)$$

\mathcal{B} is always in $[0, 1]$, with 1 indicating a perfect match between the distribution and 0 a total mismatch.

- \mathbf{M}_c^I is a model distribution of cavity intensity. In the 2D case, \mathbf{M}_c^I is estimated from intensity data within a user-provided delineation of the cavity in the first frame of the considered sequence. In the 3D case, \mathcal{M}_c^I is learned from intensity data within a small cylinder centered at \mathcal{O} . The radius of the cylinder, d , is a free parameter which has to be fixed experimentally. The red curves in Fig. 2.1 depict the intensity distributions learned from the user click (i.e., from a small cylinder). The blue curves correspond to the actual cavity distributions estimated from the ground truth. I plot the distributions for three subjects and all the phases of a cardiac cycle. Note that the learned distributions, although obtained from a small region around the user click, do not differ significantly from the actual (ground-truth) distributions patterns. Notice also that both learned and actual

distributions do not change significantly during a cardiac cycle; they are not affected by the changes in cavity size and shape within different cardiac phases (systolic to diastolic). Therefore, a user click in a single frame and the surrounding-neighborhood data were sufficient to learn a reliable intensity model.

- \mathcal{M}_c^D is a model distribution of distances within the cavity, i.e., a cavity-shape model. In the 3D case, this model is learned from a single training subject different from the testing subject. In the 2D case, it is estimated from distance data within a user-provided delineation of the cavity in the first frame of the considered sequence.
- \mathcal{M}_m^I is a model distribution of myocardium intensity. In the 3D case, \mathcal{M}_m^I is learned from intensity data within a small cylinder centered at a user point placed on the myocardium region.
- \mathcal{M}_m^D is a model distribution of distances within the myocardium from centroid, i.e., a myocardium-shape model. In the 3D case, this model is learned from a manual segmentation of a single training subject different from the testing subject. In the 2D case, it is estimated from distance data within a user-provided myocardium region in the first frame of the considered sequence.
- $|\partial\mathcal{R}|$ denotes the perimeter of region ($\mathcal{R} \in \mathcal{R}_c, \mathcal{R}_m$).
- C is a standard edge-indicator function evaluated at each point as follows:

$$C(x) = \frac{1}{1 + \beta \nabla(I(x))} \quad (2.8)$$

For $\beta = 0$, $C(x)$ becomes equal to 1 and the smoothness/edge term becomes equal to the

standard penalty on boundary/surface length.

- α_c , α_m , and λ are positive constants that weigh the relative contribution of each of the terms in the functionals. β is a positive constant balancing the contribution of the image gradient.

The typical example in Fig. 2.2 demonstrates the relevance of the functional in (2.2) to cardiac image segmentation. It shows the evolution of the segmentation and the corresponding distributions during an iterative distribution matching process. Each column depicts a different step. In the first column, the initial contour (green curve) is shown in (a1) and the corresponding intensity and distance distributions (green plots) in (a2) and (a3), respectively. Similarly, the second and third columns show the segmentations/distributions at an intermediate step and at convergence respectively. At initialization, the distributions of the current segmentation (green plots) are different from the target models (red plots). These distributions vary during optimization until they match the models (see second and third column). The red curve in (a1, b1, c1) corresponds to the ground-truth segmentation.

Introducing a scale variable

The distance-distribution prior is intrinsically invariant with respect to translation and rotation, but not with respect to scale (or size) of the cavity and myocardium regions. To illustrate this, Fig. 2.3 shows the distance distributions corresponding to the ground-truth segmentations of two different subjects, assuming one is the testing subject and the other is the training subject. The figure demonstrates that the distance distributions have similar Gaussian shapes, but shifted supports. This shift is due to inter-subject variations in scale (or size). To account for such

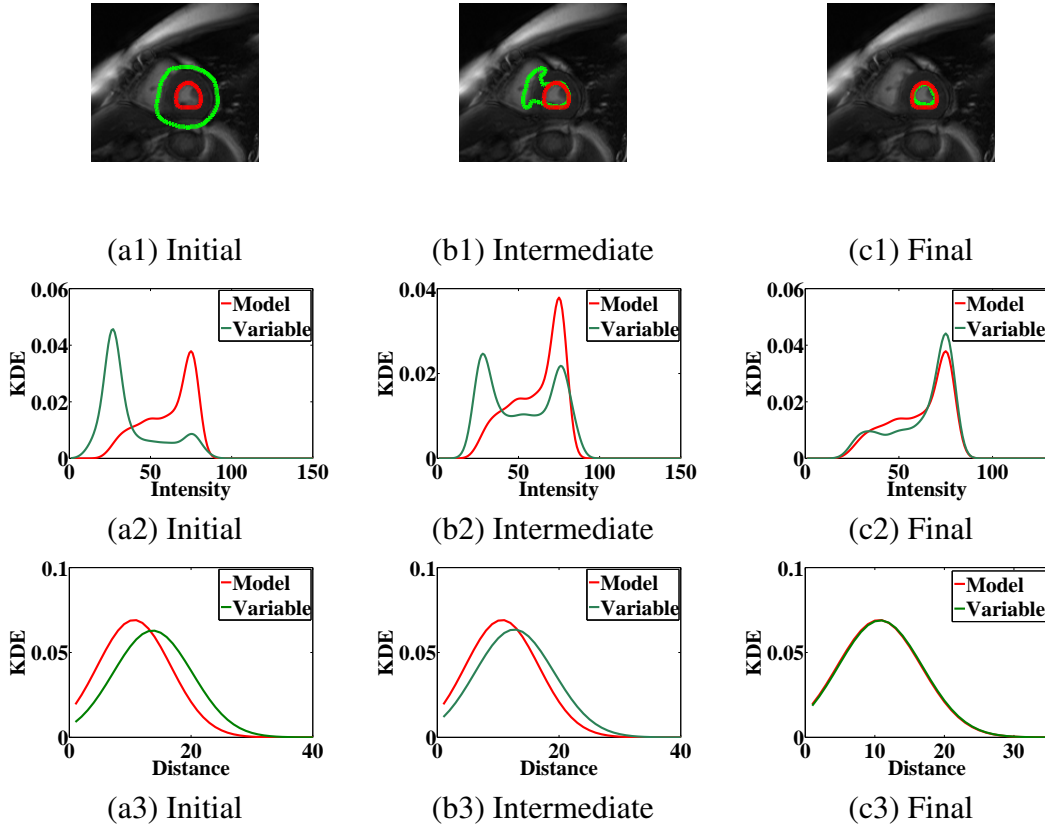


Figure 2.2: A typical example, which illustrates the evolution of the segmentation and the corresponding distributions during an iterative distribution matching process.

shifts, a scale variable introduced in each of the model distributions of distances:

$$\begin{aligned}
 \mathcal{M}_c^D(\cdot, s_c) : \mathcal{Z}_D \times \mathbb{R} &\rightarrow [0, 1] / \mathcal{M}_c^D(z, s_c) = \mathcal{M}_c^D(z + s_c), s_c \in \mathbb{R} \\
 \mathcal{M}_m^D(\cdot, s_m) : \mathcal{Z}_D \times \mathbb{R} &\rightarrow [0, 1] / \mathcal{M}_m^D(z, s_m) = \mathbf{M}_m^D(z + s_m), s_m \in \mathbb{R}
 \end{aligned} \tag{2.9}$$

Thus, to account for these new scale variables, the shape priors in (2.3) and (2.4) are replaced by scale-dependent priors as follows:

$$\begin{aligned}
 \mathcal{B}(\mathcal{P}^D(\mathcal{R}_c, \cdot), \mathcal{M}_c^D) &\rightarrow \mathcal{B}(\mathcal{P}^D(\mathcal{R}_c, \cdot), \mathcal{M}_c^D(\cdot, s_c)) \\
 \mathcal{B}(\mathcal{P}^D(\mathcal{R}_m, \cdot), \mathcal{M}_m^D) &\rightarrow \mathcal{B}(\mathcal{P}^D(\mathcal{R}_m, \cdot), \mathcal{M}_m^D(\cdot, s_m))
 \end{aligned} \tag{2.10}$$

Therefore, s_c and s_m become variables that have to be optimized along with the segmentation regions. With these new variables, the optimization problem becomes:

$$\begin{aligned} \{\hat{\mathcal{R}}_c, \hat{\mathcal{R}}_m, \hat{s}_c, \hat{s}_m\} &= \arg \min_{\mathcal{R}_c, \mathcal{R}_m, s_c, s_m} -\mathcal{D}_c(\mathcal{R}_c, s_c) - \mathcal{D}_m(\mathcal{R}_m, s_m) \\ &+ \lambda \left(\int_{\partial \mathcal{R}_c} C(x) dx + \int_{\partial \mathcal{R}_m} C(x) dx \right) \\ \text{s.t. } &\mathcal{R}_c \subset \mathcal{R}_m \end{aligned} \quad (2.11)$$

with \mathcal{D}_c and \mathcal{D}_m given by:

$$\mathcal{D}_c(\mathcal{R}_c, s_c) = \alpha_c \mathcal{B}(\mathcal{P}^I(\mathcal{R}_c, \cdot), \mathcal{M}_c^I) + (1 - \alpha_c) \mathcal{B}(\mathcal{P}^D(\mathcal{R}_c, \cdot), \mathcal{M}_c^D(\cdot, s_c)), \quad (2.12)$$

$$\mathcal{D}_m(\mathcal{R}_m, s_m) = \alpha_m \mathcal{B}(\mathcal{P}^I(\mathcal{R}_m, \cdot), \mathcal{M}_m^I) + (1 - \alpha_m) \mathcal{B}(\mathcal{P}^D(\mathcal{R}_m, \cdot), \mathcal{M}_m^D(\cdot, s_m)) \quad (2.13)$$

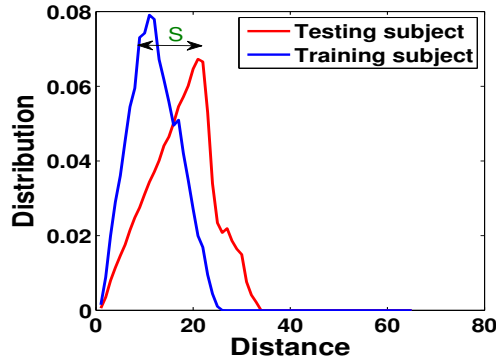


Figure 2.3: The distance distribution of the training subject (blue) and the testing subject (red).

2.2.2 Two-step optimization procedure

The model has two different types of variables: the segmentation regions and the scale variables. An iterative two-step optimization procedure is adopted. First, the scale variables are

fixed and the proposed energies are optimized with respect to the regions via convex relaxation. Then, we optimize over the scale variables via fixed-point computations, with the regions fixed.

Convex-relaxation optimization with respect to the regions

The optimization is split with respect to the regions in (2.2) into two sub-problems:

For each k -iteration (superscript k is added to the region notation and omit the scale variables at this stage to simplify the presentation):

- Fix \mathcal{R}_m^k and optimize (2.2) over \mathcal{R}_c by

$$\mathcal{R}_c^{k+1} := \arg \min_{\mathcal{R}_c} -\mathcal{D}_c(\mathcal{R}_c) + \lambda \int_{\partial \mathcal{R}_c} C(x) dx, \quad \text{s.t. } \mathcal{R}_c \subset \mathcal{R}_m^k \quad (2.14)$$

- Fix \mathcal{R}_c^{k+1} and optimize (2.2) over \mathcal{R}_m by

$$\mathcal{R}_m^{k+1} := \arg \min_{\mathcal{R}_m} -\mathcal{D}_m(\mathcal{R}_m) + \lambda \int_{\partial \mathcal{R}_m} C(x) dx, \quad \text{s.t. } \mathcal{R}_c^{k+1} \supset \mathcal{R}_m \quad (2.15)$$

Sub-problems (2.14) and (2.15) are optimization problems of the same general form:

$$\arg \min_{\mathcal{R}} \left\{ E(\mathcal{R}) := -\mathcal{B}(\mathcal{P}^J, \mathcal{M}) + \lambda \int_{\partial \mathcal{R}} C(x) dx \right\} \quad (2.16)$$

Here \mathcal{M} is the fixed model (the super- and sub-scripts that were defined for \mathcal{M} previously are omitted to simplify further presentation and notations). Also, in (2.16), it is assumed that there is only one Bhattacharya measure to simplify subsequent presentation and notations. Once the problem in (2.16) is solved, extension to a weighted sum of Bhattacharyya measures, as is the

case in (2.14) and (2.15), becomes straightforward.

Let $u : \Omega \rightarrow \{0, 1\}$ be the indicator function of $\mathcal{R} \subset \Omega$, i.e., $u(x) = 1$ when $x \in \mathcal{R}$ and $u(x) = 0$ otherwise. Using u , the distribution in (2.5) can be rewritten as follows:

$$\mathcal{P}^J(\mathcal{R}, z) = \frac{\int_{\Omega} \mathcal{K}_z(J(x))u(x) dx}{\int_{\Omega} u(x) dx} \quad \forall z \in \mathcal{Z}, \quad (2.17)$$

and the Bhattacharya similarity as follows:

$$\mathcal{B}(\mathcal{P}^J, \mathcal{M}) = \mathbf{B}(u, \mathcal{M}) = \sum_{z \in \mathcal{Z}} \left(\frac{\int_{\Omega} \mathcal{T}_{M,z}(x)u(x) dx}{\int_{\Omega} u(x) dx} \right)^{1/2} \quad (2.18)$$

where $\mathcal{T}_{M,z}(x) = \mathcal{K}_z(J(x))\mathcal{M}(z)$. Here \mathcal{M} is a fixed model that the algorithm learns either from a training subject or from user inputs. It can be either a distance or intensity distribution, for cavity or myocardium (the super- and sub-scripts for \mathcal{M} are omitted for simplicity).

The smoothness/edge term can be evaluated by the weighted total-variation of indicator function u [Chan and Shen \[2005\]](#), [Giusti \[1977\]](#):

$$\int_{\partial \mathcal{R}} C(x) dx = \int_{\Omega} C(x) |\nabla u(x)| dx, \quad C(x) \geq 0 \quad (2.19)$$

Using (2.18) and (2.19), the (2.16) is reformulated in terms of the binary valued labeling function u :

$$\arg \min_{u(x) \in \{0,1\}} \{E(u) := - \sum_{z \in \mathcal{Z}} \left(\frac{\int_{\Omega} \mathcal{T}_{M,z}(x)u(x) dx}{\int_{\Omega} u(x) dx} \right)^{1/2} + \int_{\Omega} C(x) |\nabla u(x)| dx\}. \quad (2.20)$$

Global Minimization of Energy Upper Bound

Direct computation of (2.20) is a very challenging optimization problem, both theoretically and numerically, due to the constraint of a pointwise binary valued variable and the high non-convexity of the energy. (2.20) is non-convex even when $u \in \{0, 1\}$ is relaxed by $u \in [0, 1]$.

A novel iterative convex-relaxation solution is proposed to (2.20), which globally minimizes a sequence of upper bounds of $E(u)$, denoted $E^{i+1}(u; u^i)$, $i = 1 \dots$:

$$u^{i+1} = \arg \min_{u \in \{0,1\}} E^{i+1}(u; u^i), \quad i = 1 \dots \quad (2.21)$$

where

$$E(u) \leq E^{i+1}(u; u^i), \quad i = 1 \dots \quad (2.22)$$

and

$$E(u) = E^{i+1}(u; u^i) \quad (2.23)$$

One can show that the sequence of solutions u^i to the problems in (2.21) under constraints (2.22) and (2.23) yields a monotonically decreasing sequence of cost functions E and, therefore, a minimum of E at convergence. This follows directly from the following two propositions.

Proposition 1. *Sequence $E(u^i)$ is monotonically decreasing: $E(u^{i+1}) \leq E(u^i)$.*

Proposition 2. *Sequence $E(u^i)$ is convergent.*

Proof of proposition 1

Applying constraint (2.23) to $u = u^i$ gives

$$E(u^i) = E^{i+1}(u^i, u^i) \quad (2.24)$$

Now, by definition of minimum in (2.21), we have

$$E^{i+1}(u^{i+1}, u^i) \leq E^{i+1}(u^i, u^i) \quad (2.25)$$

combining (2.24) and (2.25) gives

$$E^{i+1}(u^{i+1}, u^i) \leq E(u^i) \quad (2.26)$$

Also, applying constraint (2.22) to $u = u^{i+1}$ gives

$$E(u^{i+1}) \leq E^{i+1}(u^{i+1}, u^i) \quad (2.27)$$

Finally, combining (2.26) and (2.27) proves 1.

Appendix B: Proof of proposition 2

$E(u^i)$ is monotonically decreasing and lower bounded, because the Bhattacharyameasure is upper bounded by one. Therefore $E(u^i)$ converges.

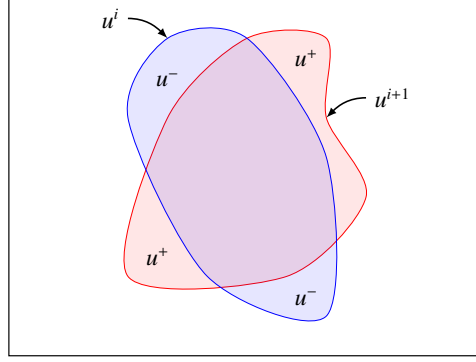


Figure 2.4: Iterative bound optimization: u^i denotes the labeling at iteration i .

2.2.3 Energy Upper Bounds

In this section, an energy upper bound $E^{i+1}(u; u^i)$ is derived. It will be further shown in subsequent sections that $E^{i+1}(u; u^i)$ can be minimized *globally* and *exactly* over $u \in \{0, 1\}$ via convex optimization.

Let $u^i \in \{0, 1\}$ denote the binary labeling function, obtained at the previous i -th step, as the starting point of the $i + 1$ -th iteration. At this stage, we seek an optimal labeling function $u \in \{0, 1\}$ which minimizes the energy upper bound. Let express the difference between u and the given $u^i \in \{0, 1\}$ as a function of two new variables $u^+ \in \{0, 1\}$ and $u^- \in \{0, 1\}$ (refer to Fig. 2.4 for an illustration):

1. u^+ indicates the area where u^i is 0 and u becomes 1, i.e., area increase:

$$u^+(x) := \begin{cases} u(x), & \text{where } u^i(x) = 0 \\ 0, & \text{otherwise} \end{cases} \quad (2.28)$$

2. u^- indicates the area where u^i is 1 and u becomes 0, i.e., area decrease:

$$u^-(x) := \begin{cases} 1 - u(x), & \text{where } u^i(x) = 1 \\ 0, & \text{otherwise} \end{cases} \quad (2.29)$$

The Bhattacharya measure (2.18) can then be rewritten in terms of u^+ and u^- as follows:

$$\mathbf{B}(u, \mathcal{M}) = \sum_{z \in \mathcal{Z}} \left(\frac{\int_{\Omega} (\mathcal{T}_{M,z} u^i + \mathcal{T}_{M,z} u^+ - \mathcal{T}_{M,z} u^-) dx}{\int_{\Omega} (u^i + u^+ - u^-) dx} \right)^{1/2}. \quad (2.30)$$

The following describes the upper bound I propose.

Proposition 3. *Given a labeling $u^i \in \{0, 1\}$, for any labeling function $u \in \{0, 1\}$, I have the following upper bound which depends on u^+ and u^- :*

$$E(u) \leq -\mathbf{B}(u^i, \mathcal{M}) + F^{i+1}(u; u^i) \quad (2.31)$$

where

$$F^{i+1}(u; u^i) = \int_{\Omega} C_v^i u^- dx + \int_{\Omega} C_w^i u^+ dx + \int_{\Omega} C |\nabla u| dx \quad (2.32)$$

and

$$C_v^i(x) = \sum_{z \in \mathcal{Z}} \frac{\mathbf{D}_{z,i} \mathcal{T}_{M,z}(x)}{\int_{\Omega} \mathcal{T}_{M,z}(x) u^i(x) dx}; \quad (2.33)$$

$$C_w^i(x) = \sum_{z \in \mathcal{Z}} \frac{\mathcal{D}_{z,i}}{2 \int_{\Omega} u^i(x) dx}; \quad (2.34)$$

$$\mathcal{D}_{z,i} = \left(\frac{\int_{\Omega} \mathcal{T}_{M,z}(x) u^i(x) dx}{\int_{\Omega} u^i(x) dx} \right)^{1/2} \quad (2.35)$$

Notice that $\mathbf{B}(u^i, \mathcal{M})$ is a constant corresponding to the given u^i . Therefore, using the results in propositions 1, 2 and 3, E can be minimized by solving the following problem at each iteration i :

$$\min_{u \in \{0,1\}} F^{i+1}(u; u^i) \quad (2.36)$$

where $F^{i+1}(u; u^i)$ is given in (2.32).

Convex-relaxation optimization of energy upper bound

Let Ω_s and Ω_t be two disjoint domains given by the current labeling function $u^i \in \{0, 1\}$:

$$\Omega = \Omega_s \cup \Omega_t, \quad \Omega_s \cap \Omega_t = \emptyset \quad (2.37)$$

where Ω_s is indicated by $u^i = 1$ and Ω_t by $u^i = 0$. From the definitions of u^+ (2.28) and u^- (2.29), (2.36) is reformulated by:

$$\arg \min_{u(x) \in \{0,1\}} \int_{\Omega_t} C_v^i(1-u) dx + \int_{\Omega_s} C_w^i u dx + \int_{\Omega} C |\nabla u| dx \quad (2.38)$$

Model (2.38) is non-convex due to the binary-valued constraint $u \in \{0, 1\}$, which is relaxed to a continuous (convex) interval $[0, 1]$. Thus, (2.38) is replaced by the following convex optimization problem:

$$\arg \min_{u(x) \in [0,1]} \int_{\Omega_t} C_v^i (1 - u) dx + \int_{\Omega_s} C_w^i u dx + \int_{\Omega} C |\nabla u| dx \quad (2.39)$$

Similar convex relaxations have been recently shown to be effective in solving the classical piecewise-constant segmentation model (e.g. [Yuan et al. \[2010\]](#)).

To solve (2.39) efficiently via convex optimization [Bertsekas \[1999\]](#), [Rockafellar and Wets \[1998\]](#), let us first consider the following proposition:

Proposition 4. *The optimization problem in (2.39) is equivalent to the following constrained optimization problem:*

$$\begin{aligned} \max_{p_s, p_t, p} \int_{\Omega_s} p_s dx \quad & \text{s.t.} \\ -p_s(x) + \operatorname{div} p(x) &= 0 \text{ a.e. } x \in \Omega_s; \\ p_t(x) + \operatorname{div} p(x) &= 0 \text{ a.e. } x \in \Omega_t; \\ p_s(x) &\leq C_v^i(x) \text{ a.e. } x \in \Omega_s; \\ p_t(x) &\leq C_w^i(x) \text{ a.e. } x \in \Omega_t; \\ |p(x)| &\leq C(x) \text{ a.e. } x \in \Omega \end{aligned} \quad (2.40)$$

where $p : \Omega \rightarrow \mathbf{R}$, $p_s : \Omega \rightarrow \mathbf{R}$ and $p_t : \Omega \rightarrow \mathbf{R}$ are variables in the form of scalar functions defined over the image domain.

Proposition 4 allows us to derive an efficient multiplier-based algorithm for optimizing (2.39) with respect to u . The algorithm is based on the standard augmented Lagrangian method Bertsekas [1999]. The following augmented Lagrangian function ($c > 0$) is defined:

$$L_c(p_s, p_t, p, u) = \int_{\Omega_s} p_s dx + \int_{\Omega_s} (\operatorname{div} p - p_s)u dx + \int_{\Omega_t} (\operatorname{div} p + p_t)u dx - \frac{c}{2} \|\operatorname{div} p - p_s\|_{\Omega_s}^2 - \frac{c}{2} \|\operatorname{div} p + p_t\|_{\Omega_t}^2 \quad (2.41)$$

A summary of the algorithm appears below in Alg.2 (i is the iteration number and the steps below are repeated until convergence).

Algorithm 1 Augmented-Lagrangian optimization

- $i = 0$: Initialize flows p_s^0, p_t^0, p^0 and labeling $u^0 \in \{0, 1\}$. Then start $i + 1$ -th iteration;
- Fix p^i and u^i and maximize in a closed form $L_c(p_s, p_t, p, u^i)$ over p_s and p_t :

$$(p_s^{i+1}, p_t^{i+1}) := \arg \max_{p_s, p_t} L_c(p_s, p_t, p^i, u^i);$$

- Fix p_s^{i+1}, p_t^{i+1} and u^i and maximize iteratively $L_c(p_s, p_t, p, u^i)$ over p (This can be solved by the Chambolle's projection algorithm Chambolle [2004]):

$$p^{i+1} := \arg \max_p L_c(p_s^{i+1}, p_t^{i+1}, p, u^i);$$

- Update labeling function u^i by:

$$u^{i+1}(x) = \begin{cases} u^i(x) + c (\operatorname{div} p^{i+1}(x) - p_s^{i+1}(x)), & \forall x \in \Omega_s \\ u^i(x) + c (\operatorname{div} p^{i+1}(x) + p_t^{i+1}(x)), & \forall x \in \Omega_t \end{cases} .$$

2.2.4 Exactness of the Convex Relaxed Min-Cut Model in (2.39)

In this section, it is demonstrated that the binary-valued optimization problem in (2.38) can be solved globally and exactly by its convex relaxation in (2.39). Clearly, (2.39) is convex. Let $u^*(x)$ be its global optimum. For any $\gamma \in [0, 1]$, the γ is defined as upper level set $u_\gamma^*(x) \forall x \in \Omega$ by

$$u_\gamma^*(x) = \begin{cases} 1, & \text{when } u^*(x) > \gamma \\ 0, & \text{when } u^*(x) \leq \gamma \end{cases}, \quad (2.42)$$

Proposition 5. *When $u^*(x)$ gives one global optimum of (2.39), its thresholding $u_\gamma^*(x) \in \{0, 1\}$ by (2.42), for any $\gamma \in [0, 1]$, solves the binary-valued optimization problem in (2.38) globally and exactly.*

The proof of proposition.5 follows the ideas in [Nikolova et al. \[2006\]](#).

Optimization with respect to the scale variable

In this step, the labeling (segmentation) variables is fixed and the energy functions are optimized with respect to scale variables s_c and s_m . Considering the expressions of \mathcal{D}_c and \mathcal{D}_m in Eqs. (2.12) and (2.13), this amounts to solving two optimization sub-steps of the following general form:

$$s^{opt} = \arg \min_s \mathcal{B}(\mathcal{P}^D(\mathcal{R}, \cdot), \mathcal{M}^D(\cdot, s)) \quad \text{with} \\ s \in \{s_c, s_m\}; \mathcal{R} \in \{\mathcal{R}_c, \mathcal{R}_m\}; \mathcal{M}^D \in \{\mathcal{M}_c^D, \mathcal{M}_m^D\} \quad (2.43)$$

Note that the intensity priors are omitted as they are constants with respect to the scale variables.

Now, considering a variable change $z \leftarrow z - s$, we have the following derivative of (2.43) with respect to s :

$$\begin{aligned} \frac{\partial \mathcal{B}(\mathcal{P}^D(\mathcal{R}, \cdot), \mathcal{M}^D(\cdot, s))}{\partial s} &= \frac{\partial \sum_{z \in \mathcal{Z}_D} \sqrt{\mathcal{P}^D(\mathcal{R}, z) \mathcal{M}^D(z + s)}}{\partial s} \\ &= \sum_{z \in \mathcal{Z}_D} \frac{\partial \mathcal{P}^D(\mathcal{R}, z - s)}{\partial s} \sqrt{\frac{\mathcal{M}^D(z)}{2\mathcal{P}^D(\mathcal{R}, z - s)}} \end{aligned} \quad (2.44)$$

Using the kernel density estimate in (2.5), we also have:

$$\begin{aligned} \frac{\partial \mathcal{P}^D(\mathcal{R}, z - s)}{\partial s} &= \frac{\sum_{x \in \mathcal{R}} \frac{\partial K_z(s + D(x))}{\partial s}}{|\mathcal{R}|} \\ &= \frac{\sum_{x \in \mathcal{R}} (z - s - D(x)) K_z(s + D(x))}{\sigma^2 |\mathcal{R}|} \end{aligned} \quad (2.45)$$

Embedding (2.45) in (2.44), setting the obtained expression to zero, and after some manipulations, the following necessary condition is obtained for a minimum of E with respect to s :

$$\begin{aligned} s - g(s) &= 0 \text{ where} \\ g(s) &= \frac{\sum_{z \in \mathcal{Z}_D} \sum_{x \in \mathcal{R}} (z - D(x)) K_z(D(x) + s) \sqrt{\frac{\mathcal{M}^D(z)}{\mathcal{P}^D(\mathcal{R}, z - s)}}}{\sum_{z \in \mathcal{Z}_D} \sum_{x \in \mathcal{R}} K_z(D(x) + s) \sqrt{\frac{\mathcal{M}^D(z)}{\mathcal{P}^D(\mathcal{R}, z - s)}}} \end{aligned} \quad (2.46)$$

Note that since the necessary condition in (2.46) has the form of a FPE, the solution can be

obtained by iterating the following FPEs:

$$s^{n+1} = g(s^n), \quad n = 1, 2, \dots \quad (2.47)$$

Let s^{opt} be the limit of sequence s^n at convergence. Then the s^{opt} is obtained as follows,

$$s^{opt} = \lim_{n \rightarrow +\infty} s^{n+1} = \lim_{n \rightarrow +\infty} g(s^n) = g(\lim_{n \rightarrow +\infty} s^n) = g(s^{opt}) \quad (2.48)$$

Consequently, s_{opt} is a solution of the necessary condition obtained in (2.46).

2.3 Experiments

The proposed 2D/3D convex relaxation (CR) methods were evaluated over a dataset containing short axis cardiac cine MRI volumes of 20 subjects (20 volumes per subject, each corresponding to a cardiac phase, i.e., 400 volumes were used in total). Three sets of comprehensive experiments are performed:

- Standard quantitative evaluations of the obtained results in comparisons with independent manual segmentations and other recent related graph-cut and level-set methods [Ayed et al. \[2009a, 2012, 2009b\]](#).
- Experimental evaluations which demonstrate: (1) The performance of the 3D algorithm is not significantly affected by the choice of the training subject (Table. 2.3); and (2) The shape description does not change significantly from one subject to another (Figure 2.9).

These results support the fact that a single subject is sufficient for training the proposed

algorithm.

- Computational evaluations which demonstrate that the parallelized computations run on a GPU (NVIDIA Tesla C1600) can bring a speed-up for a typical cardiac MRI volume.

2.3.1 Visual samples of the 2D/3D results

2D examples:

Fig. 2.5 shows the segmentation results of mid-cavity, apical, and basal slices for two subjects. The yellow and red curves correspond to the endo- and epicardium boundaries, respectively. The mid-cavity examples show how the proposed method can exclude the papillary muscles from the myocardium. The last row shows apical frames where it is challenging to segment the cavity as it is a small region with motion artifacts. The results also demonstrate that the proposed shape prior can tolerate variations in cavity scale and shape, although the training is based on a single segmentation (the first frame of the slice).

3D example:

Fig. 2.6 shows 3D segmentation results of one subject for the endo- and epicardium. I depict a 3D illustration of the obtained results and the manual surfaces, along with the corresponding 2D contours/frames from three representative slices.

2.3.2 Computational evaluations

The parallelized implementation was performed on an NVIDIA Tesla C1600 GPU, and the non-parallelized version on a 2.13 GHz Xeon (E5506), with 6 GB of RAM. The GPU (paral-

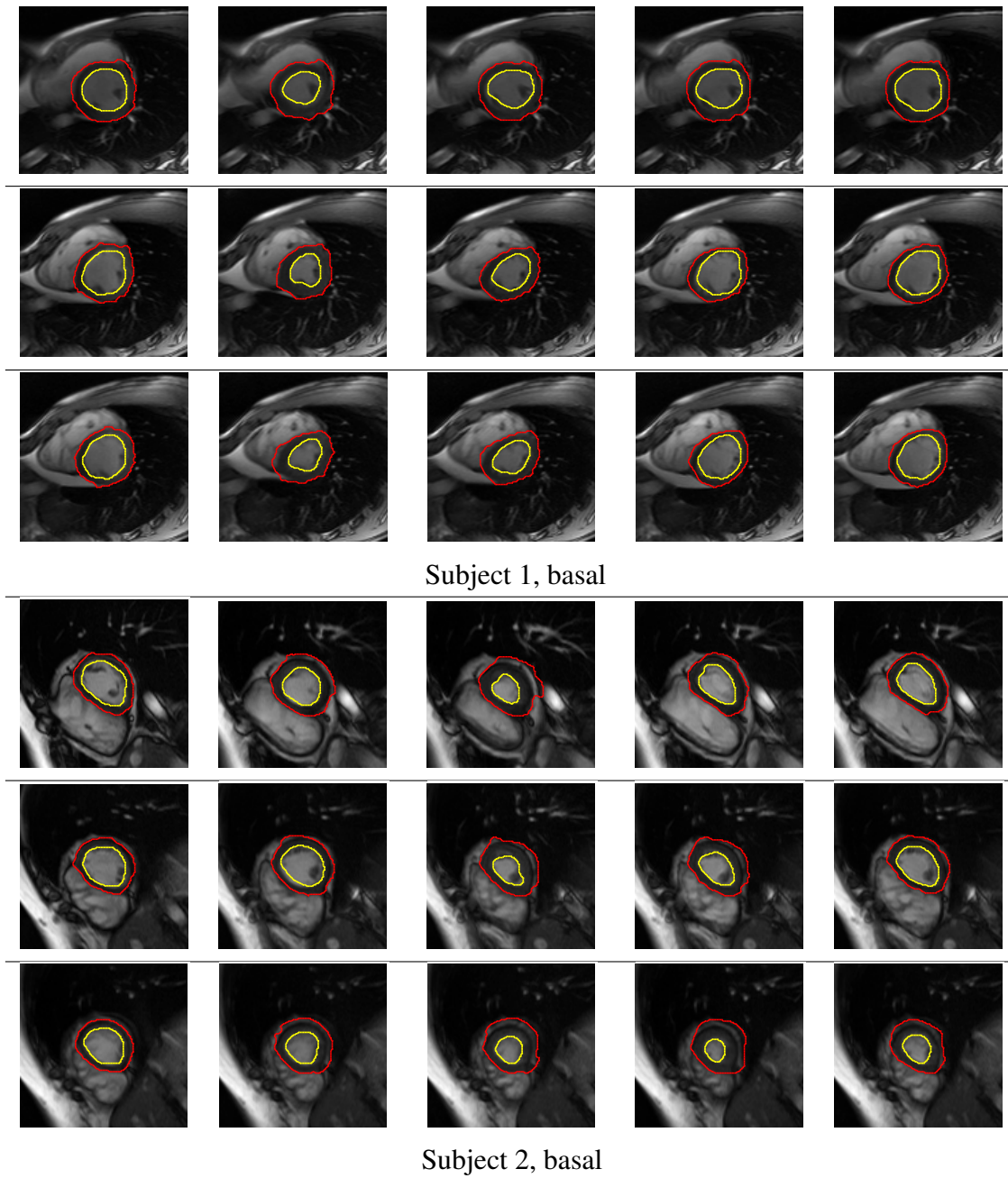


Figure 2.5: Results for two subjects from diastolic to systolic phases (left to right) for basal, mid-cavity and apical slices (top to bottom). The yellow contour delineates the cavity region, and the region between red and yellow contours delineates the myocardium.

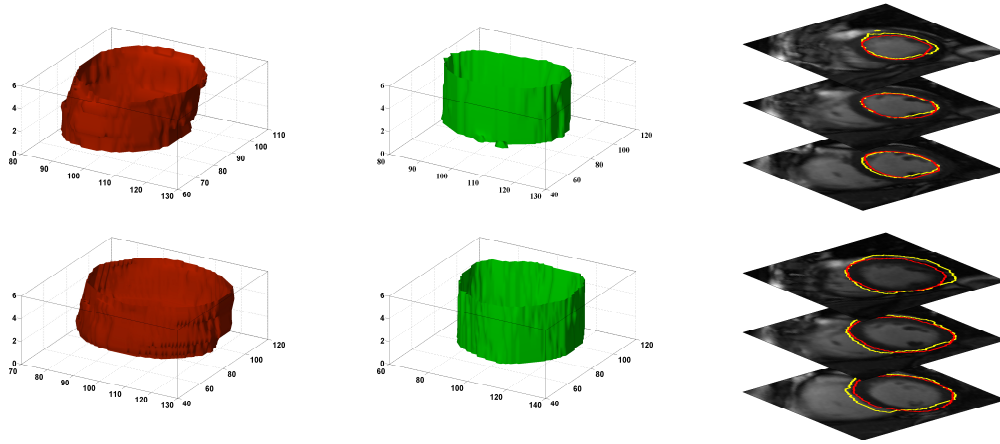


Figure 2.6: Manual segmentation (red; 1st column): (1st line) endocardium and (2nd line) Epicardium surfaces; Result of the proposed algorithm (green; 2nd column): (1st line) Endo- and (2nd line) Epicardium surfaces; (3rd column): Corresponding 2D automatic (yellow) and manual (red) contours superimposed on 2D frames.

lized) implementation demonstrates that the proposed algorithm requires about 3.87 seconds for a typical cardiac MRI volume (6 slices), a speed-up of about 5 times compared to the CPU implementation (19.3 sec/volume).

Quantitative and comparative performance evaluations

The parameters: In the 2D case, the model distributions were learned from a manual segmentation of the first frame in each cardiac slice. The following parameters were used for all the data: $\sigma = 10^{-1}$ for the intensity distributions of the myocardium, $\sigma = 10$ for the intensity distributions of the cavity, and $\sigma = 2$ for the distance distributions in (2.6); $\alpha_c = 0.95$; $\alpha_m = 0.6$; $\lambda = 0.3$; and $c = 0.05$.

In the 3D case, a single randomly chosen subject was used for training and the rest of the subjects were used for testing. For the training subject, only one 3D volume (among the 20 phases) should be fully segmented for each of the two target regions (cavity and myocardium).

The training volume is used to learn the shape model. For each testing subject, the user input is one single point per target region (cavity or myocardium), i.e., two mouse clicks in total for the whole 3D+time dataset. A user selected point placed at about the centroid of the cavity (in a middle slice) is used to compute the distance images (for both cavity and myocardium) as well as the intensity model for the cavity. Another such point placed on the myocardium region is used to learn the intensity model of the myocardium ring. Both intensity models were computed from the testing-subject data within small cylinders centered at the user-provided points, each having a radius of 4 pixels. The following parameters were invariant for all the data: $\sigma = 0.28$ for the intensity distributions of the myocardium, $\sigma = 4$ for the intensity distributions of the cavity and $\sigma = 6$ for the distance distributions; $\alpha_c = \alpha_m = 0.04$; $\lambda = 1$ and $\beta = 75$. For all subjects, a random initialization is used, which amounts to a cube centered at the middle of the image and whose size is $2/3$ that of the image dimensions.

Evaluations: I assessed the similarities between the ground truth and the segmentations via a contour-based measure, the Root Mean Squared Error (*RMS E*) [Ayed et al. \[2009b\]](#), and a region-based measure, the Dice Metric (*DM*) [Ayed et al. \[2009a, 2012\]](#). Details of these measures are as follows:

- *Dice Metric:* Let V_m and V_a be the automated and manually segmented volumes, respectively. The regions to be compared in this criteria are cavity and myocardium. *DM* is given by $DM = 2 \frac{V_a \cap V_m}{V_a + V_m}$. *DM* measures the similarity between the automatically detected and ground-truth regions. It is always in $[0 \ 1]$, 1 indicating a perfect match and 0 a total mismatch.
- *RMSE:* *RMSE* evaluates the similarity between automated and manual epi- and endo-

Methods	Dice Metric		$RMS E$ (unit:mm)		manual segmentation in testing procedure
	Cavity	Myocardium	Cavity	Myocardium	
CR (2D)	0.92 ± 0.07	0.80 ± 0.10	1.35 ± 0.13	2.05 ± 0.11	1 volume/subject
CR (3D)	0.80 ± 0.018	0.70 ± 0.01	1.95 ± 0.28	2.71 ± 0.13	N/A
GC(2D)	0.91 ± 0.04	0.81 ± 0.06	1.60	1.99	1 volume/subject
LS(2D)	0.88 ± 0.09	0.81 ± 0.10	0.89	1.89	1 volume/subject

Table 2.1: Statistical measures of the conformity between manually and automatically obtained contours for my method in 2D and 3D, Graph-cut (GC) method in [Ayed et al. \[2012\]](#), and level-set (LS) method in [Ayed et al. \[2009a\]](#). The dataset which was used for for GC and LS algorithms is the same as the dataset which was used for our algorithm.

cardium boundaries/surfaces. The $RMS E$ over N points is given by [Ayed et al. \[2012\]](#):

$$RMS E = \sqrt{\frac{1}{N} \sum_{i=1}^N (\hat{x}_i - \tilde{x}_i)^2 + (\hat{y}_i - \tilde{y}_i)^2} \quad (2.49)$$

where (\hat{x}_i, \hat{y}_i) is a point on the automatically detected boundary and $(\tilde{x}_i, \tilde{y}_i)$ is the corresponding point on the manually traced boundary. $RMS E$ evaluates a distance between manual and automatic contours. The lower the $RMS E$, the better the conformity of the results to the ground-truth.

Table 2.1 reports the DM (expressed as mean \pm standard deviation), and average $RMS E$ in millimeter for three algorithms: the proposed CR method, the graph cut method in [Ayed et al. \[2012, 2009b\]](#) (GC) and the level set method in [Ayed et al. \[2009a\]](#) (LS).

2D CR procedure resulted in improvements in accuracies over LS and GC, whereas 3D CR method yielded a decrease in accuracy. This effect can be attributed to the fact that the 3D CR approach requires much less user input than the 2D methods, and that the ground-truth segmentations are inherently two dimensional. I note, however, that all the methods yielded an average DM higher than 0.80 for cavity detection, indicating an excellent agreement

with manual segmentations [Pluempitiwiriyaewej et al. \[2005\]](#), and as observed by [Lynch et al. \[2008\]](#) a $DM > 0.90$ is generally difficult to obtain because the small structures within the cavity at the apex reduces DM significantly. I note also that the DM for the myocardium wall dropped by 10 percent compared to that for the cavity. This is reasonable since the DM is a declining function of the region's size. Because the myocardial wall area is much smaller than that of the cavity, a significant decrease in its DM is observed. Furthermore, the problem of myocardial segmentation is much more challenging due to the intensity similarity between the region and surrounding areas. For contour accuracy measured in terms of $RMS E$, all the methods led approximately to the same performance with an $RMS E$ of about < 1.95 mm for the endocardium and < 3 mm for the epicardium. This result favors the proposed 3D CR as it reduces significantly the user input compared to the recent methods listed in [Table. 2.1](#).

- *Correlation Coefficient(CC)*: The correlation coefficient evaluates the quality of a least squares fitting to the original data. The correlation coefficient between V_a and V_m for the regions within endo- and epicardium surfaces is estimated. CC is in $[0, 1]$, 1 indicating a perfect match and 0 a total mismatch. The proposed methods yielded a correlation coefficient equal to 0.95 for the cavity and 0.91 for the myocardium in the 2D case, whereas in the 3D case CC is 0.88 for the endocardium and 0.83 for the epicardium. These values indicate that the automatic and manual volume estimations are well correlated.
- *Linear regression plots*: In [Fig. 2.7](#), I plotted the computed and manual LV cavity and epicardium volumes for all 20 cardiac phases of 20 subjects, in both 2D and 3D cases. The linear regression lines are included to demonstrate the degree of similarity between automatic and manual segmentations. As the plots demonstrate, the highly automated 3D

Methods	CC	
	Endocardium	Epicardium
CR (2D)	0.95	0.91
CR (3D)	0.88	0.83

Table 2.2: Correlation coefficients between automatically and manually obtained segmentations.

algorithm overestimates endocardium volumes and underestimates epicardium volumes which stem from either inconsistency between 2D manual gold standard contours and the 3D contours from the proposed algorithm or lower accuracy around end systolic phases for blood pool and lower accuracy of the epicardium contour as it is a smaller ring-shape region with less information to learn from. Nevertheless, the result will not have a huge impact on EF as it is a relative measure between the end-diastolic and end-systolic phases.

Robustness of the algorithm with respect to initial surfaces/contours

In this section, the effect of the choice of the initial surfaces/contours is examined on the results of the proposed algorithm. Using a random subject, the algorithm is run starting from three different initializations, including a random cube whose size is approximately that of the entire image (Fig. 2.8 a). The yellow curves show the initial contours in the first line of the figure (a, b and c), and the final segmentations in the second line of the figure (d, e and f). The red curves depicts the ground-truth segmentations. Notice that the obtained results were approximately the same, although the initial contours were significantly different.

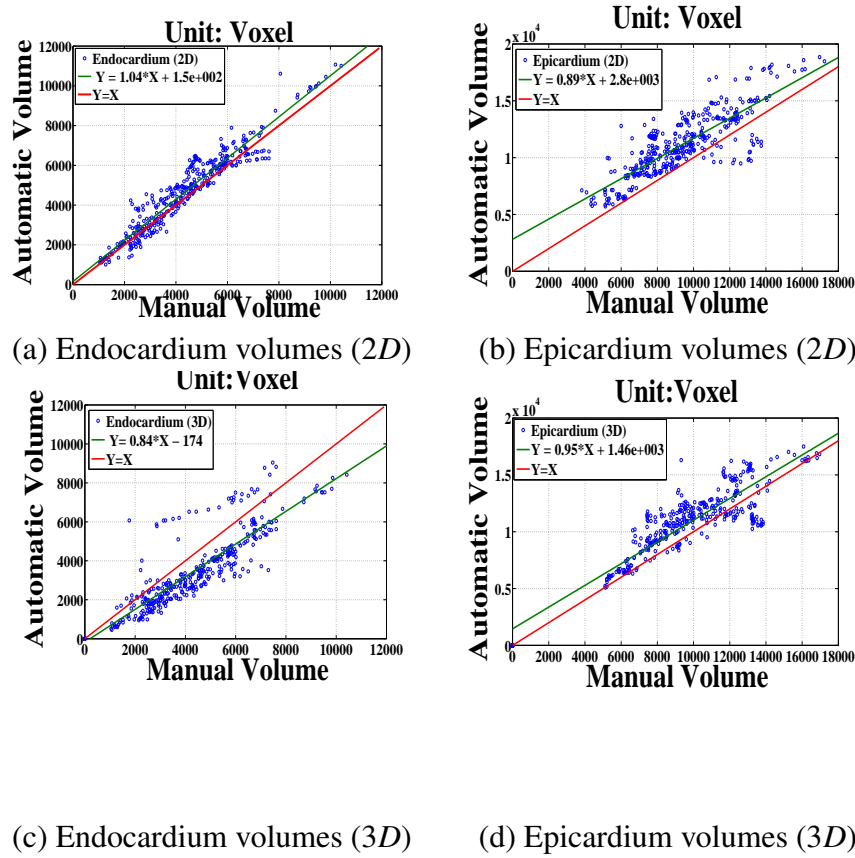


Figure 2.7: Linear regression plots depicting the automatic-segmentation volumes against manually obtained volumes in $2D$ (first row) and $3D$ (2nd row) for the entire dataset.

Robustness of the $3D$ convex-relaxation algorithm with respect to the choice of the training subject

In this section, a comprehensive evaluation of the robustness of the $3D$ convex-relaxation algorithm with respect to the choice of the training subject is reported. To this end, I proceeded to a leave-one-in approach consisting of 20 evaluations. Each evaluation corresponds to the choice of one training subject which is used to learn the model distributions. Then, given these models, the rest of the database (400 volumes, 20 subjects) is segmented, and the corresponding average DM , $RMSE$ and CC are measured. Table.2.3 listed the mean and standard deviation

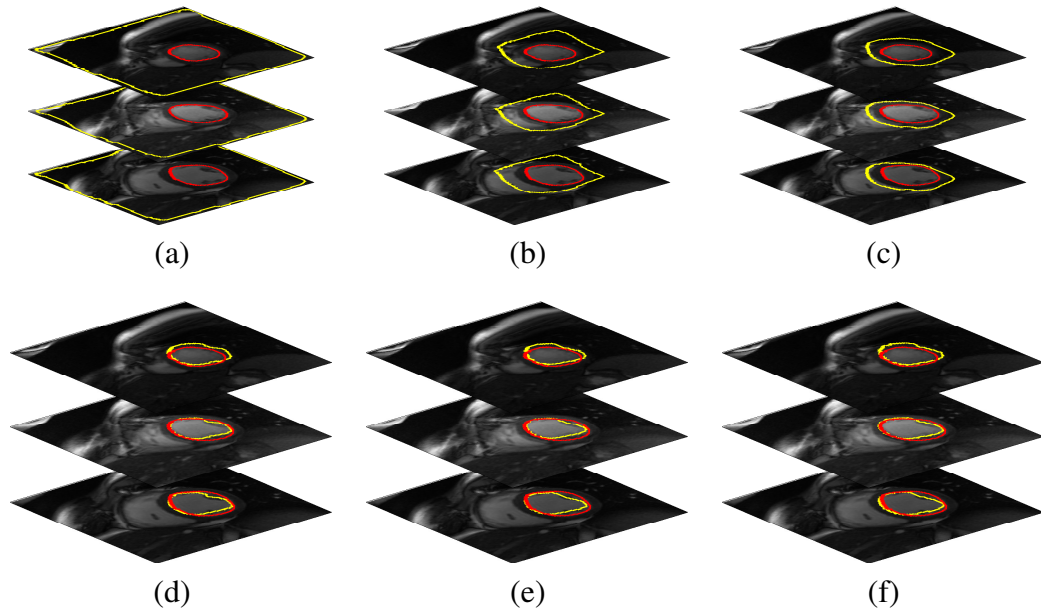


Figure 2.8: Effect of the choice of the initial surfaces/contours on the results. First line (a, b and c): The yellow curves depict three different initializations. Second line (d, e and f): The yellow curves depict the final segmentations. The red curves depict the ground-truth segmentation. The obtained results were approximately the same, although the initial contours were significantly different.

<i>DM</i>		RMSE		CC	
Cavity	Myocardium wall	Endocardium	Epicardium	Endocardium	Epicardium
0.79 ± 0.0051	0.70 ± 0.00006	1.93 ± 0.049	2.57 ± 0.0063	0.86 ± 0.0035	0.84 ± 0.0023

Table 2.3: The mean and standard deviation of obtained average *DM*, *RMS E* and *CC* for 20 different iterations using CR 3D method, where training subject is variable at each iteration; I used 20 different training subjects and validated the algorithm on the rest of the dataset.

of obtained average *DM*, *RMS E* and *CC* from 20 different iterations where variable parameter is the training subject (20 different training subjects). A very low standard deviation of average *DM*, *RMS E* and *CC* for both cavity and myocardium wall regions demonstrate that the performance of the 3D convex-relaxation algorithm is not affected by the choice of the training subject.

Invariance of the shape-prior models:

Using ground truth segmentations, in Fig.2.9 the distance distributions corresponding to 50 volumes obtained from 10 different subjects (5 volumes each) are plotted. The figures demonstrate that the distributions are very similar. The distance distributions have similar shapes, but slightly different supports. These slight shifts, which are due to inter-subject variations in scale of the cavity/myocardium regions, can be handled efficiently with the proposed fixed-point-equation computations.

To evaluate this invariance quantitatively, the Bhattacharyya coefficient is used. Recall that the range of the Bhattacharyya coefficient is $[0; 1]$, with 0 corresponding to no overlap between the distributions and 1 to a perfect match. The Bhattacharyya measures corresponding to all pairs of analyzed volumes (50 volumes) is computed. The average Bhattacharyya measures for all data analyzed is equal to 0.93 for the cavity and 0.88 for the myocardium. These values are close to 1, which shows the invariance of the distance distributions (up to a slight shift in distribution support). These results demonstrate that a single subject is sufficient for training, and confirm the relevance of the proposed shape priors to *LV* segmentation.

Robustness of the algorithm with respect to the choice of the weighting parameters

In this section, I report comprehensive experiments which evaluate quantitatively the robustness of the proposed 3D algorithm with respect to the choice of the weighting parameters.

Effect of the weights of the shape priors (α_c and α_m):

Figs. 2.10 (a-b) plot the average *DM* and *RMSE* over all subjects as functions of α_c

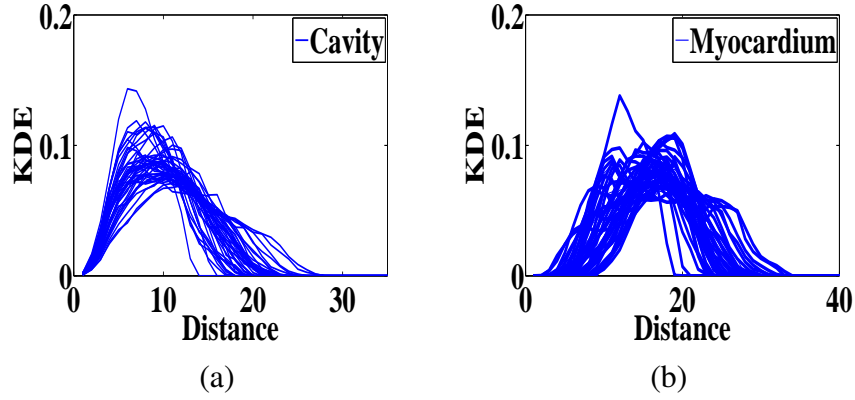


Figure 2.9: Distance distributions of 50 volumes obtained from 10 subjects (5 each) for (a) cavity and (b) myocardium regions; The average Bhattacharyya measures for all pairs of analyzed volumes (50 volumes) is 0.93 for cavity and 0.88 for myocardium. The distributions were estimated using 192 bins and a kernel width of 2.

(weight of the shape constraint for the cavity). The algorithm is run over several uniformly-spaced values of α_c in the interval $[0.1; 1]$. All the values of α_c within this interval yielded an average DM between 0.8 and 0.81. Therefore, parameter α_c does not require fine tuning. Similar experiments were performed to assess the effect of α_m (weight of the shape constraint for the myocardium), and plotted the corresponding graphs in Figs. 2.10 (c-d). A similar behavior is observed, and parameter α_m does not require fine tuning within the interval $[0.1; 1]$. Notice that, for both cavity and myocardium regions, the optimal value of the weight of the shape constraint correspond approximately to $\alpha_c = \alpha_m = 0.4$.

Effect of the smoothness weight (λ):

Figs. 2.11 (a-b) plots the average DM and $RMS E$ over all subjects as functions of λ . I executed the algorithm over several uniformly-spaced values of λ in the interval $[1; 25]$. Note that the λ did not require fine tuning: variations of λ in interval $[1; 25]$ did not affect significantly the algorithm performance. The best average performance was obtained for $\lambda = 1$.

Effect of the edge weight (β):

Figs. 2.11 (c-d) plots the average performance measures as functions of β . The algorithm is run over several uniformly-spaced values of β in the interval [10; 150]. Similarly to the other parameters, β did not need to be adjusted, with variations of the value of β in [10; 150] not affecting the average performance significantly.

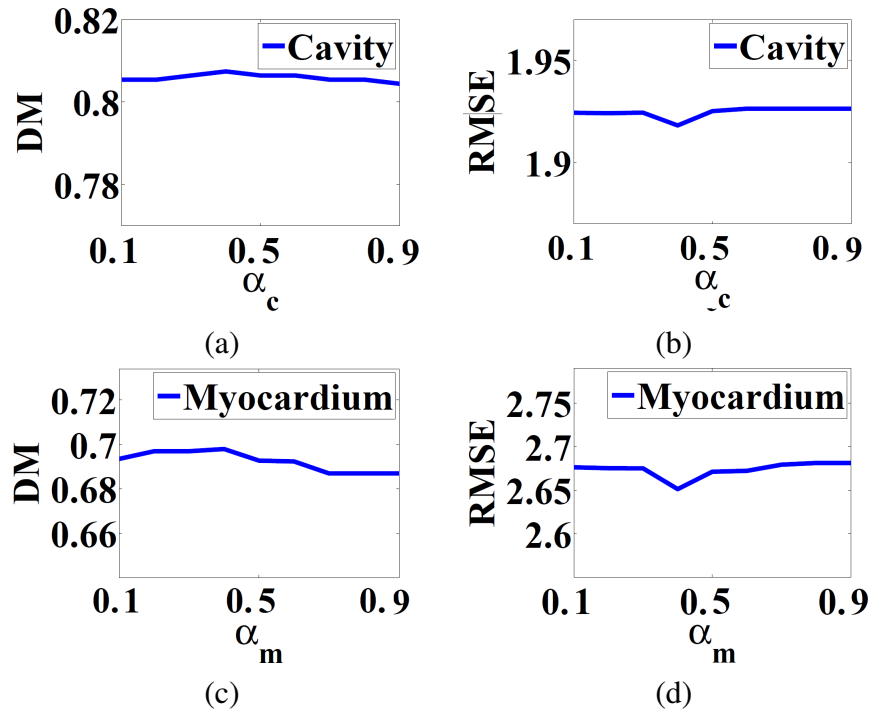


Figure 2.10: The average *DM* and *RMSE* over all the data-set as functions of the weights of the shape priors: (a-b) α_c ; (c-d) α_m .

2.4 Conclusion

This study investigated fast detection of the *LV* endo- and epicardial surfaces in cardiac magnetic resonance sequences. The solution was obtained with a convex-relaxation optimization of two original functionals, each containing two distribution-matching priors, one encoding intensity information and the other shape information. The shape prior is intrinsically invariant with respect to translation. A scale variable was introduced to achieve scale-invariance. The

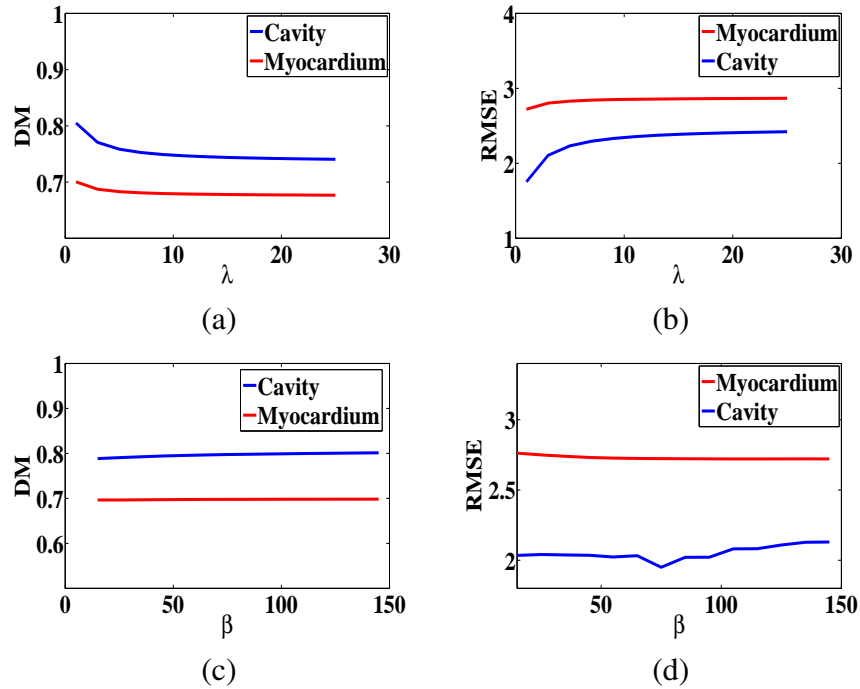


Figure 2.11: The average DM and $RMSE$ over all the data-set as functions of the smoothness/edge weights: (a-b) λ ; and (c-d) β .

proposed algorithm avoids the need for costly pose estimation (or registration) procedures and large training sets, and can tolerate shape deformations. Unlike related graph-cut approaches, the proposed solution can be parallelized to reduce substantially the computational time for 3D domains (or higher), extends directly to high dimensions, and does not have the grid-bias problem. The parallelized implementation on a *GPU* demonstrated that the proposed algorithm requires about 3.78 seconds for a typical cardiac *MRI* volume, a speed-up of about 5 times compared to a standard implementation. A performance evaluation was reported over 400 volumes acquired from 20 subjects that showed the obtained automatically delineated 3D surfaces correlate with independent manual contours. The results were assessed using DM , $RMSE$, and CC metrics as well. In all results, the myocardium wall's DM decreased by 10 percent compared to the DM for the cavity region. This can be attributed to two main reasons:

(1) The *DM* is a descending function of the region's size, and (2) The myocardial segmentation is way more challenging due to the intensity similarity between the region and the surrounding areas.

It was further demonstrated experimentally that the choice of the training subject does not affect the performance of the algorithm very much, and the utilized shape/geometric prior does not change significantly from one subject to another. It was shown that the algorithm performance is robust to the initial conditions. I further examined the effect of the parameters on the results via comprehensive experiments, thereby demonstrating that the algorithm does not require fine parameter tuning. Finally, it is worth mentioning that the 3D CR method yielded a decrease in accuracy compared to the 2D version. This effect can be explained by the fact that 3D formulation requires much less user input than the 2D method: For the 2D case, it requires the user to manually segment the first frame of the time sequence of each slice, i.e., it needs manual segmentations of 10 images among the 200 images in the testing subject data, whereas in the 3D case it needs only 1 point (mouse click) per target region (cavity or myocardium), i.e., two clicks for the whole 3D+time subject data. I can obtain more accurate 3D segmentations by simply combining the 2D segmentations, but at the expense of much more user effort. To reduce the user input significantly, the 3D formulation included new optimization steps/variables. In the 3D case, the degrees of freedom of the problem and its difficulty are higher, and the prior knowledge is less informative (a training subject different from the testing subject that was used). The 3D performance can be improved by adding further user inputs, for instance by using the same user delineations as in the 2D case.

Bibliography

- I. Ben Ayed, S. Li, and I. Ross. Embedding overlap priors in variational left ventricle tracking. *IEEE Transactions on Medical Imaging*, 28(12):1902–1913, 2009a.
- I. Ben Ayed, K. Punithakumar, S. Li, A. Islam, and J. Chong. Left ventricle segmentation via graph cut distribution matching. In *Medical Image Computing and Computer-Assisted Intervention (MICCAI)*, volume 1, pages 901–909, London, UK, 2009b.
- I. Ben Ayed, H.-M. Chen, K. Punithakumar, I. Ross, and S. Li. Graph cut segmentation with a global constraint: Recovering region distribution via a bound of the bhattacharyya measure. In *IEEE International Conference on Computer Vision and Pattern Recognition*, pages 1–7, San Francisco, CA, USA, 2010.
- I. Ben Ayed, H.-M. Chen, K. Punithakumar, I. Ross, and S. Li. Max-flow segmentation of the left ventricle by recovering subject-specific distributions via a bound of the bhattacharyya measure. *Medical Image Analysis*, 16:87–100, 2012.
- D. P. Bertsekas. *Nonlinear Programming*. Athena Scientific, 1999.
- A. Chambolle. An algorithm for total variation minimization and applications. *Journal of Mathematical Imaging and Vision*, 20(1-2):89–97, 2004.

- T. Chan and J.-H. Shen. *Image Processing And Analysis: Variational, PDE, Wavelet, and Stochastic Methods*. SIAM, Philadelphia, PA, USA, 2005.
- E. Giusti. *Minimal surfaces and functions of bounded variation*. Australian National University, Canberra, 1977.
- M. Lynch, O. Ghita, and P. F. Whelan. Segmentation of the left ventricle of the heart in 3-D+T MRI data using an optimized nonrigid temporal model. *IEEE Transactions on Medical Imaging*, 27(2):195–203, Feb 2008.
- M. Nikolova, S. Esedoglu, and T. F. Chan. Algorithms for finding global minimizers of image segmentation and denoising models. *SIAM Journal of Applied Mathematics*, 66(5):1632–1648, 2006.
- V.-Q. Pham, K. Takahashi, and T. Naemura. Foreground-background segmentation using iterated distribution matching. In *IEEE International Conference on Computer Vision and Pattern Recognition(CVPR)*, 2011.
- C. Pluempitiwiriyaewej, J. M. F. Moura, Y.-J. L. Wu, and C. Ho. STACS: new active contour scheme for cardiac MR image segmentation. *IEEE Transactions on Medical Imaging*, 24(5):593–603, 2005.
- R. T. Rockafellar and R. J.-B. Wets. *Variational analysis*, volume 317 of *Fundamental Principles of Mathematical Sciences*. Springer-Verlag, Berlin, 1998.
- J. Yuan, E. Bae, and X.-C. Tai. A study on continuous max-flow and min-cut approaches. In *IEEE International Conference on Computer Vision and Pattern Recognition (CVPR)*, 2010.

Chapter 3

Right Ventricle Segmentation using Invariant Object-Interaction Priors

This chapter¹ investigates a rapid segmentation of RV in short-axis cardiac MRI via convex relaxation (3D) using distribution matching. The algorithm requires only a single volume of a given subject from which to train or learn the models, and a very simple user input such

1

This chapter is based on the papers below:

1. Cyrus M.S. Nambakhsh, Terry M. Peters, A. Islam, Ismail Ben Ayed, **Right Ventricle Segmentation with Probability Product Kernel Constraints**, In: Medical Image Computing and Computer-Assisted Intervention (MICCAI), 2013.
2. Cyrus M.S. Nambakhsh, M. Rajchl, T.M. Peters, I. Ben Ayed, **Rapid Automated 3D RV Endocardium Segmentation in MRI via Convex Relaxation and Distribution Matching**, In: Medical Image Computing and Computer-Assisted Intervention (MICCAI) 2012 RV Challenge.
3. C. Petitjean, Cyrus M.S. Nambakhsh, T.M. Peters, I. Ben Ayed, et al., **Right Ventricle Segmentation From Cardiac MRI: A Collation Study**, To be submitted to IEEE Transaction of Medical Imaging (TMI), 2013.
4. Cyrus M.S. Nambakhsh, I. Ben Ayed, A. Islam, G. Garvin, T.M. Peters, S. Li, **Graph cuts with invariant inter-segment priors**, to be Submitted to IEEE Transaction of Medical Imaging (TMI), 2013.

as planting a seed at about centroid of the LV cavity. The solution is sought following the optimization of a functional containing shape, spatial orientation of the RV with respect to the LV, as well as the intensity priors. Based on a global measure of similarity between the distributions, the shape prior is intrinsically invariant with respect to translation. To achieve scale-invariance, a scale variable is added to the optimization from which a fixed-point equation (FPE) is derived. The 3D convex relaxation approach can be parallelized, and is implemented on a GPU. The results demonstrate that the proposed algorithm requires about 5 seconds to segment a typical cardiac MRI volume. I report a performance evaluation over 64 volumes acquired from 32-subject dataset provided by the RV Challenge at MICCAI'12 and 400 volumes from another dataset (20 subjects) of cine MRI. The results show that the obtained 3D surfaces correlate with independent manual delineations. It is further demonstrated experimentally that the performance of the algorithm is not significantly affected by the choice of the training subject, and the shape description which is proposed does not change significantly from one subject to another. These results support the fact that a single subject is sufficient for training the proposed algorithm.

3.1 Formulation

3.1.1 The functional

Let $I : \Omega \subset \mathbb{R}^3 \rightarrow \mathcal{Z}_I \subset \mathbb{R}$ be an image function that maps 3D domain Ω to a finite set of intensity values \mathcal{Z}_I . Let $D : \Omega \rightarrow \mathcal{Z}_D \subset \mathbb{R}$ be a distance function which measures the distance between each point $\mathbf{x} = (x, y, z) \in \Omega$ and a given anatomical landmark (i.e., a point) $O \in \Omega$, which will be used to build a translation-invariant shape prior and to learn an intensity prior (in this work, the centroid of the LV cavity is used region as landmark):

- The distance-distribution prior:

Assume distance (D) is $D(\mathbf{x}) = \|\mathbf{x} - \mathcal{O}\|$, with $\|\cdot\|$ the standard L2 norm. \mathcal{Z}_D is a finite set of distance values. \mathcal{O} is obtained from a very simple user input that amounts to the manual identification of the centroid of the LV cavity within a middle slice with a single mouse click.

- The angle-distribution prior:

Let $A : \Omega \rightarrow \mathcal{Z}_A \subset \mathbb{R}$ be a function measuring the angle between the vector pointing from each point $\mathbf{x} \in \Omega$ to \mathcal{O} and the fixed x-axis unit vector u :

$$A(\mathbf{x}) = \frac{\langle \vec{x}_O, u \rangle}{\|\vec{x}_O\| \|u\|}.$$

The objective is to find the optimal RV segment by solving the following optimization problem:

$$\begin{aligned} \hat{u} &= \arg \min_{u \in \{0,1\}} \mathcal{E}(u) \text{ with} \\ \mathcal{E}(u) &:= \underbrace{-\langle \mathbf{P}^I(u, \cdot), \mathbf{M}^I \rangle_\rho}_{\text{Intensity Prior}} - \underbrace{\alpha_D \langle \mathbf{P}^D(u, \cdot), \mathbf{M}^D \rangle_\rho}_{\text{Distance prior}} - \underbrace{\alpha_A \langle \mathbf{P}^A(u, \cdot), \mathbf{M}^A \rangle_\rho}_{\text{Angle prior}} \\ &\quad \underbrace{\hspace{10em}}_{\text{Shape prior}} \\ &\quad + \underbrace{\gamma \int_{\Omega} C |\nabla u| \, d\mathbf{x}}_{\text{Smoothness/Edges}} \end{aligned} \tag{3.1}$$

Detailed description of the notations and variables that appear in the optimization problem in equation (3.1) is given below:

- $u : \Omega \rightarrow \{0, 1\}$ is a binary function, which defines a variable partition of Ω : $\{\mathbf{x} \in \Omega / u(\mathbf{x}) = 1\}$, corresponding to the target RV segment, and $\{\mathbf{x} \in \Omega / u(\mathbf{x}) = 0\}$, corresponding to the complement of the target segment in Ω .

- For image data $J \in \{I, D, A\} : \Omega \subset \mathbb{R}^3 \rightarrow \mathcal{Z}_J$, and for any binary function $u : \Omega \rightarrow \{0, 1\}$, $\mathbf{P}^J(u, \cdot)$ is a vector encoding the probability density function (pdf) of data J within the segment defined by $\{\mathbf{x} \in \Omega / u(\mathbf{x}) = 1\}$:

$$\mathbf{P}^J(u, z) = \frac{\int_{\Omega} \mathcal{K}_z(J)u \, d\mathbf{x}}{\int_{\Omega} u \, d\mathbf{x}} \quad \forall z \in \mathcal{Z} \quad (3.2)$$

with \mathcal{K}_z a Gaussian window: $\mathcal{K}_z(y) = \frac{1}{(2\pi\sigma^2)^{(1/2)}} \exp\left(-\frac{\|z-y\|^2}{2\sigma^2}\right)$, with σ the width of the window.

- $\langle f, g \rangle_{\rho}$ is the *probability product kernel* [Jebara et al. \[2004\]](#), which evaluates the affinity between two pdfs f and g . It generalizes the similarity measure from Bhattacharyya to probability product kernels:

$$\langle f, g \rangle_{\rho} = \sum_{z \in \mathcal{Z}} [f(z)g(z)]^{\rho} \quad \rho \in]0, 1], \mathcal{Z} \in \{\mathcal{Z}_I, \mathcal{Z}_D, \mathcal{Z}_A\} \quad (3.3)$$

The higher $\langle f, g \rangle_{\rho}$, the better the affinity between pdfs f and g . Minimization of the probability product kernels in (3.1) aims to find a target segment whose shape and intensity pdfs most closely match *a priori* learned models:

- \mathbf{M}^I is a model of intensity.

Given the fact that the left and right ventricles have similar intensity profiles (as they both contain blood), \mathbf{M}^I is learnt from intensity data within a cylinder centered at O . The radius of the cylinder, d , is a free parameter which has to be fixed experimentally.

– \mathbf{M}^D and \mathbf{M}^A are models of distances and angles which are intrinsically invariant with respect to translation and describe the RV shape. These models are learnt from the data within the user-delineated RV cavity region from a single training subject different from the testing subject.

- $C : \Omega \rightarrow \mathbb{R}$ is an edge-indicator function given by:

$$C(\mathbf{x}) = \frac{1}{1+\nabla I(\mathbf{x})}$$

- γ , α_D and α_A are positive constants that balance the contribution of each constraint in (3.1).

Fig. 3.1(b) illustrates the LV centroid, angle and distance priors (\mathbf{M}^D and \mathbf{M}^A) and Fig. 3.1(a) demonstrates that a simple intensity thresholding of the image leaves the RV cavity connected to all surrounding regions with the same intensity profile.

As shown in Fig. 3.1 (a), the intensity prior alone is not sufficient to segment the RV region. There are several regions connected to the RV which their intensity profiles are very similar to the intensity profile of the RV region (the region enclosed within the red curve in Fig. 3.1 (a)). The consistency of all three priors over the 2D frames within a single MRI sequence of one subject is demonstrated in Fig. 3.2, which depicts the angle, distance and intensity distributions (upper to bottom row) corresponding to the manually segmented RV cavities from end-diastolic to end-systolic phases (20 frames), for both apical, mid-cavity and basal slices. One can observe that these distributions do not vary significantly throughout a cardiac cycle.

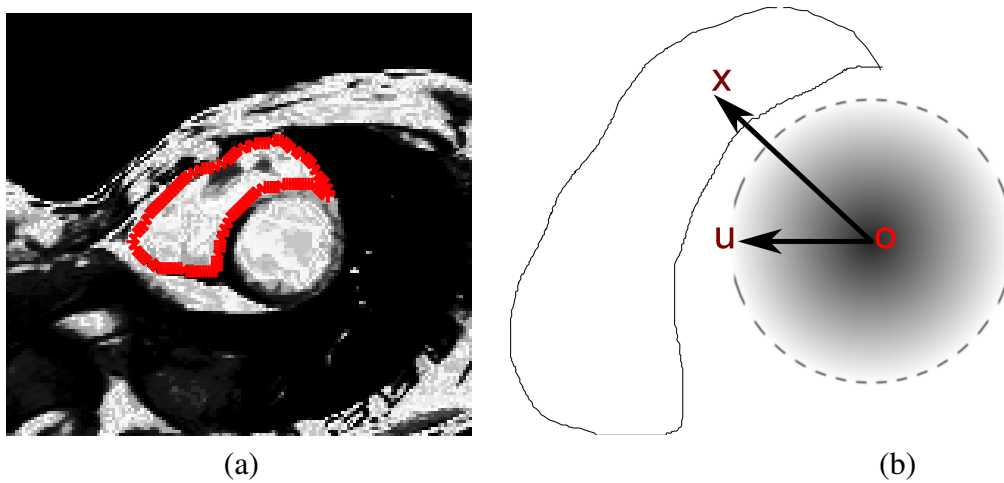


Figure 3.1: (a) An example of regions connected to the RV in which their intensity profiles are very similar to that of the RV region (the region enclosed within the red curve); (b) The geometric relationships between the LV centroid and the RV region for building the object-interaction priors.

Automation with a scale variable:

The shape priors in (3.1) are not invariant with respect to scale (or size) of the RV segments for different subjects. To illustrate this, I plotted in Fig. 3.3 (c) the distance pdfs corresponding to the ground-truth segmentations of 20 different subjects (two different volumes for each subject). The figure demonstrates that the distance pdfs have similar Gaussian shapes, but shifted

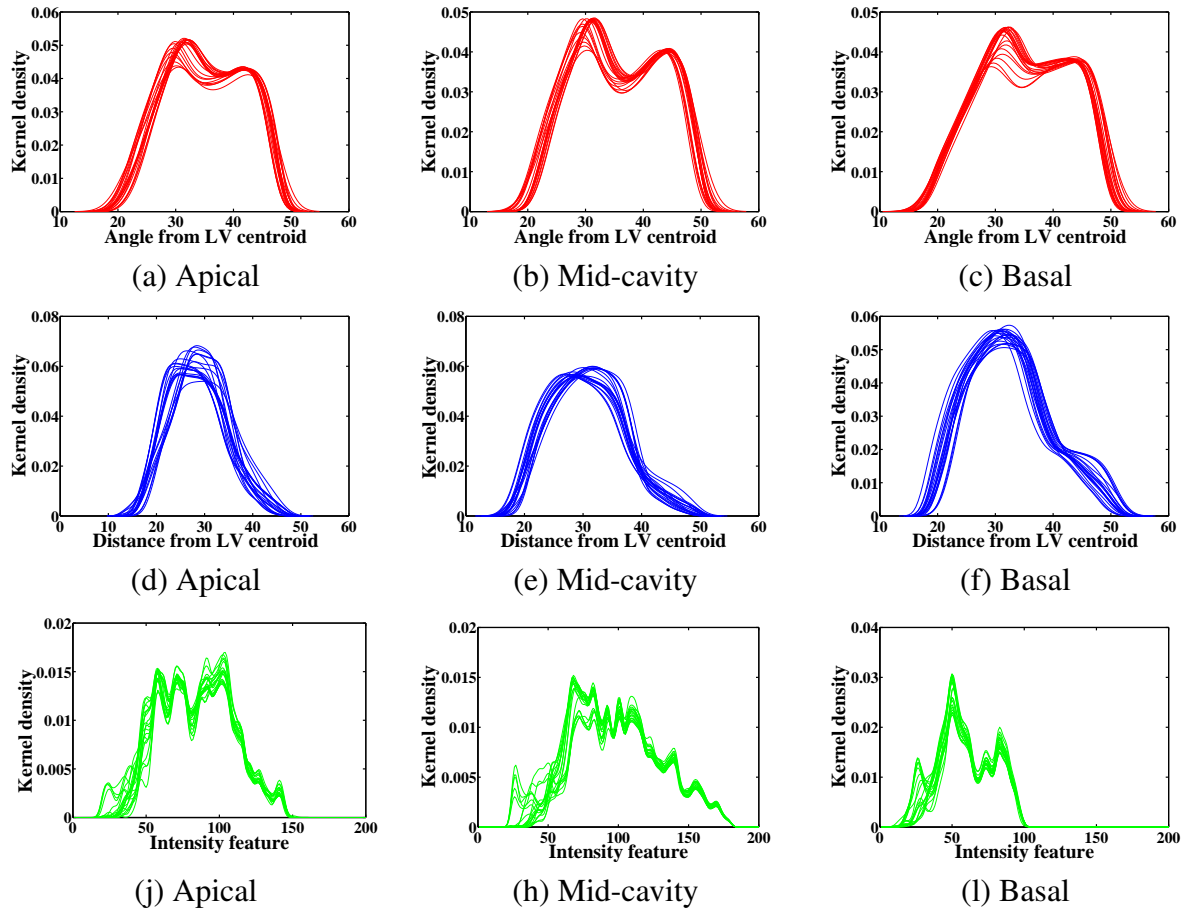


Figure 3.2: Plots of the angle, distance from LV centroid and intensity distributions of the pixels within the RV cavities for 20 frames of one single sequence of a single subject (the manual segmentations are used to compute these distributions). 1st row: angles; 2nd row: distances from LV centroid; 3rd row: intensities. 1st column: apical slices; 2nd column: mid-cavity slices; 3rd column: basal slices.

supports.

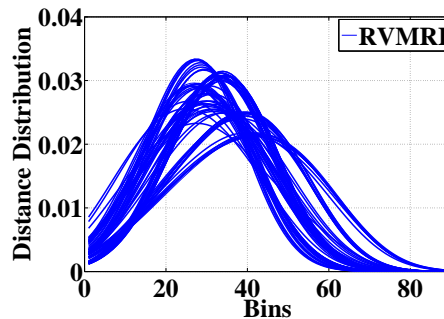


Figure 3.3: Invariance and shift of the distance-based shape model.

This shift is due to inter-subject variations in scale (or size). To account for such shifts,

a scale variable is further introduced in the model of distances: $\mathbf{M}^D(., s) : \mathcal{Z}_D \times \mathbb{R} \rightarrow [0, 1] / \mathbf{M}^D(z, s) = \mathbf{M}^D(z + s), s \in \mathbb{R}$. Thus, to account for this new variable (s), the distance-based prior in (3.1) is replaced by a scale-dependent prior: $\langle \mathbf{P}^D(u, .), \mathbf{M}^D \rangle_\rho \rightarrow \langle \mathbf{P}^D(u, .), \mathbf{M}^D(., s) \rangle_\rho$. Therefore, s becomes a variable which has to be optimized along with the segmentation region. With this new variable, the problem becomes: $\{\hat{u}, \hat{s}\} = \min_{u, s} \mathcal{E}(u, s)$.

3.1.2 Two-step optimization

The model has two different types of variable, the target segment described by indicator function u and the scale variable s . Therefore, an iterative two-step procedure is adopted. First, the scale variable is fixed and the proposed functional is optimized with respect to u via convex relaxed. Then, the optimization is run over the scale variable via fixed-point computations, while u is fixed.

Step 1–Optimization with respect to the segment via convex-relaxed

To simplify further development, let us assume that the functional contains only one probability product kernel and has the following general form:

$$\min_{u(x) \in \{0,1\}} \left\{ \mathcal{E}(u) := -\langle \mathbf{P}(u, .), \mathbf{M} \rangle_\rho + \int_{\Omega} C |\nabla u| d\mathbf{x} \right\} \quad (3.4)$$

The superscripts are omitted. Once the problem in (3.4) is solved, extension to a weighted sum of probability product kernels, as is the case in (3.1), becomes straightforward. Unfortunately, the probability product kernel in (3.4) is a non-linear (high-order) functional, which results in a difficult (non-convex) optimization problem that is not directly amenable to stan-

dard solvers. The problem is split into several surrogate-functional optimizations, each solved via a convex relaxation and an efficient multiplier-based augmented Lagrange method.

functionals: I proceed by constructing and optimizing iteratively surrogate functionals of \mathcal{E} (which its optimization is easier than the original functional):

Definition 1. Given a fixed labeling u^i (i is the iteration number), $\mathcal{S}(u, u^i)$ is a surrogate functional of \mathcal{E} if it satisfies the following conditions [Zhihua et al. \[2007\]](#):

$$\mathcal{E}(u) \leq \mathcal{S}(u, u^i) \quad (3.5a)$$

$$\mathcal{E}(u) = \mathcal{S}(u, u) \quad (3.5b)$$

Rather than optimizing \mathcal{E} directly, the surrogate functional is optimized over the first variable at each iteration:

$$u^{i+1} = \min_u \mathcal{S}(u, u^i), \quad i = 1, 2, \dots \quad (3.6)$$

Using the constraints in (3.5a) and (3.5b), and by definition of minimum in (3.6), one can show that the solutions in (3.6) yields a decreasing sequence of \mathcal{E} :

$$\mathcal{E}(u^i) = \mathcal{S}(u^i, u^i) \geq \mathcal{S}(u^{i+1}, u^i) \geq \mathcal{E}(u^{i+1}). \quad (3.7)$$

Therefore, if \mathcal{E} is lower bounded, sequence $\mathcal{E}(u^i)$ converges to a minimum of \mathcal{E} . Now, consider the following proposition:

Proposition 6. (3D Convex relaxation): Given a fixed $u^i : \Omega \rightarrow \{0, 1\}$, the following functional is a surrogate of functional \mathcal{E} defined in (3.4):

$$\mathcal{S}(u, u^i) = -\langle \mathbf{P}(u^i, \cdot), \mathbf{M} \rangle_\rho + \int_\Omega f^i u^- dx + \int_\Omega g^i u^+ dx + \int_\Omega C |\nabla u| dx \quad (3.8)$$

where

$$u^-(\mathbf{x}) := \begin{cases} 1 - u(\mathbf{x}), & \text{for } u^i(\mathbf{x}) = 1 \\ 0, & \text{otherwise} \end{cases}, u^+(\mathbf{x}) := \begin{cases} u(\mathbf{x}), & \text{for } u^i(\mathbf{x}) = 0 \\ 0, & \text{otherwise} \end{cases} \quad (3.9)$$

and

$$f^i = \sum_{z \in \mathcal{Z}} \frac{\mathcal{D}_{z,i,\rho} \mathcal{T}_{\mathbf{M},z}}{\int_\Omega \mathcal{T}_{\mathbf{M},z} u^i dx}; \mathcal{T}_{\mathbf{M},z} = \mathcal{K}_z(J) \mathbf{M}(z); \quad (3.10)$$

$$\mathcal{D}_{z,i,\rho} = \left[\frac{\int_\Omega \mathcal{T}_{\mathbf{M},z} u^i dx}{\int_\Omega u^i dx} \right]^\rho; g^i = \sum_{z \in \mathcal{Z}} \frac{\mathcal{D}_{z,i,\rho}}{\rho \int_\Omega u^i dx} \quad (3.11)$$

Proof. To prove $\mathcal{E}(u) \leq \mathcal{S}(u, u^i)$, let us first define the following expressions:

$$v^+ = \frac{\int_\Omega \mathcal{T}_{\mathbf{M},z} u^+ dx}{\int_\Omega \mathbf{T}_{\mathbf{M},z} u^i dx}; v^- = \frac{\int_\Omega \mathcal{T}_{\mathbf{M},z} u^- dx}{\int_\Omega \mathbf{T}_{\mathbf{M},z}(x) u^i dx}; w^+ = \frac{\int_\Omega u^+ dx}{\int_\Omega u^i dx}; w^- = \frac{\int_\Omega u^- dx}{\int_\Omega u^i dx} \quad (3.12)$$

lows:

Using these expressions, the probability product kernel in (3.4) can be re-written as fol-

$$\langle \mathbf{P}(u, \cdot), \mathbf{M} \rangle_\rho = \sum_{z \in \mathcal{Z}} \left\{ \left[\frac{\int_{\Omega} \mathcal{T}_{\mathbf{M}, z} u^i d\mathbf{x}}{\int_{\Omega} u^i d\mathbf{x}} \right]^\rho \left[\frac{1 + v^+ - v^-}{1 + w^+ - w^-} \right]^\rho \right\} \quad (3.13)$$

Observe all the variables v^+ , v^- , w^+ and w^- are positive, then:

$$\left[\frac{1 + v^+ - v^-}{1 + w^+ - w^-} \right]^\rho \geq \left[\frac{1 - v^-}{1 + w^+} \right]^\rho \geq (1 - v^-)(1 - \rho w^+) \geq (1 - v^- - \rho w^+) \quad (3.14)$$

The above inequalities are due the fact that for any $v^- \in [0, 1]$ and $w^+ \in [0, 1]$, and for $\rho \in]0, 1]$, we have $(1 - v^-)^\rho \geq (1 - v^-)$ and $1/(1 + w^+)^\rho \geq 1 - \rho w^+$. Substituting (3.14) into (3.13), and after some manipulations, $\mathcal{E}(u) \leq \mathcal{S}(u, u^i)$ is obtained. The proof that $\mathcal{E}(u) = \mathcal{S}(u, u)$ is straightforward, and it suffices to observe that, when $u^i = u$, the second and third integral in (3.8) become equal to zero, proving the proposition 6. \square

Convex relaxation and equivalent constrained problem: Now, $\mathcal{S}(u, u^i)$ is minimized over $u \in \{0, 1\}$ via convex optimization. Let Ω_g and Ω_f be two disjoint domains given by the current indicator function $u^i \in \{0, 1\}$: $\Omega_g = \{\mathbf{x} \in \Omega / u^i(\mathbf{x}) = 1\}$ and $\Omega_f = \{\mathbf{x} \in \Omega / u^i(\mathbf{x}) = 0\}$. From the definitions of u^+ and u^- , $\min_{u \in \{0, 1\}} \mathcal{S}(u, u^i)$ is reformulated by (the first term in the expression of $\mathcal{S}(u, u^i)$ is omitted because it is a constant independent of u):

$$\begin{aligned} \min_{u \in \{0, 1\}} \mathcal{S}(u, u^i) &= \min_{u \in \{0, 1\}} J^i(u) \text{ where} \\ J^i(u) &:= \int_{\Omega_f} f^i(1 - u) d\mathbf{x} + \int_{\Omega_g} g^i u d\mathbf{x} + \int_{\Omega} C |\nabla u| d\mathbf{x} \end{aligned} \quad (3.15)$$

Model (3.15) is non-convex due to the binary constraint $u \in \{0, 1\}$. Such a binary constraint

is relaxed to the continuous interval $[0, 1]$, and replace (3.15) by the following convex optimization problem: $\min_{u \in [0,1]} J^i(u)$. Similar convex relaxations have been recently shown to be effective in solving the classical piecewise-constant segmentation model Yuan et al. [2010]. To efficiently solve $\min_{u \in [0,1]} J^i(u)$ via convex optimization Bertsekas [1999], let us first consider the following proposition:

Proposition 7. $\min_{u \in [0,1]} J^i(u)$ is equivalent to the following constrained problem:

$$\begin{aligned} \max_{p_g, p_f, p} \min_{u \in [0,1]} & \int_{\Omega_f} p_g d\mathbf{x} + \int_{\Omega_f} (\operatorname{div} p - p_g)u d\mathbf{x} + \int_{\Omega_g} (\operatorname{div} p + p_f)u d\mathbf{x} \quad s.t. \\ & p_g(\mathbf{x}) \leq f^i(\mathbf{x}) \forall \mathbf{x} \in \Omega_f; p_f(\mathbf{x}) \leq g^i(\mathbf{x}) \forall \mathbf{x} \in \Omega_g; |p(\mathbf{x})| \leq C(\mathbf{x}) \forall \mathbf{x} \in \Omega \end{aligned} \quad (3.16)$$

where $p : \Omega \rightarrow \mathbb{R}$, $p_g : \Omega \rightarrow \mathbb{R}$ and $p_f : \Omega \rightarrow \mathbb{R}$ are variables in the form of scalar functions defined over the image domain. In (3.16), u is viewed as the multiplier to equality constraints $-p_g(\mathbf{x}) + \operatorname{div} p(\mathbf{x}) = 0 \forall \mathbf{x} \in \Omega_f$ and $p_f(\mathbf{x}) + \operatorname{div} p(\mathbf{x}) = 0 \forall \mathbf{x} \in \Omega_g$. Furthermore, by simply thresholding the optimum $u^* \in [0, 1]$ of (3.16), an exact and global optimum of the non-convex problem $\min_{u \in [0,1]} J^i(u)$ is obtained.

Proof. For the constrained optimization problem in (3.16), the conditions of the min max theorem (Ekeland and Témam [1999], Chapter 6, Proposition 2.4) are all verified: the constraints are convex, and the functional is linear in both p_g, p_f, p and multiplier u . Therefore, the functional is convex l.s.c. for fixed u and concave u.s.c. for fixed p_g, p_f and p . It follows that the

min/max operators in (3.16) can be interchanged, which yields after some manipulations:

$$\begin{aligned} \min_{u \in [0,1]} \max_{p_g, p_f, p} \int_{\Omega_f} (1-u) p_g d\mathbf{x} + \int_{\Omega_g} u p_f d\mathbf{x} + \int_{\Omega} u \operatorname{div} p d\mathbf{x} \quad s.t. \\ p_g(\mathbf{x}) \leq f^i(\mathbf{x}) \forall \mathbf{x} \in \Omega_f; p_f(\mathbf{x}) \leq g^i(\mathbf{x}) \forall \mathbf{x} \in \Omega_g; |p(\mathbf{x})| \leq C(\mathbf{x}) \forall \mathbf{x} \in \Omega \end{aligned} \quad (3.17)$$

Now, notice that $\max_{w \leq C} vw = vC$, where v , w and C are positive scalars. This results:

$$\begin{aligned} \max_{p_g \leq f^i} \int_{\Omega_f} (1-u) p_g d\mathbf{x} &= \int_{\Omega_f} (1-u) f^i d\mathbf{x} \text{ and } 1-u \geq 0 \text{ i.e., } u \leq 1 \\ \max_{p_f \leq g^i} \int_{\Omega_g} u p_f d\mathbf{x} &= \int_{\Omega_g} u g^i d\mathbf{x} \text{ and } u \geq 0 \end{aligned} \quad (3.18)$$

It is also well-known that [Yuan et al. \[2010\]](#)

$$\max_{|p(\mathbf{x})| \leq C(\mathbf{x})} \int_{\Omega} u \operatorname{div} p d\mathbf{x} = \int_{\Omega} C |\nabla u| d\mathbf{x} \quad (3.19)$$

Finally, substituting (3.18) and (3.19) into (3.17) proves proposition 7. The fact that a thresholding of the solution yields a global optimum of the initial non-convex problem follows directly from the thresholding theorem [Nikolova et al. \[2006\]](#). \square

Proposition 7 allows us to derive an efficient multiplier-based algorithm (based on the augmented Lagrangian method [Bertsekas \[1999\]](#)) for optimizing $\mathcal{S}(u, u^i)$ with respect to u . We define the following augmented Lagrangian function

$$(c > 0) : L_c(p_g, p_f, p, u) = \int_{\Omega_f} p_g d\mathbf{x} + \int_{\Omega_f} (\operatorname{div} p - p_g) u d\mathbf{x} + \int_{\Omega_g} (\operatorname{div} p + p_f) u d\mathbf{x} -$$

$$\frac{c}{2} \|\operatorname{div} p - p_g\|_{\Omega_f}^2 - \frac{c}{2} \|\operatorname{div} p + p_f\|_{\Omega_g}^2. \quad (3.20)$$

A summary of the algorithm is given below in Algorithm 2 (to avoid confusion with i , which is the outer iteration number, j is used as inner iteration number. The inner iterations in Algorithm 2 are repeated until convergence).

Algorithm 2 Augmented-Lagrangian optimization

- $j = 1$: Initialize flows p_g^1, p_f^1, p^1 and labeling $u^1 \in \{0, 1\}$. Then start $j + 1$ -th iteration;
- Fix p^j and u and maximize in a closed form $L_c(p_g, p_f, p, u)$ over p_g and p_f :

$$(p_g^{j+1}, p_f^{j+1}) := \arg \max_{p_g, p_f} L_c(p_g, p_f, p^j, u);$$

- Fix p_g^{j+1}, p_f^{j+1} and u and maximize iteratively $L_c(p_g, p_f, p, u)$ over p (This can be solved by the Chambolle's projection algorithm [Chambolle \[2004\]](#)):

$$p^{j+1} := \arg \max_p L_c(p_g^{j+1}, p_f^{j+1}, p, u);$$

- Update labeling function u by

$$u(\mathbf{x}) = \begin{cases} u(\mathbf{x}) + c (\operatorname{div} p^{j+1}(\mathbf{x}) - p_g^{j+1}(\mathbf{x})), & \forall \mathbf{x} \in \Omega_f \\ u(\mathbf{x}) + c (\operatorname{div} p^{j+1}(\mathbf{x}) + p_f^{j+1}(\mathbf{x})), & \forall \mathbf{x} \in \Omega_g \end{cases}.$$

Step 2–Fixed-point optimization with respect to the scale variable

Labeling variable u is fixed and \mathcal{E} is optimized with respect to s . Considering a variable change $z \leftarrow z - s$ and the fact that only the distance-distribution prior depends on s , we have:

$$\begin{aligned} \frac{\partial \mathcal{E}}{\partial s} &= -\alpha_D \frac{\partial \langle \mathbf{P}^D(u, \cdot), \mathbf{M}^D(\cdot, s) \rangle_\rho}{\partial s} \\ &= -\rho \alpha_D \sum_{z \in \mathcal{Z}_D} \frac{\partial \mathbf{P}^D(u, z - s)}{\partial s} [\mathbf{M}^D(z)]^\rho [\mathbf{P}^D(u, z - s)]^{\rho-1} \end{aligned} \quad (3.21)$$

Using the pdf expression in (3.2), then:

$$\frac{\partial \mathbf{P}^D(u, z - s)}{\partial s} = \frac{\int_{\Omega} \frac{\partial \mathcal{K}_z(s+D)}{\partial s} u d\mathbf{x}}{\int_{\Omega} u d\mathbf{x}} = \frac{\int_{\Omega} (z - s - D) \mathcal{K}_z(s + D) d\mathbf{x}}{\sigma^2 \int_{\Omega} u d\mathbf{x}} \quad (3.22)$$

Embedding (3.22) in (3.21), setting the obtained expression to zero, and after some manipulations, the following necessary condition is obtained for a minimum of \mathcal{E} with respect to s :

$s - g(s) = 0$ where

$$g(s) = \frac{\sum_{z \in \mathcal{Z}_D} \int_{\Omega} (z - D) \mathcal{K}_z(D + s) [\mathbf{M}^D(z)]^{\rho} [\mathbf{P}^D(u, z - s)]^{\rho-1} u d\mathbf{x}}{\sum_{z \in \mathcal{Z}_D} \int_{\Omega} \mathcal{K}_z(D + s) [\mathbf{M}^D(z)]^{\rho} [\mathbf{P}^D(u, z - s)]^{\rho-1} u d\mathbf{x}} \quad (3.23)$$

Note that since the necessary condition in (3.23) has the form of a fixed-point equation, the solution can be obtained by fixed-point iterations:

$$s^{n+1} = g(s^n), \quad n = 1, 2, \dots \quad (3.24)$$

Let s^{opt} be the limit of sequence s^n at convergence, which is obtained as follows,

$$s^{opt} = \lim_{n \rightarrow +\infty} s^{n+1} = \lim_{n \rightarrow +\infty} g(s^n) = g(\lim_{n \rightarrow +\infty} s^n) = g(s^{opt}). \quad (3.25)$$

Consequently, s_{opt} is a solution of the necessary condition obtained in (3.23).

3.2 Experiments

In the following, a typical example, which illustrates explicitly the effect of the proposed novel object-interaction priors and the effect of fixed-point equation on minimizing the user interaction is described. Then, the parameters which were used in the 3D automatic segmentations are detailed, and some representative samples of the results are illustrated.

Datasets

In this chapter, the algorithm is evaluated using two data-sets,

1. An in-house dataset to which is referred as MRIUWO from this point onward. The MR images were acquired from 16 subjects, each comprising 120 short-axis 1.5T FIESTA MRI images. Each subject includes 20 volumes where each volume includes two apical, three mid-cavity, and two basal slices. Each slice contains a sequence of 20 frames. For each frame the pixel spacing is 1.17 – 1.56 mm, and the slice thickness is 8 – 10 mm where the image resolution is 256 × 256 pixels. The images were acquired from subjects of 16-69 years of age,
2. The Training, Test1 and Test2 datasets (16 subjects in each) provided by the RV Challenge, MICCAI'12 which is referred as MICCAI'12 from this point onward. The MR images were acquired using 1.5T machine (Siemens Medical Systems). Retrospectively synchronized balanced steady-state free precession sequences were performed for the cine analysis, with repeated 10-15 second breath-holds. 2-, 3- and 4-chamber images were acquired and 8-12 contiguous cine short axis slices were obtained from the basal to apex. Table. 3.1 lists the details of the sequence parameters. MR images were

TR	TE	Slice thickness	Matrix size	Field of view	spatial resolution
50 ms	1.7 ms	7 mm	256×216	360-420 mm	0.75 mm/pixel

Table 3.1: The details of MR sequence and images in MICCAI'12 dataset .

zoomed and cropped to a 256×216 pixel ROI. Only 48 MRI datasets were retained for this challenge study. There are 2 images in each cycle.

Three types of evaluation are performed:

- Standard quantitative evaluation, which compares the results with independent manual segmentations approved by an expert;
- Computational evaluation, which demonstrates that the parallelized computations run on a GPU (NVIDIA Tesla C1600) can bring a significant speed-up of more than 20 times for a typical cardiac MRI volume, thereby yielding a real-time algorithm; and
- Experimental evaluation which demonstrates: (1) The performance of the proposed algorithm is not significantly affected by the choice of the training subject; and (2) The shape description is proposed does not change significantly from one subject to another, which demonstrate a single subject is sufficient for training.

3.2.1 User Initialization and Segmentation Parameters

For evaluation purposes, the RV cavity in the 2D images were segmented by an expert and then automatically segmented contours were compared to the corresponding manually delineated regions.

In order to initialize the algorithms, the user was prompted to plant a seed in the centroid of the LV cavity of the middle slice in the first volume (cardiac phase). Then all volumes were

segmented and the results used to evaluate accuracy of the segmentation.

The following weighting parameters were used:

Step.1: $\alpha_I = 1$, $\alpha_D = 0$, $\alpha_A = 0$, $\beta = 1$, and $\gamma = 107$.

Step.2: $\alpha_I = 0$, $\alpha_D = 0.2$, $\alpha_A = 0.1$, $\beta = 1$, and $\gamma = 65$.

3.2.2 Visual Inspection

Fig. 3.4 depicts a typical example of the results using a $125 \times 125 \times 6$ volume from MRIUWO dataset, and demonstrates a high conformity between the manual and automatic segmentations. It depicts a 3D illustration of the obtained results and the manual surfaces, along with the corresponding 2D contours/images. The volumes are computed as the sum of

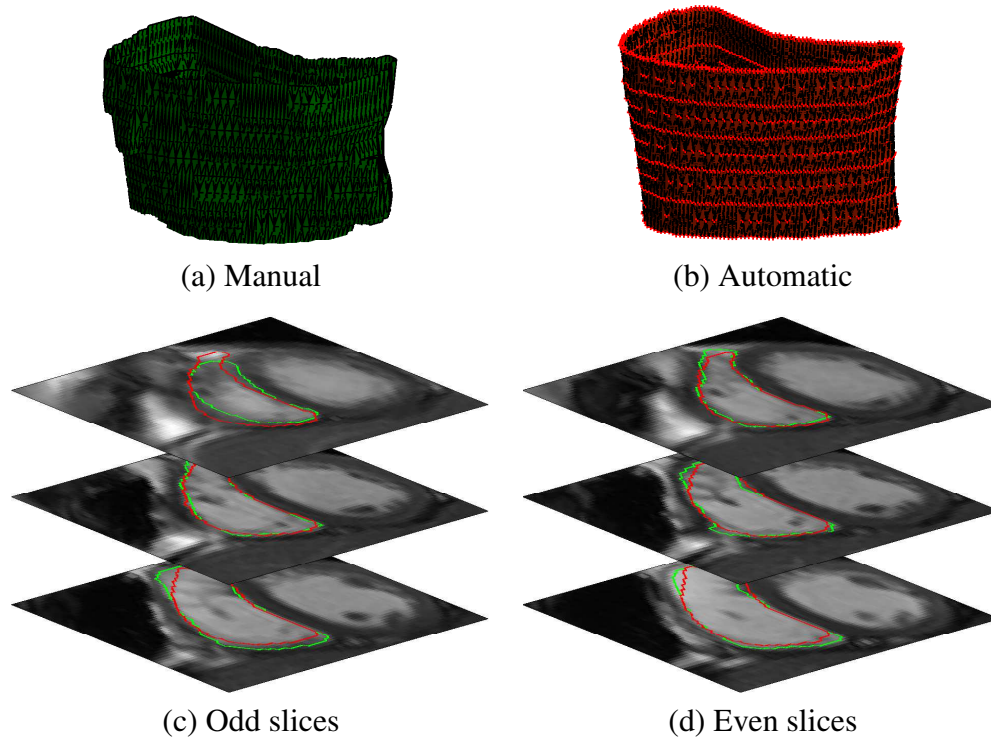


Figure 3.4: A typical example using a $125 \times 125 \times 6$ volume. (a-b): Manual and automatic surfaces; (c-d): The corresponding 2D contours/slices.

the all areas multiplied by inter-slice spacing (8.4 mm). Also, Fig. 3.5 depicts an example of the results from MICCAI'12 dataset using a $216 \times 256 \times 9$ volume, and demonstrates a suitable level of conformity between the manual and automatic segmentations.

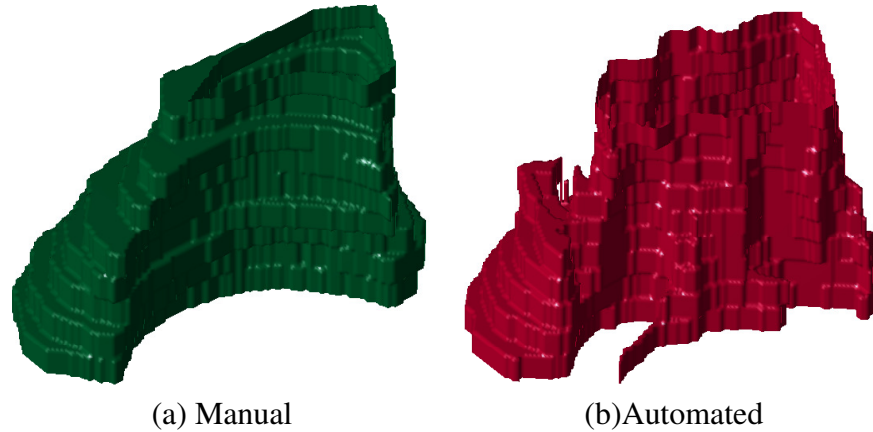


Figure 3.5: An example using a $256 \times 126 \times 9$ volume from MICCAI'12 dataset. The surfaces rendered with a simple nearest neighbour interpolation between each 2 consecutive slices.

3.2.3 Quantitative Performance Evaluations

I proceeded to a leave-one-in validation, where one subject in the training-set was used for training and the remainder of the subjects were employed for the testing. The similarities between the ground truth and my automatic segmentations are assessed using three measures:

Surface-based measures: RMSE and the Hausdorff distance (HD).

Region-based measures: DM, and correlation coefficient (CC).

The details of these metrics are as below:

- *Dice Metric*: commonly used to measure the similarity (overlap) between the automatically detected and ground-truth regions [Ayed et al. \[2009\]](#) and is defined as:

$$DM = \frac{2A_{am}}{A_a + A_m}, \quad (3.26)$$

Where A_a , A_m , and A_{am} correspond to the areas of the segmented region, the hand-labeled region, and the intersection between them² respectively.

- *RMSE*: evaluates root mean square of the perpendicular distances from manual to automatic boundaries and is given by:

$$RMSE = \sqrt{\frac{1}{N} \sum_{i=1}^N \|u_i - v_i\|^2}, \quad (3.27)$$

where u_i is a point on the automatically detected boundary and v_i is the corresponding point on the manually traced boundary (set $N = 240$)³.

- *CC*: The correlation coefficient evaluates the quality of a least squares fitting to the original data. The correlation coefficient between V_a and V_m is estimated for the regions within endo- and epicardium surfaces. $CC \in [0, 1]$, where 1 indicates a perfect match and 0 a total mismatch.

Table 3.2 lists the total number of MR images corresponding with each sub-dataset which were used for the evaluation of the MICCAI'12 dataset. Table 3.3 lists the mean and standard deviation of DM and HD for all the automated and semi-automated algorithms in the challenge.

²The higher the DM, the better the performance. DM is always in $[0, 1]$. $DM \geq 0.80$ indicates an excellent agreement between manual and automatic segmentations.

³The lower RMSE, the better the conformity of the results to the ground truth.

Dataset	number of Subjects	number of images for evaluations
Training	16	243
Test1	16	248
Test2	16	252

Table 3.2: List of MR datasets.

method	SA/A	Test1		Test2	
		HD (<i>mm</i>)	DM	HD (<i>mm</i>)	DM
Ours	A	20.21 ± 9.72	0.59 ± 0.24	22.21 ± 9.69	0.56 ± 0.24
CMIC	A	10.51 ± 9.17	0.78 ± 0.23	12.50 ± 10.95	0.73 ± 0.27
NTUST	A	28.44 ± 23.57	0.57 ± 0.33	22.20 ± 21.74	0.61 ± 0.34
SBIA	A	23.16 ± 19.86	0.55 ± 0.32	15.08 ± 8.91	0.61 ± 0.29
ICL	SA	9.26 ± 4.93	0.78 ± 0.20	9.77 ± 5.59	0.76 ± 0.23
LITIS	SA	9.97 ± 5.49	0.76 ± 0.20	7.28 ± 3.58	0.81 ± 0.16
BIT-UPM	SA	11.15 ± 6.62	0.80 ± 0.19	9.79 ± 5.38	0.77 ± 0.24

Table 3.3: The evaluation results for automatic (A) and semi-automatic (SA) segmentation of the endocardium surfaces; mean and standard deviation of DM and HD. The methods are including CMIC Zuluaga et al. [2012], NTUST Wang et al. [2012], SBIA ou et al. [2012], ICL Bai et al. [2012], LITIS Grosgeorge et al. [2012], BIT-UPM Maier et al. [2012].

The algorithm clinical performance is measured via three different criteria including the End-diastolic (ED) and End-systolic (ES) volume, and the Ejection Fraction (EF). The mean value of DM and HD for the ED and ES cardiac phases is reported in Table. 3.4. I further report the CC and the coefficients of the linear regression line ($Y = aX + b$) for the ED phase in the MICCAI'12 dataset in Table. 3.6. The results demonstrate that the proposed algorithm has achieved a good performance compared to others considering the off-line training load, the run-time speed and accuracy all together. Among four highly automated algorithms, the accuracy of the algorithm is the second best roughly while the algorithm's speed is the highest. The proposed algorithm also requires only one training subject to learn the the distance model from and it was parallelized to be run on GPU. The main reason for being very rapid in segmenting a subject is that unlike other algorithms it does not require any time-consuming registration or pose estimation procedures. Eventually the performance of the algorithm on the MRIUWO

		DM				HD (mm)			
		Test1		Test2		Test1		Test2	
method	SA/A	ED	ES	ED	ES	ED	ES	ED	ES
Ours	A	0.67	0.49	0.77	0.69	17.76	23.19	20.08	24.87
CMIC	A	0.83	0.72	0.77	0.69	9.77	11.41	12.31	12.75
NTUST	A	0.58	0.48	0.71	0.54	27.72	29.30	16.25	26.75
SBIA	A	0.60	0.48	0.67	0.54	22.17	24.37	14.28	16.09
ICL	SA	0.86	0.69	0.82	0.68	7.70	11.16	9.08	10.64
LITIS	SA	0.83	0.69	0.87	0.74	9.48	10.56	6.92	7.73
BIT-UPM	SA	0.86	0.72	0.85	0.67	8.80	14.49	7.88	12.34

Table 3.4: The evaluation results for automatic (A) and semi-automatic (SA) segmentation of endocardium surfaces on the ED and ES phases; mean and standard deviation of DM and HD. The methods are including CMIC Zuluaga et al. [2012], NTUST Wang et al. [2012], SBIA ou et al. [2012], ICL Bai et al. [2012], LITIS Grosgeorge et al. [2012], BIT-UPM Maier et al. [2012].

method	SA/A	Time/sub	User Interaction	Atlas
Ours	A	10 secs	N/A	N/A
CMIC	A	12 mins	N/A	yes
NTUST	A		N/A	yes
SBIA	A		N/A	yes
ICL	SA	5 mins	5 landmarks per volume	yes
LITIS	SA	45 secs	2 landmarks/2D image	yes
BIT-UPM	SA	2.25 mins	4-5 2D manual contours	N/A

Table 3.5: The run-time computation and off-line load for the algorithms.

		Test1			Test2		
method	SA/A	CC	a	b	CC	a	b
Ours	A	0.8	0.8	9.4	0.8	0.8	10.0
CMIC	A	0.9	0.8	3.9	0.9	0.7	5.6
NTUST	A	0.6	1.1	0.7	0.9	1.1	2.1
SBIA	A	0.8	0.8	1.4	0.9	0.7	4.8
ICL	SA	1.0	0.9	0.4	1.0	0.9	0.6
LITIS	SA	0.9	0.9	1.8	1.0	1.0	0.8
BIT-UPM	SA	1.0	1.0	0.9	1.0	1.0	1.2

Table 3.6: Clinical performance for endocardium segmentation: correlation coefficient CC , linear regression coefficients on ED areas (slope a and intercept b).

Dataset	RMSE (mm)	DM	CC	GPU/frame	CPU/frame
MRIUWO	2.30 ± 0.12	0.84 ± 0.07	0.95	0.129 sec	2.72 sec

Table 3.7: Quantitative performance evaluations over the MRIUWO dataset. Evaluations are averaged over the entire dataset. The optimization parameters were fixed for all the subjects.

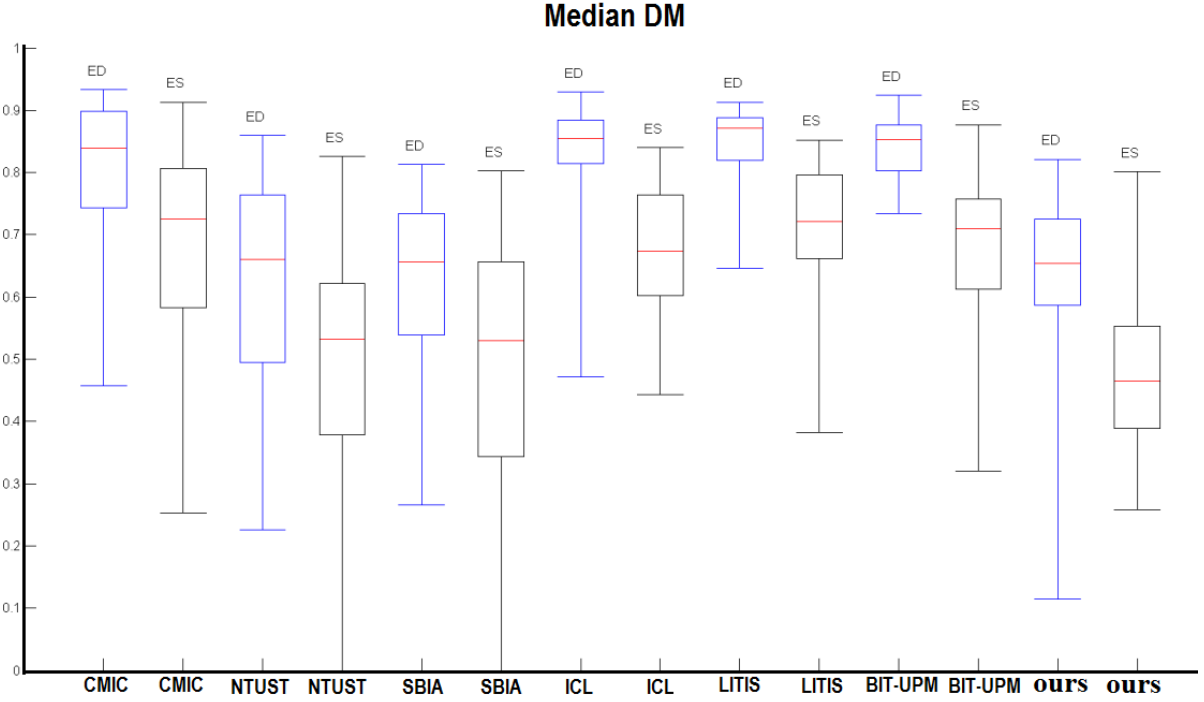


Figure 3.6: Comparison of Median DM for ED and ES phases (Test1 and Test2 datasets together) for all algorithms participated in MICCAI'12 challenge. The median is the middle red bar. The box indicates the lower quartile (splits 25% of lowest data) and the upper quartile (splits 75% of highest data). The whiskers are the maximum and minimum values.

dataset is reported using RMSE, DM and correlation coefficient in Table. 3.7. In Fig. 3.6, the distribution of the DM for each algorithm in the ED and ES phases is illustrated by a box-and-whisker plot. The automated versus manual 3D RV volumes is illustrated along the line ($y = x$) in Fig. 3.7. In order to demonstrate the correlation of the individual volumes with their associated gold-standard, Fig. 3.7b shows the reliability of the algorithm for DM which is measured by:

$$R(d) = Pr(DM > d), \quad d = \text{threshold} \quad (3.28)$$

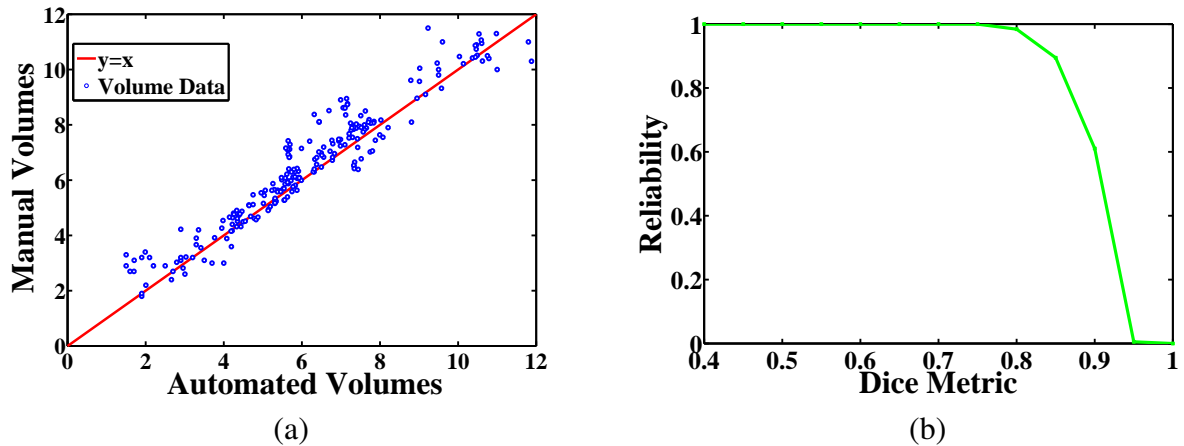


Figure 3.7: (a) Plots the manual volumes versus the automatic volumes for cardiac subjects; (b) Dice metric's reliability: $R(d) = Pr(DM > d)$ for MRIUWO dataset.

$R(d)$ indicates what percentage of DMs in the database are greater than d .

3.2.4 Invariance of the geometric distributions

The invariance of geometric priors is demonstrated in following figures.

1. Fig. 3.8: the angle and distance distributions corresponding to 6 frames per 16 different subjects for RV cavity dataset,
2. Fig.3.9: the angle and distance distributions corresponding to 20 frames per three different sequences (apical, mid-cavity, and basal) of one single subject.

These figures demonstrate that the angle distributions are very similar while the distance distributions follow a similar pattern but have different supports and are shifted. These results demonstrate that the variations of the size of the region (e.g. blood cavity over the phases) do not cause a meaningful change in the pattern of the angle distributions, while they do demon-

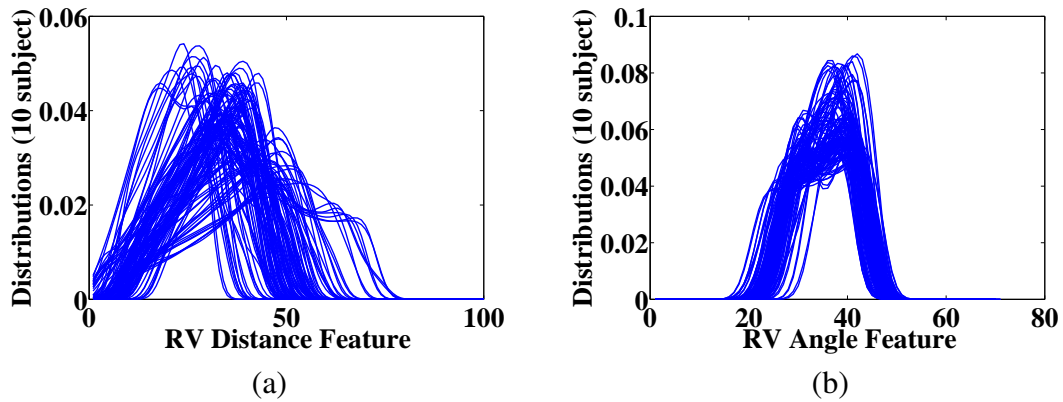


Figure 3.8: Invariance of the angle and distance distributions. 16 subjects, 6 frames from apical to basal per each subject. The distributions have been superimposed for (a) distance and (b) angle priors. The distributions were estimated using 192 bins and a kernel width $\sigma = 2$.

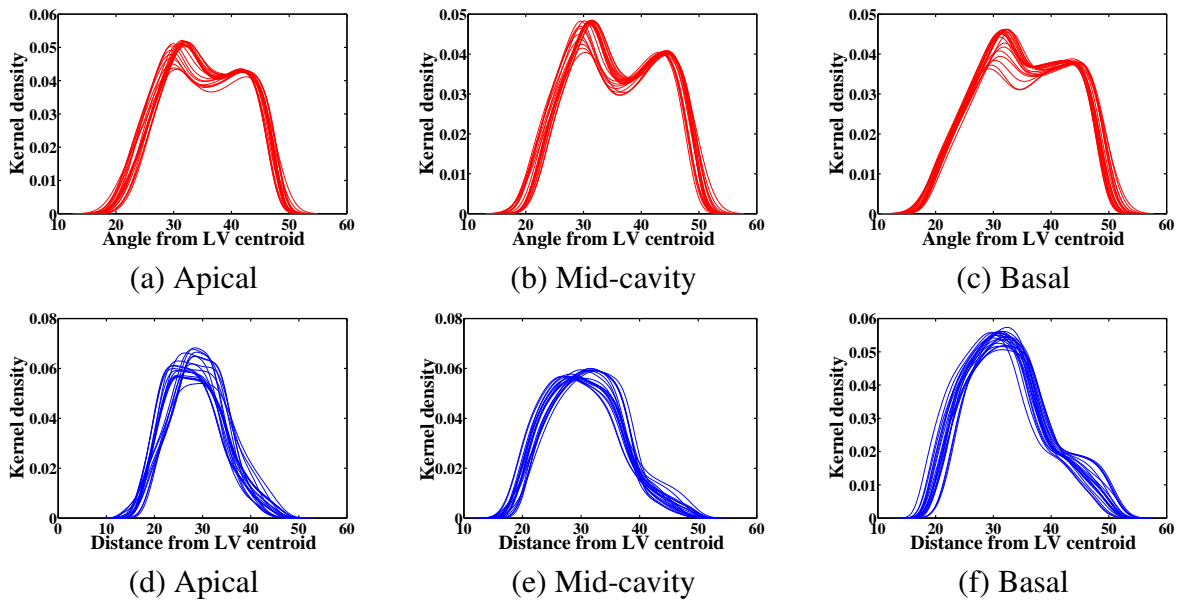


Figure 3.9: The angle and distance distributions for the RV cavity for 20 frames from different sequences (Apical, Basal, Mid-cavity) belonging to a single subject. To measure the distributions, the manually segmented contours were used. 1st row: cosine of angles; 2nd row: distances from LV centroid. 1st column: apical slices; 2nd column: mid-cavity slices; 3rd column: basal slices.

strate a slight shift in the distance distributions. These shifts, which are due to inter-subject variations in scale, are handled efficiently with the proposed fixed-point-equation computations. The experiments support the fact that a single region is sufficient for training, and confirms the relevance of the proposed priors to the RV segmentation.

3.2.5 Robustness with respect to the choice of training subject:

I proceeded to a comprehensive leave-one-in evaluation method consisting of 20 tests, each corresponding to the choice of a different training subject. Then, the entire dataset is segmented and the corresponding average DM and $RMSE$ are measured. Figs. 3.10 (a) and (b) plot the obtained average DM and $RMSE$ as functions of the index of the training subject, demonstrating a very low variation.

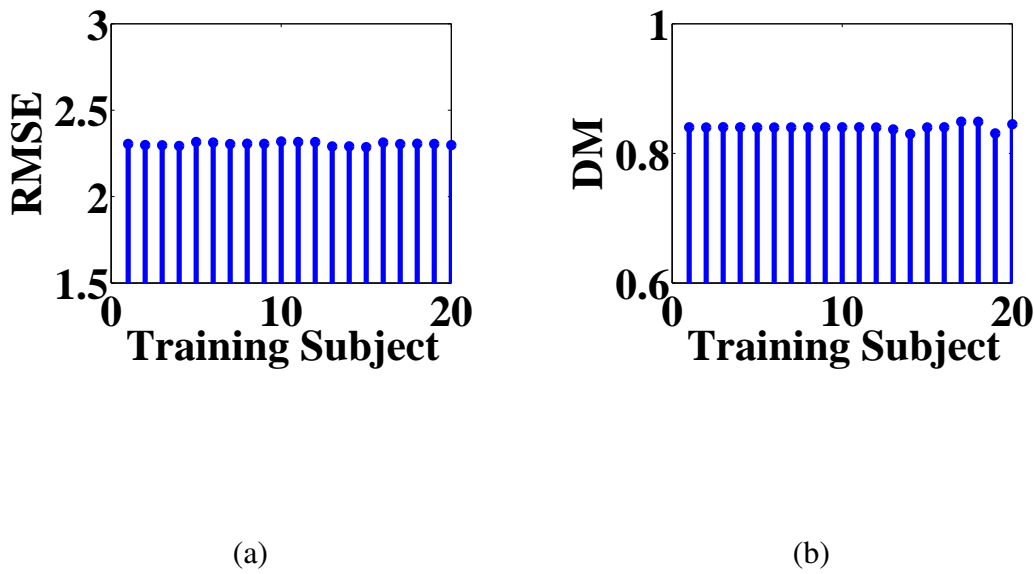


Figure 3.10: (a) and (b): Robustness of the proposed algorithm with respect to the choice of the training subject, (c): Invariance of the distance-based shape model.

3.3 Discussion

In this chapter, I proposed a unique solution to automated 3D RV image segmentation, which has not received much attention in the literature, using object-interaction priors in short-axis

MRI. The solution was obtained with a convex-relaxation optimization of two original functionals, each containing two distribution-matching priors, one encoding intensity information and the other shape information. The novel shape prior (distance and angle distributions) that was used in this chapter takes into account the RV position and interactions with the LV cavity and its centroid. The shape prior is intrinsically invariant with respect to translation and scale. A bound on the Bhattacharya distance between distributions was used that allowed me to embed descriptors for intensity distributions along with scale- and translation-invariant distance and angle distributions. The proposed algorithm relaxes the need for costly pose estimation (or registration) procedures and large training sets, and can tolerate shape deformations, unlike template (or atlas) based priors.

Furthermore, the robustness of the method was tested experimentally by showing that the performance of the algorithm is not significantly affected by the choice of the training subject, and the utilized shape description does not change significantly from one subject to another. The algorithm was evaluated using two different datasets. The algorithm was compared quantitatively with six other novel automated and semi-automated algorithms participated in the public challenge in MICCAI, 2012. Considering speed, user efforts, and accuracy of the algorithms, our results demonstrated that the proposed algorithm achieves an overall good performance amongst all other highly automated algorithms. Majority of the participated algorithms are based on atlas and registration algorithms which require extensive user interventions during the testing and training phases. The promising results also demonstrate that with further developments it is feasible to use the algorithm in current clinical routines.

Bibliography

I. Ben Ayed, S. Li, and I. Ross. Embedding overlap priors in variational left ventricle tracking. *IEEE Transactions on Medical Imaging*, 28(12):1902–1913, 2009.

W. Bai, W. Shi, H. Wang, N. S. Peters, and D. Rueckert. Multi-atlas based segmentation with local label fusion for right ventricle MR images. *Medical Image Computing and Computer-Assisted Intervention (MICCAI), Workshop on RV Segmentation Challenge in Cardiac MRI*, 2012.

D. P. Bertsekas. *Nonlinear Programming*. Athena Scientific, 1999.

A. Chambolle. An algorithm for total variation minimization and applications. *Journal of Mathematical Imaging and Vision*, 20(1-2):89–97, 2004.

I. Ekeland and R. Téman. *Convex analysis and variational problems*. Society for Industrial and Applied Mathematics, Philadelphia, PA, USA, 1999.

D. Grosgeorge, C. Petitjean, and S. Ruan. Right ventricle segmentation by graph cut with shape prior. *Medical Image Computing and Computer-Assisted Intervention (MICCAI), Workshop on RV Segmentation Challenge in Cardiac MRI*, 2012.

- T. Jebara, R.I. Kondor, and A. Howard. Probability product kernels. *Journal of Machine Learning Research*, 5:819844, 2004.
- O. M. O. Maier, D. Jimenez-Carretero, A. Santos, and M.J. Ledesma-Carbayo. Right-ventricle segmentation with 4D region-merging graph cuts in MR. *Medical Image Computing and Computer-Assisted Intervention (MICCAI), Workshop on RV Segmentation Challenge in Cardiac MRI*, 2012.
- M. Nikolova, S. Esedoglu, and T. F. Chan. Algorithms for finding global minimizers of image segmentation and denoising models. *SIAM Journal of Applied Mathematics*, 66(5):1632–1648, 2006.
- Y. ou, J. Doshi, G. Erus, and C. Davatzikos. Multi-atlas segmentation of the cardiac MR right ventricle. *Medical Image Computing and Computer-Assisted Intervention (MICCAI), Workshop on RV Segmentation Challenge in Cardiac MRI*, 2012.
- C.-W. Wang, C.-W. Peng, and H.-C. Chen. A simple and fully automatic right ventricle segmentation method for 4-dimensional cardiac MR images. *Medical Image Computing and Computer-Assisted Intervention (MICCAI), Workshop on RV Segmentation Challenge in Cardiac MRI*, 2012.
- J. Yuan, E. Bae, and X.-C. Tai. A study on continuous max-flow and min-cut approaches. In *IEEE International Conference on Computer Vision and Pattern Recognition (CVPR)*, 2010.
- Z. Zhihua, J. T. Kwok, and D.-Y. Yeung. Surrogate maximization/minimization algorithms and extensions. *Machine Learning*, 69:1–33, 2007.

- M. A. Zuluaga, M. J. Cardoso, and S. Ourselin. Automatic right ventricle segmentation using multi-label fusion in cardiac MRI. *Medical Image Computing and Computer-Assisted Intervention (MICCAI), Workshop on RV Segmentation Challenge in Cardiac MRI, 2012.*

Chapter 4

ANN Learned Information Measures for LV Myocardium Abnormality Detection

In this chapter¹, I investigate an information-theoretic based ANN for normal/abnormal LV myocardium motion classification. The proposed framework comprises a 3-layer supervised ANN which uses a hyperbolic tangent sigmoid for hidden layer and a linear transfer function for the output layer as activation functions.

The classification process starts with the segmentation of myocardium in cine MRI and ends with a classifier which decides if each segment of myocardium is normal or abnormal. Using the LV segmentation contours from chapter 2, points are estimated over the LV cavity

1

this chapter is based on the paper below:

1. Cyrus M. S. Nambakhsh, Kumaradevan Punithakumar, Ismail Ben Ayed, Aashish Goela, Ali Islam, Terry Peters, Shuo Li, A neural network learned information measures for heart motion abnormality detection, Proc. SPIE, Image Processing, March 2011.

via a Kalman filter and a recursive dynamic Bayesian filter, and some statistical information of the points such as radial distance and velocity are measured. Distributions of the statistical information for the entire 4D (3D+time) subject are built using a kernel density estimate. However, experiments show there is a high degree of similarity between the distributions of statistical information belonging to normal and abnormal segments. Fig. 4.1 illustrates an example for radial velocity of normal and abnormal cases. To solve the problem, studies in

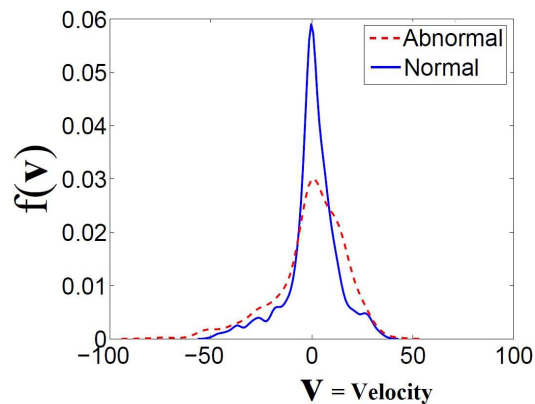


Figure 4.1: Distributions of radial velocity of all normal (blue) and abnormal (red) points in my dataset.

the literature approached the problem with a set of global information-theoretic measures such as SDE, Renyi entropy and Fisher information [Pierce \[1980\]](#), [Khinchin](#). However, the distributions of information-theoretic measures are still fairly overlapped which results in a low classification accuracy [Punithakumar et al. \[2010\]](#).

Contribution of this chapter is using a multi-layer feed-forward off-the-shelf ANN (using MATLAB) which employs the information-theoretic measures of the LV wall motion as a set of features and classifies the normal and abnormal cases.

4.1 Preprocessing of data

The application of information theory in medical image analysis is still in early stages, although information-theoretic have been utilized in physics [Frieden \[1999\]](#) and computer vision [Kim et al. \[2005\]](#), [Ayed et al. \[2008\]](#). Information-theoretic are global measurements of the distribution of a given characteristic of a subject. Information-theoretic measures such as SDE, Fisher information and Renyi entropy have shown a better classification ability compared to statistical criteria such as the mean in classifying distributions of normal and abnormal wall motion cases [Punithakumar et al. \[2010\]](#). A few other medical imaging applications in which information-theoretics have played fundamental role include measuring the heart rate Gaussianity using the Renyi entropy [Lake \[2006\]](#), and analyzing heart period variability using Shannon entropy [Porta et al. \[2001\]](#).

4.1.1 Information theory and cardiac motion abnormality detection

Fig. 4.2 shows an example of abnormal and normal LV wall motion along with the corresponding kernel density estimates of motion measurements such as radial distance and velocity [Punithakumar et al. \[2010\]](#). As illustrated, the distributions of normal and abnormal segments are highly overlapped. Using moments² of these distributions such as mean results in very close values for both normal and abnormal distributions, demonstrating the challenge associated with the classifier (captions in Fig. 4.2c and d).

²A moment is a scalar measure of the shape of a set of points. The 2nd moment measures the “width” of a set of points in one dimension.

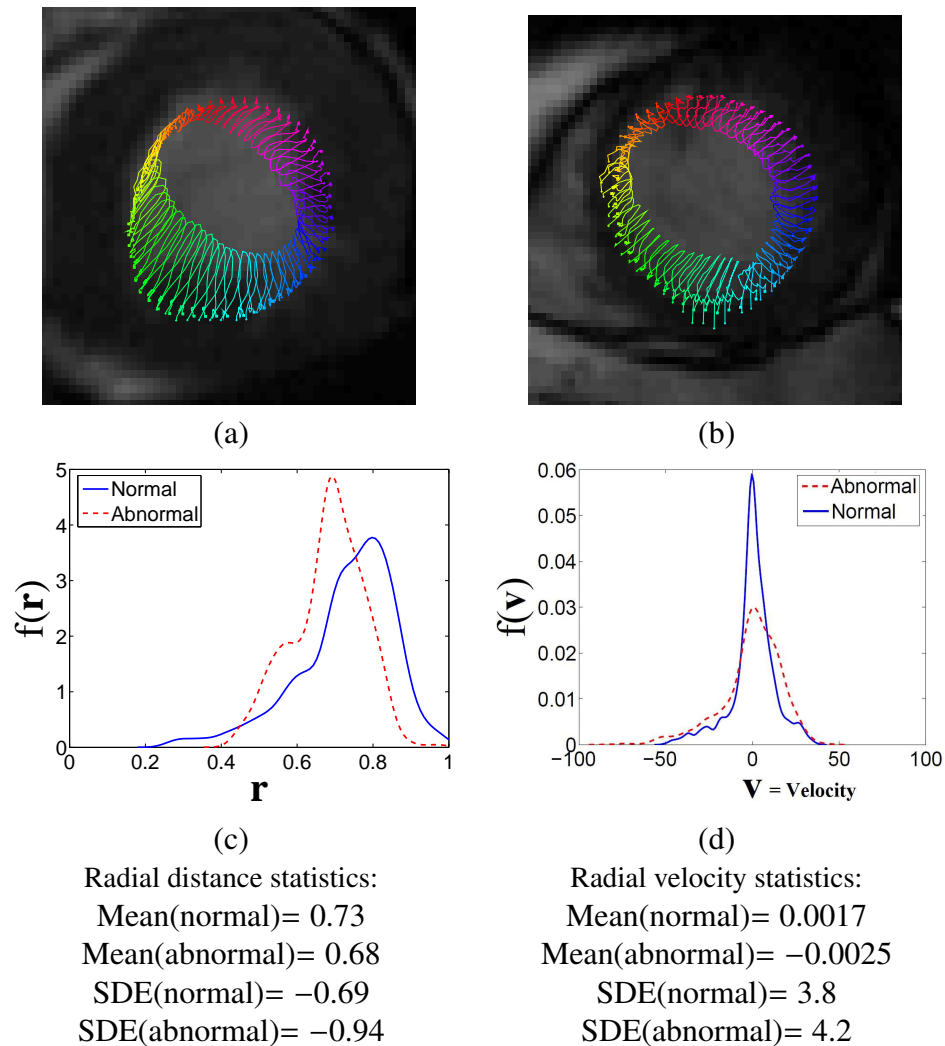


Figure 4.2: The power of the SDE compared to the Mean in classifying ab/normal motions. (a) typical normal, (b) typical abnormal heart motion trajectory, (c) and (d) corresponding distributions of radial distance and velocity. SDE unlike the Mean is able to create a more discriminative margin between normal and abnormal motion distributions despite a significant overlap between them; the figures are from Punithakumar et al. [2010].

4.1.2 Tracking the endocardium boundary motion

In this section, I investigate sampling the points over the cavity boundary and subsequent tracking of them over temporal phases. As illustrated in Fig.4.3, the purpose of this approach is to track a point such as P_1 over n temporal phases and measure statistical parameters such as radial distance (r) and radial velocity (variation of the distance over temporal phases).

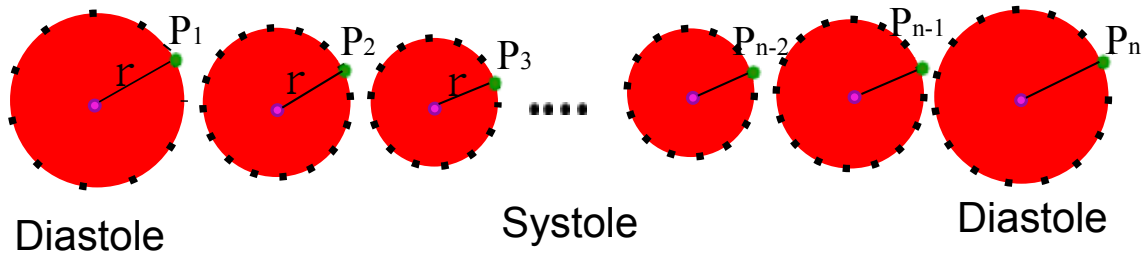


Figure 4.3: An illustration of segmented cavity region and sampled contour. Each point such as P_1 on the boundary of far left contour should be tracked over cardiac temporal phases from systolic (middle contour) to diastolic (far right and left). The pink point is the centroid of the cavity and r is the distance of an assumed point (P_i) to the centroid (radial radial).

Having the automatically delineated segmentation contours, let (x, y) be a Cartesian coordinate of a point such as P_1 on the cavity boundary in Fig. 4.3. A state vector is defined that describes the dynamics of the point in each direction. For x-direction assume $\xi = [\bar{x} \ x \ \dot{x}]^T$ where x is radial distance, and \bar{x} and \dot{x} describe the mean and velocity of the point respectively over a cardiac cycle. Considering the heart motion to be periodic, a *continuous state-space* model as below can be used to represent it [Punithakumar et al. \[2010\]](#):

$$\dot{\xi}(t) = \begin{bmatrix} 0 & 0 & 0 \\ 0 & 0 & 1 \\ \omega^2 & -\omega^2 & 0 \end{bmatrix} \xi(t) + \begin{bmatrix} 1 & 0 \\ 0 & 0 \\ 0 & 1 \end{bmatrix} w(t), \quad (4.1)$$

where ω and $w(t)$ are the angular frequency and the white noise. Model (4.1) is linear for a given ω . The *discrete-time equivalent* of (4.1) is as follows.

$$\xi_{k+1} = \begin{bmatrix} 1 & 0 & 0 \\ 1 - \cos(\omega T) & \cos(\omega T) & \frac{1}{\omega} \sin(\omega T) \\ \omega \sin(\omega T) & -\omega \sin(\omega T) & \cos(\omega T) \end{bmatrix} \xi_k + w_k = F_{cy}(k)\xi_k + w_k \quad (4.2)$$

Now combine the vector along X and Y axis and construct $\mathbf{s} = [\bar{x} \ \dot{x} \ \bar{y} \ \dot{y}]^T$ to describe the dynamics of points in x-y plane. The discrete state-space model in this plane is obtained as follows [Punithakumar et al. \[2010\]](#),

$$\mathbf{s}_{k+1} = \begin{bmatrix} F_{cy}(k) & \mathbf{0}_{3 \times 3} \\ \mathbf{0}_{3 \times 3} & F_{cy}(k) \end{bmatrix} \mathbf{s}_k + \mathbf{v}_k = F_k \mathbf{s}_k + \mathbf{v}_k. \quad (4.3)$$

The recursive Bayesian Filtering and Kalman filter

The Kalman filter results in desired parameters from uncertain and inaccurate observations. It is a recursive process so that new measurements are processed as they are obtained. The Kalman filter is optimal in the sense that if the noise is Gaussian, the Kalman filter minimizes the mean square error of the estimated parameters. If noise is not Gaussian, and given only the mean and standard deviation of the noise, the Kalman filter is the best linear estimator. Kalman filtering has been very popular in many applications because:

1. It has a good performance due to optimality and structure
2. It is suitable for real-time processing

3. It has an inexpensive and simple formulation and implementation.

4. Its measurement equations do not require inversion

Let $z_t = [z_{t,x} \ z_{t,y}]^T$ be the measurement along x and y axis at time step $t \in [1, \dots, K]$.

Then, the state measurement equation is given by

$$z_t = H_t s_t + v_t, \quad (4.4)$$

where

$$H_t = \begin{bmatrix} 0 & 1 & 0 & 0 & 0 & 0 \\ 0 & 0 & 0 & 0 & 1 & 0 \end{bmatrix} \quad (4.5)$$

The variance of v_t needs to be known to implement the Kalman filter. v_t is a zero-mean Gaussian noise sequence with covariance

$$R_t = \begin{bmatrix} r & 0 \\ 0 & r \end{bmatrix}. \quad (4.6)$$

Given the initial state and covariance of v_t , there have sufficient information to find the optimal state estimate using the Kalman filter equations, which can be approached by splitting the recursive processing into a few steps. Fig. 4.4 shows a block diagram of the state estimation by the kalman filter, which recursively estimates the state of the system and the uncertainty or covariance of the estimate (P_t), updating the estimate using a state transition model and measurements.

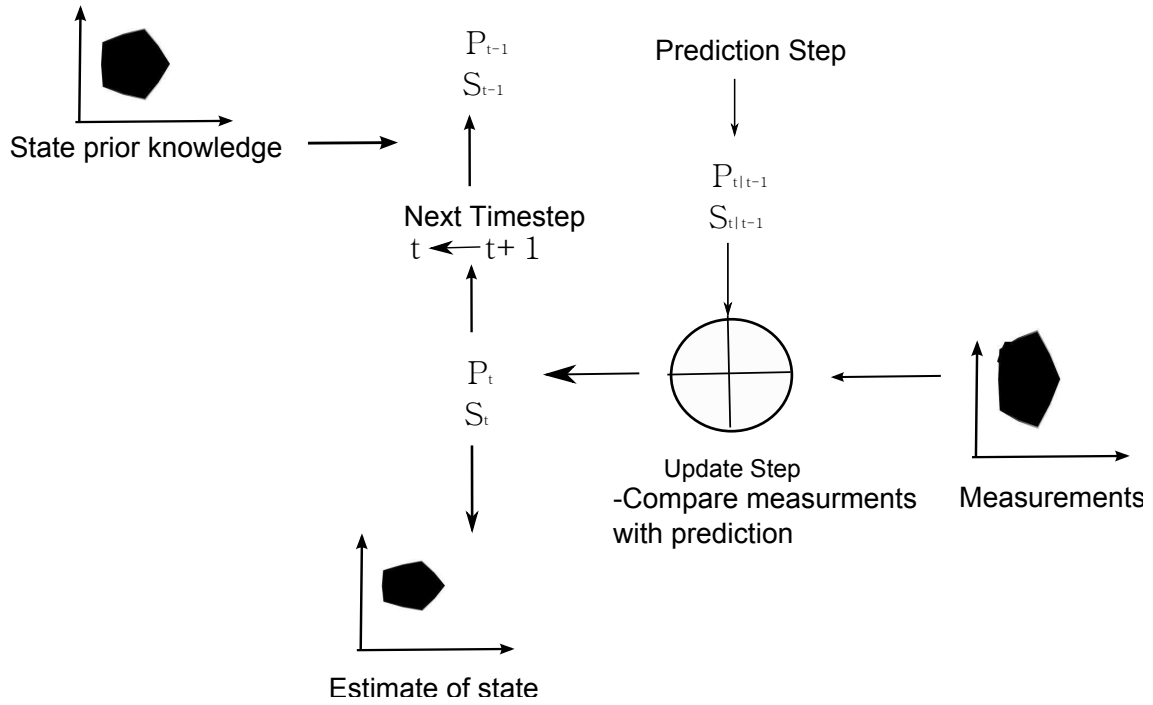


Figure 4.4: The block diagram of Kalman Filter. P_t is state prediction covariance and S_t the state.

State Prediction

Following the state equation (4.3) and using expectation of $z_{1:k} = \{z_1, \dots, z_k\}$, the predicted state is formulated as $\mathbf{m}_t = \mathbb{E}[\mathbf{s}_t]$ where \mathbf{m}_t is the average of the state vector [Punithakumar et al. \[2010\]](#). The state prediction equation is formulated by

$$\mathbf{m}_{t+1}^- = F_t \mathbf{m}_t. \quad (4.7)$$

The corresponding *state prediction covariance* as mentioned in Fig. 4.4 is given by

$$P_{t+1}^- = F_t P_t F_t^T + Q_t. \quad (4.8)$$

Time Update

The *updated state estimate* is given by

$$\mathbf{m}_{t+1} = \mathbf{m}_{t+1}^- + W_{t+1} \nu_{t+1}. \quad (4.9)$$

The *updated state covariance* is calculated as

$$P_{t+1} = P_{t+1}^- - W_{t+1} S_{t+1} W_{t+1}^T. \quad (4.10)$$

Where ν_t (*measurement residual*) is given by [Punithakumar et al. \[2010\]](#):

$$\nu_{t+1} = z_t - H_t \mathbf{m}_{t+1}^-, \quad (4.11)$$

and the W_t as Kalman Gain is computed by

$$W_{t+1} = P_{t+1}^- S_{t+1}^{-1}. \quad (4.12)$$

Filter Initialization

A *two-point differencing* approach [Yaakov et al. \[2002\]](#) is employed to set initial position and velocity of the state. The initial position and velocity along the x -axis are given by

$$\hat{\mathbf{x}}_1 = z_{1,x} \quad (4.13)$$

$$\hat{\dot{\mathbf{x}}}_1 = \frac{(z_{2,x} - z_{1,x})}{T}. \quad (4.14)$$

The average position over the cardiac cycle \bar{x} is initialized by taking the expectation over all the measurements:

$$\hat{\bar{x}}_1 = \frac{1}{K} \sum_{k=1}^K z_{k,x} \quad (4.15)$$

The corresponding initial covariance is given by

$$P_1 = \begin{bmatrix} \Phi_1 & \mathbf{0}_{3 \times 3} \\ \mathbf{0}_{3 \times 3} & \Phi_1 \end{bmatrix}, \quad (4.16)$$

where

$$\Phi_1 = \begin{bmatrix} r & \frac{r}{K} & \frac{r}{KT} \\ \frac{r}{K} & r & \frac{r}{T} \\ \frac{r}{KT} & \frac{r}{T} & \frac{2r}{T^2} \end{bmatrix}. \quad (4.17)$$

Inconsistencies of the segmentation results over cardiac cycle is removed by measuring the centroid of the LV as following,

Let $\{s_k^i = [\bar{x}_k^i \ x_k^i \ \dot{x}_k^i \ \bar{y}_k^i \ y_k^i \ \dot{y}_k^i]^T : i = 1, \dots, N\}$ be a sample point on the LV endocardium boundary in a given frame k . The centroid of the LV cavity $(c_{x,k} \ c_{y,k})$ is defined as follows,

$$\begin{cases} c_{x,k} &= \frac{1}{N} \sum_{i=1}^N x_k^i \\ c_{y,k} &= \frac{1}{N} \sum_{i=1}^N y_k^i \end{cases} \quad (4.18)$$

All the segmentation results falling in $\sqrt{(c_{x,k+1} - c_{x,k})^2 + (c_{y,k+1} - c_{y,k})^2} > k$ are ignored, where k is a predefined constant. Subsequently, the sample points were only predicted using the dynamic model, i.e., they were not updated by the filter [Punithakumar et al. \[2010\]](#). The

trajectory of each point over temporal phases is estimated by

1. sampling each contour to N_s points;
2. selecting only N points using spline interpolation;
3. putting together points over consecutive frames using the *symmetric nearest neighbor correspondences*.

In this study, the radial distance for each point is normalized with respect to the maximum value in the dataset [Punithakumar et al. \[2010\]](#), and subsequently, a Gaussian Kernel Density Estimation (KDE) is applied to obtain the probability density of the points.

4.1.3 The SDE, Fisher information and Rényi entropy of normalized radial distance

Let $\mathbf{r} \in \mathbb{R}$ be a random variable. The kernel density estimate of \mathbf{r} is given by

$$f(\mathbf{r}) = \frac{\sum_{i,t} \mathcal{K}_\sigma(r_t^i - \mathbf{r})}{N \times K}, \quad (4.19)$$

where

$$\mathcal{K}_\sigma(y) = \frac{1}{\sqrt{2\pi\sigma^2}} \exp\left(-\frac{y^2}{2\sigma^2}\right) \quad (4.20)$$

is the Gaussian kernel.

Three information-theoretic criteria are derived to measure the *global* information as follows,

1. SDE:

$$S_f = - \int_{\mathbf{r} \in \mathbb{R}} \frac{\sum_{i,t} \mathcal{K}_\sigma(r_t^i - \mathbf{r})}{NK} \left(\ln \sum_{i,t} \mathcal{K}_\sigma(r_t^i - \mathbf{r}) - \ln NK \right) d\mathbf{r} \quad (4.21)$$

2. Rényi entropy

$$R_f^\alpha = \frac{1}{1-\alpha} \ln \int_{\mathbf{r} \in \mathbb{R}} \left(\frac{\sum_{i,t} \mathcal{K}_\sigma(r_t^i - \mathbf{r})}{NK} \right)^\alpha d\mathbf{r} \quad 0 < \alpha < \infty, \alpha \neq 1, \quad (4.22)$$

3. Fisher information

$$I_f = 4 \int_{\mathbf{r} \in \mathbb{R}} |\nabla g(\mathbf{r})|^2 d\mathbf{r}, \quad (4.23)$$

where

$$g(\mathbf{r}) = \sqrt{\frac{\sum_{i,t} \mathcal{U}_\sigma(r_t^i - \mathbf{r})}{NK}} \quad (4.24)$$

4.1.4 Artificial feed-forward back-propagation neural network

I propose a non-linear classification of the aforementioned distributions using an multi layer perceptron ANN. The ANN builds a nonlinear relation between the inputs and clusters of the output to distinctively separate overlapped classes of inputs. Below is the relationship between input vector \mathbf{X} and the output vector \mathbf{Y} ,

$$\mathbf{Y} = F \left[\sum W^{h_{(n-1)}} \dots \tanh \left(\sum \mathbf{W}^{h_1} \cdot \tanh(\mathbf{W}^{h_0} \cdot \mathbf{X}) \right) \right] \quad (4.25)$$

where \mathbf{X} is a matrix of inputs, F a thresholding or step function, \mathbf{W}^{h_i} is a matrix of weights in consecutive layers $i = 0 \dots n - 1$ and \mathbf{Y} the output classes, where the best \mathbf{W} must be found

corresponding to the least error in estimating \mathbf{Y} .

Training:

As mentioned previously, ANN is used to implement a non-linear relationship between \mathbf{Y} and \mathbf{X} in (4.25). The ANN is trained with \mathbf{X} as,

$$\mathbf{X} = (X_1, X_2, \dots, X_n)^T = (S_f, I_f, R_f^\alpha, \mu_r, \mu_v)^T \quad (4.26)$$

where μ_r and μ_v are mean radial distance and velocity respectively. The output vector $\mathbf{Y} \in \{0, 1\}$. The dataset is split into a training set $\{(\mathbf{X}^j, \mathbf{Y}^j); j \in I_r\}$ and a testing set $\{(\mathbf{X}^j, \mathbf{Y}^j); j \in I_t\}$. The network in its simplest form comprises of a single neuron as shown in Fig. 4.5a. The applied ANN uses a hyperbolic tangent function, $F(x) = \tanh(x)$, as the activation function in hidden layers and a step function in the output layer. To train the network a back propagation gradient descent algorithm was used to adjust the weights to reduce the network's error in the output.

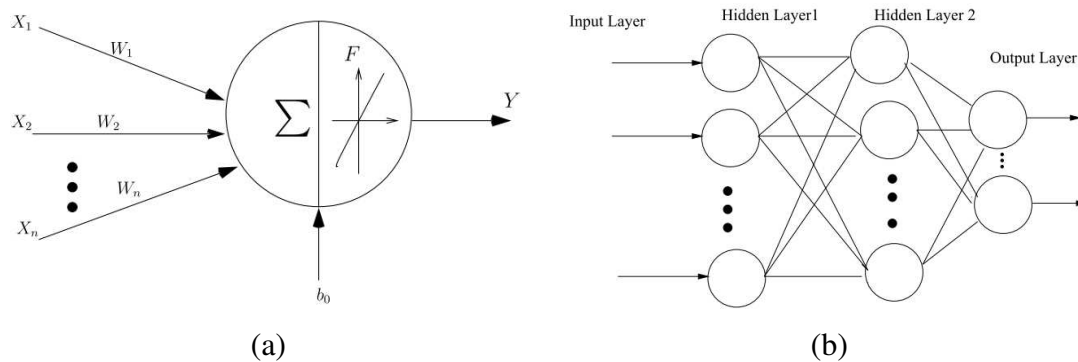


Figure 4.5: a) A node in ANN model, and b) General structure of the ANN.

Testing:

After the training procedure, the weight vector, \mathbf{W} , is configured and remains constant. Having the ANN trained, a single node in the network (Fig. 4.5) is fed with \mathbf{X}^t during testing procedure. The output of the neuron is computed as

$$\hat{\mathbf{Y}}_k^t = \tanh(\mathbf{W} \cdot \mathbf{X}_k^t) \quad (4.27)$$

which, following substitution of (4.26) into (4.27) yields:

$$\hat{\mathbf{Y}}_k^t = \tanh(W_1 \cdot S_f(k) + W_2 \cdot I_f(k) + W_3 \cdot R_f^\alpha(k) + b_0) \quad (4.28)$$

where k is the k th sample of the testing set and b_0 is bias to the neuron. Assuming that the ANN contains a single hidden layer, and that there are n neurons in this layer, the ultimate output is expressed as

$$\mathbf{Y}_{out} = F_{step}(\mathbf{W}^h \cdot \mathbf{Z} + b_{out}) \quad (4.29)$$

$$\mathbf{Z}(i) = \hat{\mathbf{Y}}^t(i) \quad (4.30)$$

where F_{step} is a step function, $\hat{\mathbf{Y}}^t(i)$ is the output of i th neuron in the hidden layer (4.27), \mathbf{W}^h is the weight vector connecting the neurons in the hidden layer to the neuron in the output layer and b_{out} is bias to the output neuron. Note that the ANN in this study has a single neuron in the output layer.

4.2 Experiments

In this chapter, a database of 395 short-axis MRI sequences, each consisting of 20 cine 2D-images acquired from 30 normal and 18 abnormal subjects, was used for evaluation purposes. The images were acquired using 1.5T MRI scanners with a steady state acquisition (FIESTA) image sequence.

I compared the proposed ANN classifier with other classifiers such as SVM using linear kernel (off-the-shelf Matlab library was used), the mean radial displacement, the mean systolic radial velocity, the SDE, the Rényi entropy ($\alpha = 2$) and the Fisher information. For KDEs, a kernel with a bandwidth of 0.5 was employed.

For evaluation purposes, the results were compared with the ground truth as determined by a radiologist. The assumption is that a myocardium segment in a sequence is diagnosed as abnormal if the point in that segment falls within abnormal distribution. To evaluate the classifier, a *leave-one-subject-out* approach was used. Fig. 4.6 illustrates the ROC curves and the corresponding AUCs to demonstrate the performance of the classifier. Furthermore, the discriminative ability of the classifiers was assessed by the Bhattacharyya measure. Table 4.1 summarizes the quantified results.

Fig. 4.6 demonstrates that the proposed ANN has a better classification accuracy than the SVM and information-theoretic classifiers. The closer the curve to the upper left corner, the better the classification performance. The ANN's ROC curve has the most proximity to an ideal step function among all other classifiers. It yields a sensitivity of 91% and a specificity of 90%.

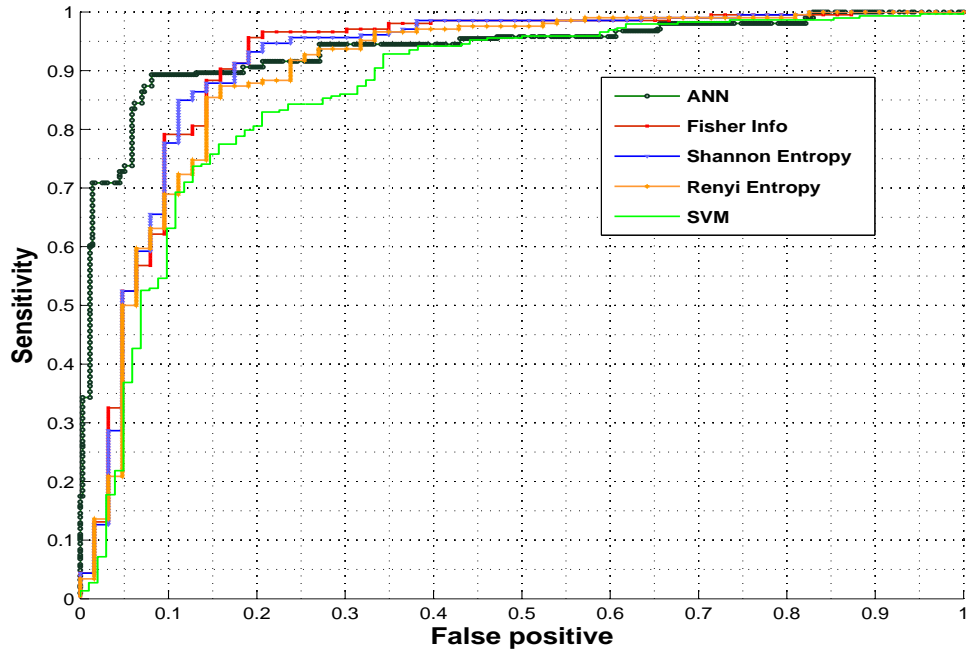


Figure 4.6: Receiver operating characteristics of the ANN, Information-theoretic and SVM classifiers are illustrated.

The AUC represents the average sensitivity of the classifier versus specificity resulting from thresholding of the classifiers outputs. The corresponding AUCs are listed in Table 4.1. The ANN yielded the highest AUC which is of 93.2, resulting in the best overall performance.

The Bhattacharyya distance metric (\mathcal{B}) Comaniciu et al. [2003] was employed to evaluate the discriminative power of the classifiers over normal and abnormal walls as well.

$$\mathcal{B} = \sqrt{1 - \sum_{y \in \mathbb{R}} \sqrt{f_N(y)f_A(y)}}, f_N = \text{normal distribution}, f_A = \text{abnormal distribution} \quad (4.31)$$

Higher \mathcal{B} means lesser the overlap and better the classifier. The ANN yielded the highest \mathcal{B} as shown in Fig. 4.7 and reported in Table 4.1.

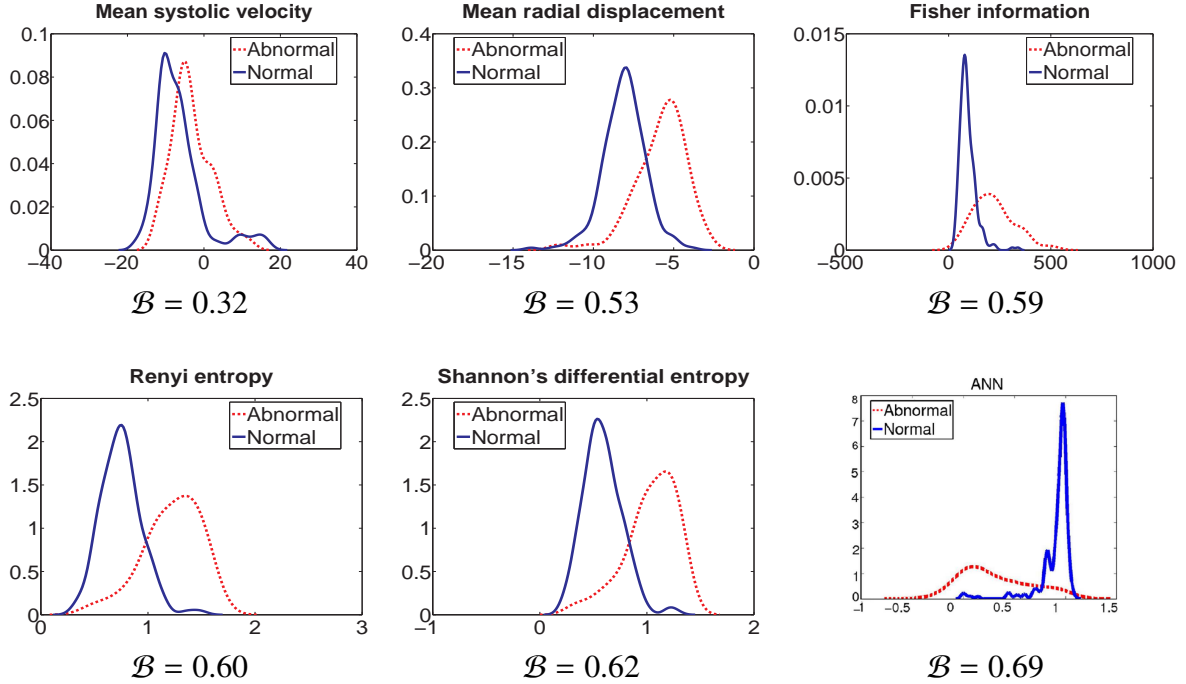


Figure 4.7: Distribution of normal and abnormal hearts using different classifiers.

Classifier element	AUC (%)	\mathcal{B}	Classification accuracy	
			Abnormal (%)	Normal (%)
ANN	93.2	0.69	91.0	90.0
SVM	86.50	0.61	85.0	75.0
Mean systolic velocity	70.8	0.32	79.4	54.9
Fisher information	89.3	0.59	84.1	85.0
Rényi entropy	90.8	0.60	87.3	84.5
Shannon's differential entropy	90.9	0.62	90.5	78.6

Table 4.1: The AUC, \mathcal{B} and accuracy of the classifiers corresponding to Fig. 4.6 and Fig. 4.7.

4.3 Conclusions

I derived an ANN to classify the LV motion based on information theoretic measures. The ANN was fed by global measurements of distributions of the wall motion such as SDE, and Fisher information along with local measurements such as mean. The ANN was examined by different combinations of the input features to determine the best combination. Moreover, the ANN structure was subject to modifications of number of layers, nodes and activation function

to obtain the best performance. The proposed method was devised based on quantitative wall motion analysis. The distributions of the radial distance and velocity are the best replica of the approach radiologists trace the abnormal motions qualitatively. The results according to ROC, AUCs, Bhattacharyya distance metrics, and *leave-one-out* cross validation demonstrate that the proposed ANN can lead to a significant improvement over other classifiers in the literature.

Bibliography

- I. Ben Ayed, S. Li, and I. Ross. Tracking distributions with an overlap prior. In *IEEE Conference on Computer Vision and Pattern Recognition*, pages 1–7, June 2008.
- D. Comaniciu, V. Ramesh, and P. Meer. Kernel-based object tracking. *IEEE Transactions on Pattern Analysis and Machine Intelligence*, 25(5):564–575, 2003.
- B. R. Frieden. *Physics from Fisher Information: A Unification*. Cambridge University Press, January 1999.
- A. I. A. Khinchin. *Mathematical Foundations of Information Theory*. Dover Publications, Incorporated, 1957.
- J. Kim, J. W. Fisher, A. J. Yezzi., M. Cetin, and A. S. Willsky. A nonparametric statistical method for image segmentation using information theory and curve evolution. *IEEE Transactions on Image Processing*, 14(10):1486–1502, 2005.
- D. E. Lake. Renyi entropy measures of heart rate gaussianity. *IEEE Transactions on Biomedical Engineering*, 53(1):21–27, 2006.

- J. R. Pierce. *An Introduction to Information Theory: Symbols, Signals and Noise*. Dover Publications, Incorporated, 1980.
- A. Porta, S. Guzzetti, N. Montano, R. Furlan, M. Pagani, A. Malliani, and S. Cerutti. Entropy, entropy rate, and pattern classification as tools to typify complexity in short heart period variability series. *IEEE Transactions on Biomedical Engineering*, 48(11):1282–1291, 2001.
- K. Punithakumar, I. Ben Ayed, I. Ross, A. Islam, J. Chong, and S. Li. Detection of left ventricular motion abnormality via information measures and bayesian filtering. *IEEE Transactions on Information Technology in Biomedicine*, 14(4):1106–1113, 2010.
- B.-S. Yaakov, K. Thiagalingam, and L. X. Rong. *Estimation with Applications to Tracking and Navigation*. John Wiley & Sons Inc., 2002.

Chapter 5

Conclusion

5.1 General Discussion

Cardiovascular diseases With 40% fatality rate impose a huge burden on societies. Heart failure, which affects roughly 500,000 Canadians annually, is indicated by the failure of the heart to fill the ventricles and eject adequate volume of blood to the rest of the body [Ross et al. \[2006\]](#). Its progression is caused from a number of different pathologies such as myocardial infarction, hypertension or cardiomyopathy [Figuroa and Peters \[2006\]](#).

In order to reduce the rate of hospitalization and its associated cost, tools that allow radiologists to reach an early, efficient, simple and accurate quantification of clinical criteria are highly desired [Caiani et al. \[2004b\]](#).

A critical step in the diagnosis of cardiovascular diseases is the assessment of the LV function using global structural/anatomical indicators such as EF and indicators such as wall

motion. In clinical routines, these assessments rely on visual evaluation or manual segmentation and interpretation of the LV wall motion in image modalities such as MRI Afshin [2012], Ayed et al. [2012a]. However, visual assessments are subject to high inter-observer variability, inaccuracy, and have limited reproducibility Hoffmann et al. [2006], Redheuil et al. [2007]. In contrast, automated LV and RV segmentations in short-axis cardiac MRI is rapid, reproducible and subject independent.

Although algorithms for the LV segmentation do exist, they require either extensive training or intensive user inputs. The RV segmentation in MRI has yet to be solved and is still acknowledged as a completely unsolved problem.

In this thesis, I proposed fast detection of the LV endo- and epi-cardium surfaces (3D) and contours (2D) in short-axis cardiac MRI via convex relaxation and distribution matching, along with a rapid 3D segmentation of the RV in cardiac MRI via distribution matching constraints on segment shape and appearance. The segmentation results were also used for fast and accurate classification of the wall motion abnormalities. It is anticipated the proposed methods can be integrated into clinical practice as aid-diagnostic tools to assist radiologists in their assessments.

5.2 Cardiovascular Magnetic Resonance Imaging

Cardiac MRI is the modality of choice for cardiac disease diagnosis as well as monitoring the recovery and progression of the disease Karamitsos et al. [2007], Mahrholdt et al. [2002]. Its advantages are including being noninvasive imaging and a great contrast between chambers, cavities and soft tissue. It has an enhanced spatial resolution and excellent contrast be-

tween blood and myocardium as well as epicardium and surrounding fat Sarwar et al. [2008], Karamitsos et al. [2007], Mahrholdt et al. [2002]. Unlike some other imaging modalities, it does not expose the patient to ionizing radiation which makes it an attractive and powerful research tool for follow-up studies. Since these factors allow for precise and reproducible measurements of LV volumes, EF, and mass, the research studies require smaller numbers of patients to attain sufficient statistical power Sarwar et al. [2008]. In this thesis, 2D short-axis cine MR images were acquired using a 1.5T scanner in balanced steady-state free precession mode. The datasets contained apical, mid-cavity and basal slices from 30 normal and 18 abnormal subjects as well as a 48 subjects from a public database published by MICCAI for the RV challenge 2012.

5.3 Techniques to automate the quantification of cardiac MRI and wall motion abnormality detection

5.3.1 Segmentations

In chapters two and three, the LV and RV regions were quantified using automatically delineated segmentation surfaces. Volumes and EF are essential measures in the diagnosis of cardiovascular diseases. They are often estimated via manual segmentation of several images in a cardiac sequence, which is prohibitively time consuming. Chapter two proposed a fast delineation of the *LV* endo- and epicardial boundaries while chapter three investigated the delineation of *RV* endocardial surfaces in short-axis cardiac cine MRI. The solution was obtained with a convex-relaxation optimization of two original functionals, an intensity and shape prior

which is intrinsically invariant with respect to translation. As scale-invariance solution was achieved by introducing a scale variable to the formulations. The proposed algorithm avoids the need for large training sets, computationally expensive registration, and unlike atlas based priors, it can tolerate shape deformations. The parallelized implementation on a GPU demonstrated that the proposed algorithm requires about 3.78 seconds to segment the LV volumes for a typical cardiac *MRI* volume, 5 times faster than a typical standard implementation. A performance evaluation over the databases demonstrated that the automatically delineated 3D surfaces correlate with independent manual contours. The results were assessed using *DM*, *RMSE*, and *CC* metrics, with the proposed 3D algorithm resulting in the same *RMSE* (a measure of distance between surfaces) as other 2D algorithms, although these 2D approaches require more extensive user inputs. I demonstrated that the algorithm performance is robust to the initial conditions. The fully automated 3D method for LV segmentation yielded a decrease in accuracy when compared to the 2D approach. This effect can be explained by the fact that 3D formulation requires much less user input than the 2D method. For the 2D case, the user is required to manually segment the first frame of the time sequence of each slice in the testing subject data, whereas in the 3D case the algorithm only needs a single starting point (mouse click) per target region (cavity or myocardium), i.e., two clicks for the whole 3D+time subject data. The 3D algorithm can become more accurate at the expense of much more post-processing user interactions. Significantly reducing the user input compared to the 2D algorithm, the 3D formulation included new optimization steps/variables. In the 3D algorithm, the degrees of freedom for the problem and its difficulty are higher, and the prior knowledge is less informative (a training subject different from the testing subject was used). The 3D performance can likely be improved by further adding user inputs, for instance, by

using the same user delineations as in the 2D case.

In chapter three, I investigated a unique solution to rapid automated RV image segmentation using object-interaction priors. RV segmentation in short-axis MRI has not so far received much attention in the literature. The solution was obtained with a convex-relaxation optimization of two original functionals, each containing two distribution-matching priors, one encoding intensity information and the other shape information. The novel shape prior that was used in this chapter takes into account the RV position and interactions with the LV cavity and its centroid. The applied shape prior is intrinsically invariant with respect to translation and scale. In addition, a scale variable from which a FPE was derived, was introduced thereby achieving scale-invariance with only few fast computations. The employed bound on the Bhattacharya distance between distributions permitted the embedding of descriptors for intensity distributions along with scale- and translation-invariant distance and angle distributions. The proposed algorithm relaxes the need for costly pose estimation (or registration) procedures and large training sets, and can tolerate shape deformations, unlike template (or atlas) based priors.

Furthermore, the method's robustness was tested experimentally, demonstrating that the performance of the algorithm is not significantly affected by the choice of the training subject, and the shape description which was used does not change significantly from one subject to another. The algorithm was evaluated for the complex RV segmentation problem in cine short-axis MR images from two different datasets, and was compared with six other fully automated and semi-automated 3D RV segmentation algorithms which participated in a public challenge organized by MICCAI community. The proposed highly automated 3D algorithm achieved reasonable results among fully automated algorithms. The quantitative results for DM and

HD in ED and ES phases showed that the algorithm outperforms the majority of the automated approaches. This chapter also reports a performance evaluation for RV regions over 64 volumes acquired from 32-subjects provided by the RV Challenge at MICCAI'12 and 400 volumes from the in-house dataset of 20 subjects. The results show that the obtained 3D surfaces correlate with independent manual delineations.

Finally, experiments performed on the LV and RV regions demonstrated that (1) the performance of the algorithm is not significantly affected by the choice of the training subject; and (2) the shape description was proposed does not significantly change from one subject to another. The promising results demonstrate that with further developments the approach will be feasible to be used in current clinical routines.

5.3.2 Wall motion

The myocardium wall motion that is assessed visually in short-axis CMRI by a majority of radiologists relies extensively on the radiologist's ability to perceive temporal and spatial information about the wall thickening and the motion of the myocardial segments [Caiani et al. \[2004b\]](#). Several clinical studies have demonstrated that visual assessments are not very accurate and suffer from inter-observer variability [Lu et al. \[2009\]](#), [Caiani et al. \[2004a,b\]](#). As a result, novel methods for automated evaluation of these regions have become a major area of research in the past few years [Petitjean and Dacher \[2011\]](#). The study in [Caiani et al. \[2004b\]](#) demonstrates the feasibility of quantitatively analyzing endocardial motion from CMR images. The experiment shows that automated methods can be used to accurately detect wall motion abnormalities, whereas the detection of wall motion abnormalities by radiologists could be less

accurate and suffer from high inter-observer variability.

In chapter four, I derived an ANN to classify the LV motion based on information-theoretic measures. The ANN was trained by global measures from the distributions of wall motion statistics such as radial distance and velocity. The automatically delineated segmentation contours were sampled into discrete points in each 2D frame, and the points were then passed through recursive Bayesian and Kalman filtering to track the trajectory of each point over the cardiac temporal phases. Using this approach, statistics such as radial distance and velocity were computed for each sampled point. Then, using a kernel density estimate, the information-theoretic measures such as SDE, Renyi entropy and Fisher information were computed. The applied multi-layer ANN was examined by different combinations of the information theoretics and distribution measures to determine the best combination. The ANN structure was subject to modifications in a number of layers, nodes and activation functions to obtain the best structure. The proposed method was devised based on quantitative wall motion analysis. The radial distance and velocity features used in this chapter were chosen to closely mimic radiologists visual tracking of abnormal and normal motions. The results according to ROC, AUCs, and Bhattacharyya distance metrics, and *leave-one-out* cross validation, demonstrate that the proposed ANN leads to a significant improvement over other classifiers.

5.4 Future Directions

The algorithms in chapters two and three use a special bound of the similarity measure currently. One may improve the algorithm using a general upper bound instead of Bhattacharyya. Improving the accuracy of the proposed segmentation methods, which are highly automated,

can bring together an excellent diagnostic package with a high degree of reliability. The experiments also could be performed using 3T cardiac MR images to observe whether having a better contrast between soft tissue and blood can improve the segmentation results.

The algorithm in chapter three currently segments only the RV endocardium. It would be of interest if different shape and intensity priors can be tried to segment myocardium regions as well. Having the segmented RV myocardium, tracking and analysis of the RV wall motion and thickening can also be used in diagnosis of RV related diseases such as ARVC and Hypertrophic cardiomyopathy (HCM).

I observed a tremendous potential in the segmentation algorithm to be utilized for segmentation of other anatomical organs such as lumbar spine and vertebrae. The segmentation of vertebrae with the requirement of only one click from a user is highly desired in clinical practice [Ayed et al. \[2012b, 2011\]](#).

The applied abnormality classification method in chapter 4 is a global classification approach and does not interpret myocardium with specific abnormalities in local segments currently. One of the main foci of future research could be segmental tracking of the myocardium and using ANN to classify each segment independently, clustering them into specific known abnormality groups, and eventually mapping the results into a 17-segment bull's eye plot. One can improve the speed and accuracy of the classifier by tracking the points on 3D surfaces of the LV and RV volumes. Also, the accuracy of the algorithm could be improved by training the ANN with a large number of abnormal cases belonging to other heart conditions. Thus, the proposed framework can be used as an adaptive stand-alone application which can be trained towards particular diseases.

As described in the introduction chapter, in clinical practice, DE-MRI is used to detect scars that have been formed on myocardium region. Combining the segmentation results from cine MRI with volumetric DE-MRI would be of interest for radiologists. Using the convex relaxation algorithm introduced in this thesis, one could propose an approach to register the segmented myocardial region in short-axis cine MRI to volumetric DE-MRI. Also, examining the proposed convex relaxation algorithm directly on DE-MRI for segmentation of the myocardium would be of interest.

I believe that with further developments, these algorithms can be integrated into either existing diagnostic packages or as stand-alone applications into portable machines for an efficient and repeatable diagnosis of ventricular or bi-ventricular diseases. As portable machines gain acceptance amongst radiologists, one commercial direction to pursue is to implement the proposed highly automated segmentation algorithms on a touch device so that the 3D RV and LV volume rendering is controlled with fingertip movements around the centroid of the LV cavity.

Bibliography

- M. Afshin. *Automatic Assessment of Cardiac Left Ventricle Function Via Magnetic Resonance Images*,. PhD thesis, The School of Graduate and Postdoctoral Studies, Western University, London, Ontario, Canada, 2012.
- I. Ben Ayed, K. Punithakumar, G.J. Garvin, W. Romano, and S. Li. Graph cuts with invariant object-interaction priors: Application to intervertebral disc segmentation. *IPMI*, pages 221–232, 2011.
- I. Ben Ayed, H.-M. Chen, K. Punithakumar, I. Ross, and S. Li. Max-flow segmentation of the left ventricle by recovering subject-specific distributions via a bound of the bhattacharyya measure. *Medical Image Analysis*, 16:87–100, 2012a.
- I. Ben Ayed, K. Punithakumar, R. Minhas, R. Joshi, and G.J. Garvin. Vertebral body segmentation in mri via convex relaxation and distribution matching. *Medical Image Computing and Computer-Assisted Intervention (MICCAI)*, pages 520–527, 2012b.
- EG Caiani, E Toledo, P. MacEneaney, KA Collins, RM Lang, and V Mor-Avi. The role of still-frame parametric imaging in magnetic resonance assessment of left ventricular wall motion by non-cardiologists. *Journal of Cardiovasc Magnetic Resonance*, 6:619–25, 2004a.

- E.G. Caiani, E. Toledo, P. MacEneaney, K.A Collins, R.M. Lang, and V. Mor-Avi. Objective assessment of left ventricular wall motion from cardiac magnetic resonance images. *Computers in Cardiology*, pages 153 –156, 2004b.
- M. S. Figueroa and J. I. Peters. Congestive heart failure: Diagnosis, pathophysiology, therapy, and implications for respiratory care. *Respiratory Care*, 51:403–413, 2006.
- R. Hoffmann, S. von Bardeleben, J. D. Kasprzak, A. C. Borges, F. ten Cate, C. Firschke, S. Lafitte, N. Al-Saadi, S. Kuntz-Hehner, G. Horstick, C. Greis, M. Engelhardt, J. L. Vanoverschelde, and H. Becher. Analysis of regional left ventricular function by cineventriculography, cardiac magnetic resonance imaging, and unenhanced and contrast-enhanced echocardiography: A multicenter comparison of methods. *Journal of the American College of Cardiology*, 47(1):121128, 2006.
- T. D. Karamitsos, L. E. Hudsmith, J. B. Selvanayagam, S. Neubauer, and J. M. Francis. Operator induced variability in left ventricular measurements with cardiovascular magnetic resonance is improved after training . *Journal of Cardiovascular Magnetic Resonance*, 9:777783, 2007.
- Y. Lu, P. Radau, K. Connelly, A. Dick, and G. Wright. Pattern recognition of abnormal left ventricle wall motion in cardiac MR. in *Medical Image Computing and Computer-Assisted Intervention; MICCAI*, 5762:750–758, 2009.
- H. Mahrholdt, A. Wagner, T. A. Holly, M. D. Elliott, R. O. Bonow, R. J. Kim, and R. M. Judd. Reproducibility of chronic infarct size measurement by contrast-enhanced magnetic resonance imaging. *Circulation*, 106:23222327, 2002.

- C. Petitjean and J.-N. Dacher. A review of segmentation methods in short axis cardiac MR images. *Medical Image Analysis*, 15:169–184, 2011.
- A. B. Redheuil, N. Kachenoura, R. Laporte, A. Azarine, X. Lyon, O. Jolivet, F. Frouin, and E. Mousseaux. Interobserver variability in assessing segmental function can be reduced by combining visual analysis of CMR cine sequences with corresponding parametric images of myocardial contraction. *Journal of Cardiovascular Magnetic Resonance*, 9(6):863872, 2007.
- H. Ross, J. Howlett, J. M. Arnold, P. Liu, B. J. O’Neill, J. M. Brophy, C. S. Simpson, M. M. Sholdice, M. Knudtson, D. B. Ross, J. Rottger, K. Glasgow, and Canadian Cardiovascular Society Access to Care Working Group. Treating the right patient at the right time: Access to heart failure care. *Canadian Journal of Cardiology*, 22:749–745, 2006.
- A. Sarwar, M. D. Shapiro, S. Abbara, and R. C. Cury. Cardiac magnetic resonance imaging for the evaluation of ventricular function. *Seminars in Roentgenology*, 43:183–192, 2008.

Copyright Reprint Permissions



RightsLink®

Home

Create Account

Help



Title: Detection of Left Ventricular Motion Abnormality Via Information Measures and Bayesian Filtering
Author: Punithakumar, K.; Ben Ayed, I.; Ross, I.G.; Islam, A.; Chong, J.; Shuo Li
Publication: Information Technology in Biomedicine, IEEE Transactions on
Publisher: IEEE
Date: July 2010
Copyright © 2010, IEEE

User ID
<input type="text"/>
Password
<input type="text"/>
<input type="checkbox"/> Enable Auto Login
<input type="button" value="LOGIN"/>
Forgot Password/User ID?
If you're a copyright.com user, you can login to RightsLink using your copyright.com credentials. Already a RightsLink user or want to learn more?

Thesis / Dissertation Reuse

The IEEE does not require individuals working on a thesis to obtain a formal reuse license, however, you may print out this statement to be used as a permission grant:

Requirements to be followed when using any portion (e.g., figure, graph, table, or textual material) of an IEEE copyrighted paper in a thesis:

- 1) In the case of textual material (e.g., using short quotes or referring to the work within these papers) users must give full credit to the original source (author, paper, publication) followed by the IEEE copyright line © 2011 IEEE.
- 2) In the case of illustrations or tabular material, we require that the copyright line © [Year of original publication] IEEE appear prominently with each reprinted figure and/or table.
- 3) If a substantial portion of the original paper is to be used, and if you are not the senior author, also obtain the senior author's approval.

Requirements to be followed when using an entire IEEE copyrighted paper in a thesis:

- 1) The following IEEE copyright/ credit notice should be placed prominently in the references: © [year of original publication] IEEE. Reprinted, with permission, from [author names, paper title, IEEE publication title, and month/year of publication]
- 2) Only the accepted version of an IEEE copyrighted paper can be used when posting the paper or your thesis on-line.
- 3) In placing the thesis on the author's university website, please display the following message in a prominent place on the website: In reference to IEEE copyrighted material which is used with permission in this thesis, the IEEE does not endorse any of [university/educational entity's name goes here]'s products or services. Internal or personal use of this material is permitted. If interested in reprinting/republishing IEEE copyrighted material for advertising or promotional purposes or for creating new collective works for resale or redistribution, please go to http://www.ieee.org/publications_standards/publications/rights/rights_link.html to learn how to obtain a License from RightsLink.

If applicable, University Microfilms and/or ProQuest Library, or the Archives of Canada may supply single copies of the dissertation.

BACK

CLOSE WINDOW



RightsLink®

Account
Info

Help



Title: Max-flow segmentation of the left ventricle by recovering subject-specific distributions via a bound of the Bhattacharyya measure

Author: Ismail Ben Ayed, Hua-mei Chen, Kumaradevan Punithakumar, Ian Ross, Shuo Li

Publication: Medical Image Analysis

Publisher: Elsevier

Date: Jan 1, 2012
Copyright © 2012, Elsevier

Logged in as:
mohammad nambakhsh
Account #:
3000675159

LOGOUT

Order Completed

Thank you very much for your order.

This is a License Agreement between mohammad nambakhsh ("You") and Elsevier ("Elsevier")
The license consists of your order details, the terms and conditions provided by Elsevier, and the [payment terms and conditions](#).

License number	Reference confirmation email for license number
License date	Jul 11, 2013
Licensed content publisher	Elsevier
Licensed content publication	Medical Image Analysis
Licensed content title	Max-flow segmentation of the left ventricle by recovering subject-specific distributions via a bound of the Bhattacharyya measure
Licensed content author	Ismail Ben Ayed, Hua-mei Chen, Kumaradevan Punithakumar, Ian Ross, Shuo Li
Licensed content date	January 2012
Licensed content volume number	16
Licensed content issue number	1
Number of pages	14
Type of Use	reuse in a thesis/dissertation
Portion	figures/tables/illustrations
Number of figures/tables/illustrations	All
Actual number of figures/tables/illustrations	36
Format	both print and electronic
Are you the author of this Elsevier article?	Yes
Will you be translating?	No
Order reference number	
Title of your thesis/dissertation	AUTOMATED SEGMENTATION OF LEFT AND RIGHT VENTRICLES IN MRI AND CLASSIFICATION OF THE MYOCARDIUM ABNORMALITIES
Expected completion date	Sep 2013
Elsevier VAT number	GB 494 6272 12
Billing Type	Invoice
Billing address	75 ann street london, ON n6a 1r1 Canada
Permissions price	0.00 USD
VAT/Local Sales Tax	0.00 USD
Total	0.00 USD



Title: Automated regional wall motion abnormality detection by combining rest and stress cardiac MRI: Correlation with contrast-enhanced MRI

Author: Avan Suinesiaputra, Alejandro F. Frangi, Theodorus A.M. Kaandorp, Hildo J. Lamb, Jeroen J. Bax, Johan H.C. Reiber, Boudewijn P.F. Lelieveldt

Publication: Journal of Magnetic Resonance Imaging

Publisher: John Wiley and Sons

Date: Jul 20, 2011

Copyright © 2011 Wiley-Liss, Inc.

Logged in as:
mohammad nambakhsh

LOGOUT


Order Completed

Thank you very much for your order.

This is a License Agreement between mohammad nambakhsh ("You") and John Wiley and Sons ("John Wiley and Sons"). The license consists of your order details, the terms and conditions provided by John Wiley and Sons, and the [payment terms and conditions](#).

[Get the printable license.](#)

License Number	3185830993794
License date	Jul 11, 2013
Licensed content publisher	John Wiley and Sons
Licensed content publication	Journal of Magnetic Resonance Imaging
Licensed content title	Automated regional wall motion abnormality detection by combining rest and stress cardiac MRI: Correlation with contrast-enhanced MRI
Licensed copyright line	Copyright © 2011 Wiley-Liss, Inc.
Licensed content author	Avan Suinesiaputra, Alejandro F. Frangi, Theodorus A.M. Kaandorp, Hildo J. Lamb, Jeroen J. Bax, Johan H.C. Reiber, Boudewijn P.F. Lelieveldt
Licensed content date	Jul 20, 2011
Start page	270
End page	278
Type of use	Dissertation/Thesis
Requestor type	University/Academic
Format	Print and electronic
Portion	Figure/table
Number of figures/tables	1
Original Wiley figure/table number(s)	1
Will you be translating?	No
Total	0.00 USD



Office of Research Ethics
The University of Western Ontario

Use of Human Subjects - Ethics Approval Notice

Principal Investigator: Dr. I. Ross
Review Number: 16634E
Review Date: December 04, 2009
Protocol Title: Computer assisted image based cardiac disease diagnosis and monitoring
Department and Institution: Imaging, London Health Sciences Centre
Sponsor: NSERC-NATURAL SCIENCES ENGINEERING RSRCH COU
Ethics Approval Date: July 20, 2010
Documents Reviewed and Approved: UWO Protocol

Review Level: Expedited
Approved Local # of Participants: 100
Expiry Date: December 31, 2014

Documents Received for Information:

This is to notify you that The University of Western Ontario Research Ethics Board for Health Sciences Research Involving Human Subjects (HSREB) which is organized and operates according to the Tri-Council Policy Statement: Ethical Conduct of Research Involving Humans and the Health Canada/ICH Good Clinical Practice Practices: Consolidated Guidelines; and the applicable laws and regulations of Ontario has reviewed and granted approval to the above referenced study on the approval date noted above. The membership of this REB also complies with the membership requirements for REB's as defined in Division 5 of the Food and Drug Regulations.

The ethics approval for this study shall remain valid until the expiry date noted above assuming timely and acceptable responses to the HSREB's periodic requests for surveillance and monitoring information. If you require an updated approval notice prior to that time you must request it using the UWO Updated Approval Request Form.

During the course of the research, no deviations from, or changes to, the protocol or consent form may be initiated without prior written approval from the HSREB except when necessary to eliminate immediate hazards to the subject or when the change(s) involve only logistical or administrative aspects of the study (e.g. change of monitor, telephone number). Expedited review of minor change(s) in ongoing studies will be considered. Subjects must receive a copy of the signed information/consent documentation.

Investigators must promptly also report to the HSREB:

- changes increasing the risk to the participant(s) and/or affecting significantly the conduct of the study;
- all adverse and unexpected experiences or events that are both serious and unexpected;
- new information that may adversely affect the safety of the subjects or the conduct of the study.

If these changes/adverse events require a change to the information/consent documentation, and/or recruitment advertisement, the newly revised information/consent documentation, and/or advertisement, must be submitted to this office for approval.

Members of the HSREB who are named as investigators in research studies, or declare a conflict of interest, do not participate in discussion related to, nor vote on, such studies when they are presented to the HSREB.

Chair of HSREB: Dr. Joseph Gilbert
FDA Ref. #: IRB 00000940

Curriculum Vitae

Education

PhD candidate, Biomedical Engineering. **2009-2013**

Biomedical Engineering Graduate Program, Western University.

Thesis: *Automated segmentation and quantification of LV and RV and wall motion abnormality detection in CMRI.*

Supervisors: Dr. Terry Peters, Dr. Ismail Ben Ayed.

MSc, Biomedical Engineering. **2003-2006**

Dept. of Biomedical Systems & Medical Physics, Biomedical Division, Tehran University of Medical Sciences (TUMS), Iran.

Thesis: *Watermarking of ECG signals on medical images using EZW algorithm.*

Supervisors: Dr. Alireza. Ahmadian, Tehran University of Medical Sciences, Dr. Mohammad. Ghavami, Kings College London. Dr. Reza.S Dilmaghani, Kings College London.

BSc, Biomedical Engineering. **1999-2003**

Dept. of Biomedical Engineering, Amirkabir University of Technology (Polytechnic), Tehran, Iran.

Project: *Design of Digital Nurse Caller.*

Honours and Achievements

- Western Graduate Research Scholarship
- NSERC Collaborative Research and Training Experience (CREATE) Program in Computer-Assisted Medical Interventions
- Canadian Institute of Health Research (CIHR), Vascular Training Program
- Travel Bursary Award
- 3rd amongst participants of national-wide entry level exam, BME, MSc level.
- Qualified as distinguished student and rewarded exemption of compulsory military service, Iran
- Top ranked student, MSc program at Tehran University of Medical Sciences

Related Work and Teaching Assistant

- C++, C sharp, Image Processing. 2009-2013
- FPGA & VHDL Programming, Tehran University. 2005-2007

Computer and Programming Skills

- *Proficient in:* ASP.NET, C sharp, C++, Microsoft SQL Server 2012, WCF, Html5, CSS, JQuery, JQuery Mobile, VHDL, AHDL, C for Micro-controllers.
- *Software:* Solidworks, Visual Studio 2012, TFS, SQL management, Matlab, Simulink, Quartus II, DSP builder, ISE, Modelsim, Code Vision, Orcad, Protel, Multisim (national instrument).
- *Project Management:* Asana, Base-camp

Publications

Journal and Conference Papers

Journal Papers

1. Cyrus M.S. Nambakhsh, Jing Yuan, Kumaradevan Punithakumar, Aashish Goela, Martin Rajchl, Terry M. Peters, Ismail Ben Ayed, *Left Ventricle Segmentation in MRI via Convex Relaxed Distribution Matching*, Medical Image Analysis (MEDIA), 2013.
2. Cyrus M.S. Nambakhsh, Greg Garvin, Terry M. Peters, Ismail Ben Ayed, Shuo Li, *Graph Cuts Optimization of Invariant Object-Interaction Priors: Application to Cardiac and Lumbar Spine MR Images*, to be Submitted to IEEE TMI, 2013.
3. Martin Rajchl, Jing Yuan, James A. White, Eranga Ukwatta, John Stirrat, Cyrus M.S. Nambakhsh, Feng P.Li, and Terry M. Peters, *Fast Hierarchical Max-Flow Segmentation of Scar Tissue from Late-Enhancement Cardiac MR Images*, submitted to IEEE Transaction of Medical Imaging, April, 2013.
4. Caroline Petitjean, Cyrus M.S. Nambakhsh, et., al, *Right Ventricle Segmentation From Cardiac MRI: A Collation Study*, Submitted to IEEE TMI, 2013.
5. Cyrus M.S. Nambakhsh, Terry M. Peters, Ismail Ben Ayed, *Analysis of a General Upper Bound for RV Segmentation with Probability Product Kernel Constraints*, To be submitted to IEEE TMI, 2013.
6. M. S. Nambakhsh, A. Ahmadian and Habib Zaidi, *A Novel Contextual Based Multiple Watermarking of PET Images by Patient ID and ECG Signal*, Elsevier, Journal of Computerized Medical Imaging and Graphics, 2010, in press.
7. M. S. Nambakhsh and M. Shiva, *A Novel Blind Wavelet Base Watermarking of ECG Signals on Medical Images Using EZW Algorithm*, Encyclopedia of Healthcare Information Systems, Idea Group, Illinois University, USA, 2007.
8. M. S. Nambakhsh, A. Ahmadian, M. Ghavami and R. S. Dilmaghani, *Watermarking of ECG signals on medical images using EZW algorithm*, Iranian Journal of Medical Physics, August 26, 2006.

Conference papers

1. Cyrus M.S. Nambakhsh, Terry M. Peters, Ismail Ben Ayed, ***Right Ventricle Segmentation with Probability Product Kernel Constraints***, MICCAI, 2013.
2. Cyrus M.S. Nambakhsh, M. Rajchl, Terry M. Peters, Ismail Ben Ayed, ***Rapid Automated 3D RV Endocardium Segmentation in MRI via Convex Relaxation and Distribution Matching***, RV Segmentation Challenge in Cardiac MRI, MICCAI, 2012.
3. M. Rajchl, J. Yuan, E. Ukwatta, C. Nambakhsh, J. Stirrat, J. White, and T.M. Peters, ***A Fast Convex Optimization Approach to Segmenting 3D Scar Tissue from Delayed-Enhancement Cardiac MR Images***. Medical Image Computing and Computer-Assisted Intervention, 2012.
4. M.S. Nambakhsh, jing Yuan, Ismail Ben Ayed, Kumaradevan Punithakumar, Aashish Goela, Ali Islam Terry M. Peters and Shuo Li, ***A Convex Max-Flow segmentation of LV using Subject-Specific Distributions on Cardiac MRI***, International Conference on Information Processing in Medical Imaging, Germany, 2011.
5. M.S. Nambakhsh, Kumaradevan Punithakumar, Ismail Ben Ayed, Terry M. Peters and Shuo Li, ***A Neural Network Learned Information Theoretic Measure for Heart Motion Abnormality Detection***, SPIE, Medical Imaging, USA, 2011.
6. M. Baboli, A. Sharafi, A. Ahmadian, M.S. Nambakhsh, ***An accurate and robust algorithm for detection of heart and respiration rates using an impulse based UWB signal***, IEEE International Conference on Biomedical and Pharmaceutical Engineering, 2009.
7. Vahid Tavakoli and M. S. Nambakhsh, ***A Fast and Accurate Method for Echocardiography Strain Rate Imaging***, SPIE, Annual Meeting Medical Imaging USA, 2009.
8. M. S. Nambakhsh, V. Tavakoli and N. Sahba, ***FPGA-Core Defibrillator using Wavelet-Fuzzy ECG Arrhythmia Classification***, Proceedings of IEEE EMBS, Conference, 2008, Canada.
9. V. Tavakoli, M. S. Nambakhsh and N. Sahba, ***A New Variational Technique for Combining Affine Registration and Optical Flow in Echocardiography Images***, Proceedings of IEEE EMBS Conference, 2008, Canada.
10. N. Sahba, V. Tavakoli and M. S. Nambakhsh, ***Ultrasound Thermal Change Detection based on Steerable Filters***, Proceedings of IEEE EMBS, Canada, 2008.
11. M. S. Nambakhsh, A. Ahmadian, M. Ghavami, R. S. Dilmaghani and S. Karimifard, ***A novel blind Watermarking of ECG signals on medical images using EZW algorithm***, Proceedings of IEEE EMBS, USA, 2006.
12. S. Karimifard, A. Ahmadian, M. Khoshnevisan and M. S. Nambakhsh, ***Morphological Heart Arrhythmia Detection Using Hermitian Basis Functions and kNN Classifier***, Proceedings of IEEE EMBS, USA , 2006.

Books

1. M.S. Nambakhsh, *Digital Circuits Design by FPGA & FIPSOC*, in Electrical Engineering and Hardware Design Series (in Farsi), 2002, 448 pages, ISBN: 964-377-031-1, Naghoos Press.
2. M.S. Nambakhsh, *Wavelet Neural Networks and Applications*, in Engineering Series (in Farsi), 2005, 100 pages, ISBN: 964-377-187-3, Naghoos Press.
3. *AVR Assembly language*, in Electrical Engineering Series (in Farsi), 2006, 96 pages, ISBN: 964-377-242-x, Naghoos Press.